https://doi.org/10.5194/egusphere-2026-6615
Preprint. Discussion started: 10 November 2026
© Author(s) 2026. CC BY 4.0 License.

The integrated aerosol–climate model CIESM-PAMT: Part 1. Model description and aerosol evaluation

Hengqi Wang[1,a,#], Minqi Wang[1,2,#], Yiran Peng[1*], Knut von Salzen[3,4], Jiangnan Li[4], Husi Letu[5], Luke Fraser-Leach[6], Jinyuan Xin[7], Xiaoye Zhang[8], and Johannes Quaas[9]

[1]Department of Earth System Science, Ministry of Education Key Laboratory for Earth System Modeling, Institute for Global Change Studies, Tsinghua University, Beijing, 100084, China
[2]COMNOVA, Shanghai, 201203, China
[3]Department of Atmospheric and Climate Science, University of Washington, Washington, Seattle, USA
[4]Canadian Centre for Climate Modelling and Analysis, Environment and Climate Change Canada, Victoria, British Columbia, Canada
[5]State Key Laboratory of Remote Sensing and Digital Earth, Aerospace Information Research Institute, Chinese Academy of Sciences, Beijing, 100094, China
[6]Department of Physics, University of Toronto, Toronto, M5S1A7, Canada
[7]State Key Laboratory of Atmospheric Environment and Extreme Meteorology, Institute of Atmospheric Physics, Chinese Academy of Sciences, Beijing 100029, China
[8]State Key Laboratory of Severe Weather Meteorological Science and Technology (LaSW) and Key Laboratory of Atmospheric Chemistry of CMA, Chinese Academy of Meteorological Sciences, Beijing 100081, China
[9]Leipzig Institute of Meteorology, Leipzig University, Leipzig, 04109, Germany
[a]now at: State Key Laboratory of Remote Sensing and Digital Earth, Aerospace Information Research Institute, Chinese Academy of Sciences, Beijing, 100094, China
[#]Contributed equally to this work.

Correspondence to: Yiran Peng (pyiran@mail.tsinghua.edu.cn)

Abstract. Aerosols play a critical role in regulating the Earth's climate system by influencing the radiative balance and cloud processes. Climate models with online-coupled aerosol modules are essential tools for studying such effects. To enhance the representation of aerosol processes in the Community Integrated Earth System Model (CIESM), this study couples a new aerosol module, the Piecewise lognormal approximation Aerosol Model for Tsinghua University (PAMT), creating the integrated aerosol–climate model CIESM-PAMT. This work is presented in two parts. The current paper (Part 1) focuses on the model description and the evaluation of aerosol simulations, whereas Part 2 focuses on clouds, precipitation, and aerosol radiative forcing (paper in preparation). Compared with the original seven-mode aerosol module (MAM7) in CIESM (CIESM-MAM7), CIESM-PAMT updates nearly all aerosol processes, reduces the number of tracers from 31 to 24, and allows for more flexible adjustments of aerosol size-distribution resolution before compilation, thereby improving computational efficiency while maintaining simulation accuracy, albeit at the expense of representing some aerosol processes.

Evaluation results show that CIESM-PAMT reproduces global aerosol spatial distributions, optical properties, and number and mass concentrations with varying degrees of agreement with observations. Compared with AERONET measurements, the relative biases in aerosol optical depth (AOD), fine-mode AOD, coarse-mode AOD, and Ångström exponent are 11%,

https://doi.org/10.5194/egusphere-2026-6615
Preprint. Discussion started: 10 November 2026
© Author(s) 2026. CC BY 4.0 License.

30%, −25%, and −8.6%, respectively. Comparisons with ground-based and shipborne observations yield relative biases of −6.7% for black carbon (BC), −21% for organic carbon (OC), 2.2% for land sulfate (SO4), and 65% for marine SO4 mass concentrations. The relative biases in PM2.5 and PM10 are −31% and −58%, respectively, while the bias in aerosol number concentration is −48%. In the Arctic region (>60°N), CIESM-PAMT can also capture the observed aerosol optical properties and concentration variations, although discrepancies remain for some aerosol components and sites.

Overall, the comparison indicates that CIESM-PAMT generally achieves better agreement with observations than CIESM-MAM7 for aerosol optical properties, BC and OC mass concentrations, and aerosol number concentrations. The two configurations show comparable results for land SO4 and PM2.5, whereas CIESM-PAMT exhibits larger biases in PM10 and marine SO4. In the Arctic, CIESM-PAMT reduces the systematic biases in most evaluated aerosol properties. Overall, CIESM-PAMT provides a more realistic representation of global aerosol distributions, optical properties, and concentrations by adopting a flexible piecewise lognormal aerosol representation, thereby improving the capability of CIESM for aerosol–climate simulations. These improvements establish a robust basis for future investigations of aerosol–climate interactions and their climate impacts.

1 Introduction

Aerosols are key drivers of the Earth's climate, exerting both direct effects through the scattering and absorption of solar radiation and indirect effects by modifying cloud microphysics and precipitation (Albrecht, 1989; Bellouin et al., 2020; Twomey, 1977; Wang et al., 2025; Yu et al., 2006). Despite this well-established role, aerosol–cloud interactions and their associated climate feedbacks remain highly complex and exhibit pronounced variability across regions and timescales (Bellouin et al., 2020; Quaas et al., 2024; Rosenfeld et al., 2023). In this context, integrated aerosol–climate models constitute a fundamental tool for quantifying the global impacts of aerosols and for interpreting their contributions to observed climate variability and long-term trends (Bogenschutz et al., 2018; Cole et al., 2023; Salzmann et al., 2022; Tegen et al., 2019). Nevertheless, considerable uncertainties persist in current models, particularly in representing the spatial and temporal distribution of anthropogenic emissions, aerosol optical properties, and aerosol–cloud interactions, as highlighted by the Aerosol Comparisons between Observations and Models (AeroCom) initiative (Gliß et al., 2021). These deficiencies can translate into large discrepancies in simulated radiative forcing and cloud responses, thereby undermining confidence in climate projections (Gliß et al., 2021; IPCC, 2023). Therefore, continued development, rigorous evaluation, and systematic refinement of integrated aerosol–climate models are essential for improving the quantification of anthropogenic aerosol effects and for reducing persistent uncertainties in climate simulations.

Given the critical role of climate models in scientific research and policy decision-making, Tsinghua University initiated the development of an independent climate modelling system in 2009 and successfully released version 1.1 of the Community Integrated Earth System Model (CIESM) in 2019 (Lin et al., 2020). CIESM is built upon version 1.2.1 of the Community Earth System Model, developed by the National Center for Atmospheric Research (i.e., NCAR CESM1.2.1) (Hurrell et al.,

https://doi.org/10.5194/egusphere-2026-6615
Preprint. Discussion started: 10 November 2026
© Author(s) 2026. CC BY 4.0 License.

2013), and incorporates 13 independently developed or enhanced physical parameterizations and modules (Lin et al., 2020). CIESM has participated in multiple model intercomparison and evaluation activities, including the Coupled Model Intercomparison Project Phase 6 (CMIP6) (Chin et al., 2026; Lin et al., 2020; Mahmood et al., 2016; von Salzen et al., 2022; Whaley et al., 2022). CMIP6 simulations demonstrate that CIESM shows substantial improvements compared with the NCAR CESM1.2.1 in several long-standing challenges in the climate modelling community, including the distribution of tropical precipitation, the representation of marine boundary layer clouds, and the intensity and periodicity of the El Niño–Southern Oscillation (Lin et al., 2020). However, it is important to note that CIESM employed the observation-constrained aerosol forcing dataset MACv2-SP (Stevens et al., 2017) for its CMIP6 simulations, rather than its fully coupled aerosol module. This reliance on prescribed aerosol forcing limited the model's ability to physically represent aerosol–cloud interactions (ACI) and constrained its capacity to simulate the full complexity of aerosol–climate feedbacks (von Salzen et al., 2025).

In fact, CIESM is equipped with optional two-way coupled online aerosol modules. Its atmospheric component is developed based on version 5.3 of the Community Atmosphere Model (CAM5.3) in NCAR CESM1.2.1, and the aerosol component primarily includes the Aerosol Modules with three and seven lognormal modes (i.e., MAM3 and MAM7) (Liu et al., 2012). Previous studies have identified several known simplifications and systematic biases in MAM3, such as the rapid internal mixing of primary carbon aerosols into the accumulation mode and the coarse representation of aerosol size distributions (Ghan et al., 2012; Liu et al., 2016). Consequently, MAM7 is now much more commonly used than MAM3. In MAM7, several aerosol process parameterizations continue to follow established formulations, leaving room for further refinement (Ghan et al., 2012; Liu et al., 2016). Moreover, MAM7 tracks a number of tracers (31 in total), resulting in substantial computational costs. The number of overlapping lognormal modes and their geometric standard deviations in MAM7 are fixed, limiting flexibility for simplification or refinement based on computational needs. For example, achieving higher computational efficiency often requires replacing MAM7 with MAM3.

With the continuous improvement of computing resources, climate models require a more flexible scheme capable of dynamically adjusting the representation of the aerosol size distribution during runtime, thereby balancing computational efficiency with simulation accuracy. For this reason, when developing the new-generation NCAR CESM2 (Danabasoglu et al., 2020), the NCAR replaced MAM7 with the more computationally efficient and structurally simplified four-mode aerosol scheme, MAM4 (Liu et al., 2016). Accordingly, to achieve a more realistic representation of aerosol–cloud interactions while maintaining computational efficiency, CIESM also needs to improve and optimize its aerosol module.

To fill this gap, we adapted the Piecewise lognormal approximation Aerosol Model (PAM) used in AMAP (2021) for implementation in CIESM. We call this adapted version as the PAM for Tsinghua University (PAMT), forming the integrated aerosol–climate model CIESM-PAMT. Compared with MAM7, PAMT employs fewer tracers (24 in total), provides greater flexibility in representing aerosol size distributions, and substantially updates nearly all aerosol processes.

In the following, we present the model coupling and evaluation work in two parts. This paper constitutes Part 1, focusing on the key parameterizations implemented in PAMT, the coupling framework with CIESM, and the evaluation of the coupled

https://doi.org/10.5194/egusphere-2026-6615
Preprint. Discussion started: 10 November 2026
© Author(s) 2026. CC BY 4.0 License.

model's performance in aerosol simulations. Part 2 will further examine the simulations of clouds, precipitation, radiation, and aerosol–cloud interactions by CIESM-PAMT (paper in preparation). The evaluation draws upon a comprehensive set of observational and modelling datasets, including ground-based, shipborne, and satellite observations, reanalysis data, and multi-model results. The assessment provides quantitative benchmarks and guidance for the further development of CIESM. The remainder of this paper is organized as follows. Sections 2 and 3 describe the aerosol process parameterizations, coupling methodology, and model configuration of PAMT. Section 4 presents the multi-source observational datasets used for evaluation. Section 5 compares model simulations with observations and discusses the associated biases and uncertainties. Section 6 summarizes the main findings and future directions.

2 Coupling of CIESM and PAMT

2.1 Overview of CIESM

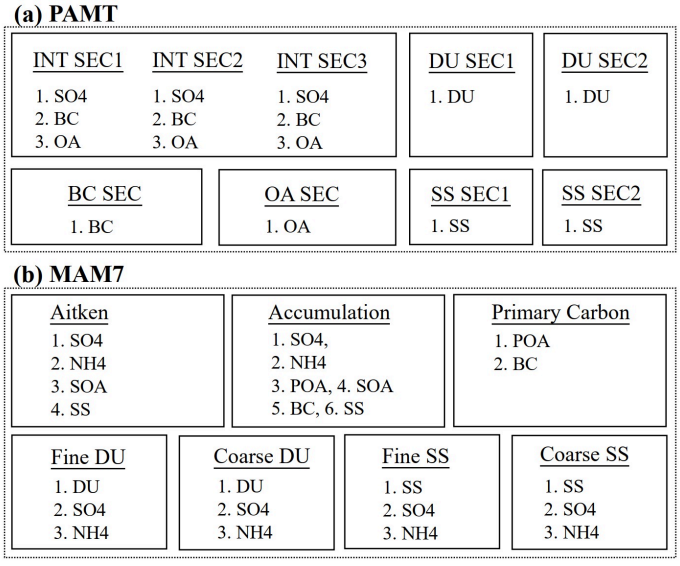


Figure 1. Aerosol composition of each mode in PAMT and MAM7. Aerosols within the same box are internally mixed, while aerosols in different black boxes are externally mixed.

CIESM was developed with a focus on correcting systematic biases in existing climate models by implementing new physical parameterizations across its component modules (Lin et al., 2020). Specifically, CIESM is built upon NCAR CESM1.2.1 (Hurrell et al., 2013) and incorporates a number of independently developed or enhanced physical schemes and modules, including the modified convective parameterizations (Song and Zhang, 2011; Wang et al., 2016), new probability density function cloud scheme (Qin et al., 2018), new single-ice scheme (Zhao et al., 2017), four-stream shortwave radiation scheme (Zhang and Li, 2013), turbulent mountain stress scheme (Liang et al., 2017), efficient barotropic solver (Huang et al., 2016), modified ocean tidal mixing (Lin et al., 2020), wind speed-dependent sea surface albedo (Jin et al., 2011), new

https://doi.org/10.5194/egusphere-2026-6615
Preprint. Discussion started: 10 November 2026
© Author(s) 2026. CC BY 4.0 License.

thermal roughness length parameterization (Yang et al., 2008), diagnostic floe size parameterization (Lüpkes et al., 2012), global soil dataset (Shangguan et al., 2014), and new community coupler (Liu et al., 2018). The version of CIESM that participated in CMIP6 does not include carbon or nitrogen cycle processes and thus currently functions as a climate system model without biogeochemical coupling (Lin et al., 2020).

Table 1. Geometric standard deviations of the lognormal distributions used in each section of PAMT and MAM7, along with the corresponding aerosol diameter ranges. For PAMT, the size ranges correspond to the boundaries of each discrete size section, whereas for MAM7 they represent the 10th–90th percentile range of the assumed lognormal size distributions.

Aerosol module		Standard deviation	Size range (μm)
PAMT	Internally mixed aerosol		
	INT SEC1	2.0	0.016-0.081
	INT SEC2	2.0	0.081-0.406
	INT SEC3	2.0	0.406-2.048
	Externally mixed aerosol		
	BC SEC	2.0	0.016-2.048
	OA SEC	2.0	0.016-2.048
	SS SEC1	2.0	0.034-0.560
	SS SEC2	2.0	0.560-9.194
	DU SEC1	2.0	0.100-1.644
	DU SEC2	2.0	1.644-27.042
MAM7	Aitken	1.6	0.015-0.052
	Accumulation	1.8	0.056-0.260
	Primary Carbon	1.6	0.039-0.130
	Fine SS	2.0	0.095-0.560
	Fine DU	1.8	0.140-0.620
	Coarse SS	2.0	0.630-3.700
	Coarse DU	1.8	0.590-2.750

The default version of CIESM was coupled with MAM7 (Liu et al., 2012), hereafter referred to as CIESM-MAM7. However, during its participation in the CMIP6, the aerosol module was not activated. It is important to note that the MAM7 framework has continued to evolve in subsequent studies, with further developments in organic aerosol partitioning(Glotfelty et al., 2017), aerosol chemical processing (Zaveri et al., 2021), dust representation (Ke et al., 2022), and so on (Wu et al., 2018). These developments are not incorporated into the version considered in this study. Therefore, the comparison presented here specifically refers to the MAM7 implementation used in CIESM, as described by Liu et al. (2012).

MAM7 classifies aerosols into seven modes based on particle size distribution and mixing state, including Aitken, accumulation, primary carbon, fine/coarse sea salt (SS), and fine/coarse dust (DU) modes (Fig. 1b) (Liu et al., 2012). Within

https://doi.org/10.5194/egusphere-2026-6615
Preprint. Discussion started: 10 November 2026
© Author(s) 2026. CC BY 4.0 License.

each mode, the aerosol size distribution is represented by a lognormal distribution (Table 1). The overall aerosol size distribution, $n(D)$, is obtained by superimposing these seven sets of lognormal distributions:

$$n(D) = \sum_{m=1}^{7} n_m(D) = \sum_{m=1}^{7} \frac{N_m}{\sqrt{2\pi}\ln\sigma_{g,m}} \exp\left[-\frac{1}{2}\left(\frac{\ln\left(D/D_{g,m}\right)}{\ln\sigma_{g,m}}\right)^2\right], \quad (1)$$

where $n_m(D)$ is the number concentration distribution function of the aerosol mode m. N_m, $D_{g,m}$ and $\sigma_{g,m}$ are the total number concentration, median diameter and geometric standard deviation of the aerosol distribution in mode m, respectively.

MAM7 considers the following aerosol components: sulfate (SO4), ammonium (NH4), primary organic aerosol (POA), secondary organic aerosol (SOA), black carbon (BC), soil dust (DU), and sea salt (SS), which exist in either internal or external mixtures (Fig. 1b, Table 1). MAM7 classifies aerosols into two types based on whether they reside inside or outside cloud droplets, termed cloud-borne and interstitial aerosol particles, respectively. During simulations, interstitial aerosols are transported in three-dimensional space, whereas cloud-borne aerosols are only transported vertically. Interstitial aerosol species are carried as prognostic state variables and transported in three dimensions. In contrast, cloud-borne aerosol species are stored in the physics buffer and are not fully transported (except through vertical turbulent mixing), which reduces computational cost while having only a minor impact on their simulated concentrations (Ghan and Easter, 2006).

In models, variables that are advected across grids by the three-dimensional wind field are referred to as tracers. In MAM7, there are 31 tracers directly associated with aerosols, including 7 number concentration tracers (one for each mode) and 24 mass concentration tracers (one for each component in each mode) (Fig. 1b). The gaseous species that MAM7 transports include sulfur dioxide (SO_2), hydrogen peroxide (H_2O_2), dimethyl sulfide (DMS), sulfuric acid (H_2SO_4), ammonia (NH_3), and secondary organic aerosol gas-phase precursors (SOAG).

MAM7 is a two-moment scheme, meaning that it simultaneously predicts both the number concentration and mass mixing ratio of different aerosol types (Liu et al., 2012). The temporal evolution of the mass ($M_{m,s}^a$, unit: kg kg^{-1}) and number concentration (N_m^a, unit: kg^{-1}) of interstitial aerosols (represented by the superscript a) of type s in mode m can be expressed as:

$$\frac{\partial M_{m,s}^a}{\partial t} + \frac{1}{\rho}\nabla\cdot\left(\rho\vec{V}M_{m,s}^a\right) = \left(\frac{\partial M_{m,s}^a}{\partial t}\right)_{\text{emis}} + \left(\frac{\partial M_{m,s}^a}{\partial t}\right)_{\text{cond}} + \left(\frac{\partial M_{m,s}^a}{\partial t}\right)_{\text{nucl}} + \left(\frac{\partial M_{m,s}^a}{\partial t}\right)_{\text{hete}} + \left(\frac{\partial M_{m,s}^a}{\partial t}\right)_{\text{drydep}} + \left(\frac{\partial M_{m,s}^a}{\partial t}\right)_{\text{washo}} + \left(\frac{\partial M_{m,s}^a}{\partial t}\right)_{\text{resus}} + \left(\frac{\partial M_{m,s}^a}{\partial t}\right)_{\text{conv}} + \left(\frac{\partial M_{m,s}^a}{\partial t}\right)_{\text{diffus}}, \quad (2)$$

$$\frac{\partial N_m^a}{\partial t} + \frac{1}{\rho}\nabla\cdot\left(\rho\vec{V}N_m^a\right) = \left(\frac{\partial N_m^a}{\partial t}\right)_{\text{emis}} + \left(\frac{\partial N_m^a}{\partial t}\right)_{\text{coag}} + \left(\frac{\partial N_m^a}{\partial t}\right)_{\text{nucl}} + \left(\frac{\partial N_m^a}{\partial t}\right)_{\text{hete}} + \left(\frac{\partial N_m^a}{\partial t}\right)_{\text{drydep}} + \left(\frac{\partial N_m^a}{\partial t}\right)_{\text{washo}} + \left(\frac{\partial N_m^a}{\partial t}\right)_{\text{resus}} + \left(\frac{\partial N_m^a}{\partial t}\right)_{\text{conv}} + \left(\frac{\partial N_m^a}{\partial t}\right)_{\text{diffus}}. \quad (3)$$

Similarly, the temporal evolution of the mass ($M_{m,s}^c$, unit: kg kg^{-1}) and number concentration (N_m^c, unit: kg^{-1}) of cloud-borne aerosols (represented by the superscript c) of type s in mode m can be expressed as:

$$\frac{\partial M_{m,s}^c}{\partial t} = \left(\frac{\partial M_{m,s}^c}{\partial t}\right)_{\text{hete}} + \left(\frac{\partial M_{m,s}^c}{\partial t}\right)_{\text{wetox}} + \left(\frac{\partial M_{m,s}^c}{\partial t}\right)_{\text{drydep}} + \left(\frac{\partial M_{m,s}^c}{\partial t}\right)_{\text{raino}} + \left(\frac{\partial M_{m,s}^c}{\partial t}\right)_{\text{resus}} + \left(\frac{\partial M_{m,s}^c}{\partial t}\right)_{\text{conv}} + \left(\frac{\partial M_{m,s}^c}{\partial t}\right)_{\text{diffus}}, \quad (4)$$

https://doi.org/10.5194/egusphere-2026-6615
Preprint. Discussion started: 10 November 2026
© Author(s) 2026. CC BY 4.0 License.

$$\frac{\partial N_m^c}{\partial t} = \left(\frac{\partial N_m^c}{\partial t}\right)_{\text{hete}} + \left(\frac{\partial N_m^c}{\partial t}\right)_{\text{drydep}} + \left(\frac{\partial N_m^c}{\partial t}\right)_{\text{raino}} + \left(\frac{\partial N_m^c}{\partial t}\right)_{\text{resus}} + \left(\frac{\partial N_m^c}{\partial t}\right)_{\text{conv}} + \left(\frac{\partial N_m^c}{\partial t}\right)_{\text{diffus}}, \quad (5)$$

where t represents time, $\vec{V}$ is the three-dimensional wind field, and ρ is the air density. The terms on the right-hand side of the equations represent sources and sinks that affect aerosol mass and number concentration, including emissions (emis), condensation (cond), coagulation (coag), aerosol nucleation/new particle formation (nucl), droplet/ice heterogeneous nucleation (hete), dry deposition (drydep), wet deposition (raino: rainout, washo: washout), resuspension (resus), aqueous-phase chemistry (wetox), vertical transport by convection (conv), and vertical mixing by turbulence (diffus). The parameterizations used for these processes are summarized in Table 2.

Table 2. Aerosol-related processes and their parameterizations in CIESM-PAMT and CIESM-MAM7.

Aerosol processes	CIESM-PAMT	CIESM-MAM7
Size distribution	Piecewise lognormal approximation method (von Salzen, 2006)	Modal approach (Liu et al., 2012)
Emission inventory	CMIP6 and AeroCom inventories (Hoesly et al., 2018)	CMIP6 and AeroCom inventories (Hoesly et al., 2018)
Dust emission	Size-resolved dust scheme (Peng et al., 2012)	DEAD-based dust emission scheme (Mahowald et al., 2006a, b; Okin, 2008; Yoshioka et al., 2007)
Sea salt emission	Observation-based sea salt scheme (Lewis and Schwartz, 2004; Ma et al., 2008)	Laboratory-based sea salt scheme (Mårtensson et al., 2003; Monahan et al., 1986)
Gas-phase chemistry	DMS/SO_2 oxidation and H_2O_2 chemistry (Emmons et al., 2010)	DMS/SO_2 oxidation and H_2O_2 chemistry (Emmons et al., 2010)
Aqueous-phase chemistry	H_2O_2/O_3 oxidation with iterative ion-balance pH calculation (von Salzen et al., 2000)	H_2O_2/O_3 oxidation with electroneutrality-based pH diagnosis (Seinfeld and Pandis, 2006; Tie et al., 2001)
Aerosol nucleation	Sulfuric acid–ammonia–organics-water nucleation with cosmic-ray effects (Dunne et al., 2016; Kulmala et al., 1998; Merikanto et al., 2007)	Sulfuric acid–ammonia–water nucleation via lookup tables (Merikanto et al., 2007)
Condensation	Fuchs–Sutugin-based condensation (Hanson, 2005; Russell et al., 1994; von Salzen, 2006)	Mass-transfer-based condensation (Binkowski and Shankar, 1995; Pöschl et al., 1998; Seinfeld and Pandis, 2006)
Black carbon aging	e-folding BC aging (Croft et al., 2005)	Three-layer SO4 coating (Liu et al., 2012)
Coagulation	Sectional coagulation scheme with 21 size bins and Brownian diffusion (Seinfeld and Pandis, 2006; Tzivion et al., 1987)	Mode-based coagulation scheme using the CMAQ numerical approach (Binkowski and Roselle, 2003)
Water uptake	RH-dependent hygroscopicity with explicit Kelvin-effect treatment (this publication)	Fixed hygroscopicity with implicit Kelvin-effect treatment (Ghan and Zaveri, 2007; Neale et al., 2012; Petters and Kreidenweis, 2007)
Cloud droplet nucleation	QDGE scheme (Wang et al., 2022)	ARG scheme (Abdul-Razzak and Ghan, 2000)
Ice nucleation	LP scheme (Liu et al., 2007)	LP scheme (Liu et al., 2007)
Dry deposition	Revised Zhang scheme with tunable, species-dependent sticking efficiency (Emerson et al., 2020; Seinfeld and Pandis, 2006; Zhang et al., 2001)	Zhang scheme with wet/dry surface-dependent sticking efficiency (Zhang et al., 2001)
Wet deposition	Cloud-type-dependent rainout and rain/snow washout with resuspension (Croft et al., 2009; Scott, 1978)	Cloud-water-loss-based rainout and size-dependent washout with resuspension (Barth et al., 2000; Easter et al., 2004; Rasch et al., 2000)

https://doi.org/10.5194/egusphere-2026-6615
Preprint. Discussion started: 10 November 2026
© Author(s) 2026. CC BY 4.0 License.

2.2 Introduction to PAMT

2.2.1 Overview of the PAMT

The Piecewise Lognormal Approximation Model (PAM) was initially developed for simulations of aerosol chemical and microphysical processes in the Canadian Atmospheric Model (CanAM5) (Cole et al., 2023), as a more comprehensive alternative to the default bulk aerosol scheme in CanAM5. CanAM5-PAM was previously used to assess Short-Lived Climate Forcers (SLCFs) and their impacts on global air quality and the Arctic climate (AMAP, 2021; von Salzen et al., 2022; Whaley et al., 2022). More recently, CanAM5.1-PAM was used to assess the contribution of declining aerosol concentrations on clouds over the Northeast Pacific and North Atlantic (von Salzen et al., 2025). In addition to these studies, von Salzen (2006) evaluated the parameterization of gas-to-particle conversion and the parameterization of aerosol activation was evaluated by Wang et al. (2022). Ma et al. (2008) and Peng et al. (2012) compared results from CanAM-PAM with observations of sea salt and soil dust, respectively. Black carbon aerosol optical properties were analysed by Digby et al. (2025).

Even though CanAM5-PAM reproduces observed Arctic aerosol surface concentrations and vertical profiles well, in comparison to other models (AMAP, 2021; Whaley et al., 2022), a comprehensive analysis of simulated global aerosol and cloud properties is currently lacking. Furthermore, it is currently unknown whether PAM can also be used in combination with other global atmospheric and climate models, in addition to CanAM. The objective of the present study is to address these issues by introducing PAMT (i.e., PAM for Tsinghua University) in CIESM and to compare results with a wide range of different aerosol and cloud observational data sets. Furthermore, this approach allows direct comparisons with the MAM7 aerosol module in CIESM, which provides unique opportunities for direct comparisons of two different aerosol schemes in the same host model. Therefore, the approach here goes beyond earlier multi-model intercomparisons for aerosols and clouds, which cannot distinguish between differences in aerosol and other atmospheric processes in the models.

It should be noted that PAM can operate as a standalone system and can therefore be regarded as a model, rather than merely a module like MAM. In this study, it is simply coupled with CIESM and used as a module within the overall framework. Nevertheless, its applicability extends well beyond this specific configuration.

PAMT differs significantly from MAM7 in terms of the numerical representation of aerosol size distribution, parameterizations of various source and sink processes, aerosol activation, aerosol mixing state, and optical calculations, as summarized in Table 2. The following sections provide a detailed description of the specific parameterizations implemented in PAMT.

2.2.2 Aerosol Size Distributions in PAMT

PAMT represents aerosol size distributions using the Piecewise Lognormal Approximation (PLA) method (von Salzen, 2006). The approach combines features of two commonly used approaches for describing the aerosol size distribution (i.e., aerosol spectrum) in models: the bin and modal approaches. In general, the bin approach divides the aerosol spectrum into

https://doi.org/10.5194/egusphere-2026-6615
Preprint. Discussion started: 10 November 2026
© Author(s) 2026. CC BY 4.0 License.

discrete sections, potentially allowing a detailed representation of particle-size features, but it is computationally expensive and thus mainly applied in parcel or chemistry models. The modal approach is less detailed but computationally efficient, making it suitable for climate models, with MAM7 serving as a representative example. The PLA method combines the advantages of both approaches and integrates them into a unified framework: PLA first divides the aerosol spectrum into several contiguous size sections (with the number of sections denoted as $ISEC$) and assumes that the aerosol size distribution in each section follows a lognormal distribution, with the distribution parameters determined by the mass/number concentrations within each section. von Salzen (2006) showed that the PLA scheme performs well in terms of both accuracy and computational efficiency.

Accordingly, the aerosol number concentration distribution ($n(\varphi)$) in the PLA can be written as:

$$n(\varphi) = \sum_{i=1}^{ISEC} n_i(\varphi) = \sum_{i=1}^{ISEC} n_{0,i} \exp\left[-\psi_i\left(\varphi - \varphi_{0,i}\right)^2\right] H\left(\varphi - \varphi_{i-\frac{1}{2}}\right) H\left(\varphi_{i+\frac{1}{2}} - \varphi\right), \quad (6)$$

where $n_i(\varphi)$ is the distribution function of aerosol number concentration in section i, φ is the dimensionless size parameter defined as $\varphi \equiv \ln(R_p/R_0)$, R_p is the particle radius, and R_0 is a reference radius of 1 μm. The parameters $n_{0,i}$, ψ_i, and $\varphi_{0,i}$ represent the magnitude, width, and modal location of the distribution, respectively. $H(x)$ is the Heaviside step function, which constrains the lognormal distribution in each section to the particle-size interval between $\varphi_{i-1/2}$ and $\varphi_{i+1/2}$. In CIESM-PAMT, ψ_i is prescribed according to the standard deviation of the aerosol spectrum, while $n_{0,i}$ and $\varphi_{0,i}$ are updated at each time step based on simulated mass and number concentrations, enabling dynamic adjustment of the aerosol spectrum. In addition, the number of sections $ISEC$ is a tuneable parameter, and increasing it generally enhances the accuracy of the size-distribution representation (von Salzen, 2006). In the version of PAMT used in this study, $ISEC$ is set to 3 internally mixed sections and 6 externally mixed sections, as shown in Fig. 1a and Table 1.

In PAMT, the PLA is applied to 5 different aerosol species: primary BC (BC SEC); primary OA (OA SEC); internally mixed BC, OA, and SO4 (INT SEC1/2/3); DU (DU SEC1/2); and SS (SS SEC1/2) (Fig. 1a). The particle size ranges and geometric standard deviations of these modes are listed in Table 1. Internally mixed SO4, BC, and OA is represented using three piecewise lognormal modes. Primary BC and OA are each treated as externally mixed and represented by a single lognormal mode. DU and SS are also each treated as externally mixed and represented by two piecewise lognormal modes.

Similar to MAM7, PAMT also accounts for cloud-borne and interstitial aerosol particles, but it does not distinguish between them as explicitly as MAM7 does. The proportions of aerosols in the cloudy and clear-sky portions of the grid cells are diagnosed from the all-sky aerosol. Specifically, the mixing ratios in the cloudy and clear portions are calculated from the all-sky mixing ratios X, which are saved and advected in the model. dX is the mixing ratio difference between the cloudy and clear portions, which is calculated in the model based on the parameterized cloudy and clear-sky processes whenever clouds are present in a grid cell:

$$X_{cld} = X + \frac{\mathrm{d}X}{1-f_c}, \; X_{clr} = X - \frac{\mathrm{d}X}{f_c}, \quad (7)$$

https://doi.org/10.5194/egusphere-2026-6615
Preprint. Discussion started: 10 November 2026
© Author(s) 2026. CC BY 4.0 License.

where f_c is the cloud fraction. The aerosol parameterizations distinguish between the sources and sinks in cloudy and clear portions of the grid cells and the equations are coupled through the emissions, dry deposition, convective transport, advection, and diffusion of all-sky aerosols ($dX = 0$ for these processes). And the time evolution of the mixing ratios for mass ($M_{i,j}$, unit: kg kg^{-1}) and number concentration (N_i, unit: kg^{-1}) of all-sky aerosol type j in section i can be expressed as:

$$\frac{\partial M_{i,j}}{\partial t} + \frac{1}{\rho}\nabla\cdot\left(\rho\vec{V}M_{i,j}\right) = \left(\frac{\partial M_{i,j}}{\partial t}\right)_{\text{emis}} + \left(\frac{\partial M_{i,j}}{\partial t}\right)_{\text{wetox}} + \left(\frac{\partial M_{i,j}}{\partial t}\right)_{\text{cond}} + \left(\frac{\partial M_{i,j}}{\partial t}\right)_{\text{nucl}} + \left(\frac{\partial M_{i,j}}{\partial t}\right)_{\text{hete}} + \left(\frac{\partial M_{i,j}}{\partial t}\right)_{\text{drydep}} + \left(\frac{\partial M_{i,j}}{\partial t}\right)_{\text{raino}} + \left(\frac{\partial M_{i,j}}{\partial t}\right)_{\text{washo}} + \left(\frac{\partial M_{i,j}}{\partial t}\right)_{\text{resus}} + \left(\frac{\partial M_{i,j}}{\partial t}\right)_{\text{conv}} + \left(\frac{\partial M_{i,j}}{\partial t}\right)_{\text{diffus}}, \quad (8)$$

$$\frac{\partial N_i}{\partial t} + \frac{1}{\rho}\nabla\cdot\left(\rho\vec{V}N_i\right) = \left(\frac{\partial N_i}{\partial t}\right)_{\text{emis}} + \left(\frac{\partial N_i}{\partial t}\right)_{\text{coag}} + \left(\frac{\partial N_i}{\partial t}\right)_{\text{nucl}} + \left(\frac{\partial N_i}{\partial t}\right)_{\text{hete}} + \left(\frac{\partial N_i}{\partial t}\right)_{\text{drydep}} + \left(\frac{\partial N_i}{\partial t}\right)_{\text{raino}} + \left(\frac{\partial N_i}{\partial t}\right)_{\text{washo}} + \left(\frac{\partial N_i}{\partial t}\right)_{\text{resus}} + \left(\frac{\partial N_i}{\partial t}\right)_{\text{conv}} + \left(\frac{\partial N_i}{\partial t}\right)_{\text{diffus}}, \quad (9)$$

where the meanings of the subscripts are consistent with those in MAM7.

PAMT includes 24 aerosol-related tracers, including 9 number tracers (3 for internally mixed and 6 for externally mixed aerosols) and 15 mass tracers (9 internally mixed and 6 externally mixed). A larger number of tracers increases the amount of inter-grid transport required and therefore the computational cost. Therefore, PAMT is theoretically more computationally efficient than MAM7 because of fewer tracers. The gaseous species considered in PAMT include SO_2, H_2O_2, DMS, H_2SO_4, and SOAG. However, PAMT does not explicitly simulate the atmospheric evolution of NH3. Instead, it assumes that [SO_4^{2-}] exists entirely in the form of $(NH_4)_2SO_4$ and diagnoses [NH_4^+] from the simulated [SO_4^{2-}].

The simulated aerosol size distribution depends not only on how each aerosol module numerically represents the spectrum but also on the aerosol source and sink processes. As shown in Fig. 2, different sources and sinks affect different particle size ranges. In the following sections, we describe these parameterizations and highlight the similarities and differences between PAMT and MAM7.

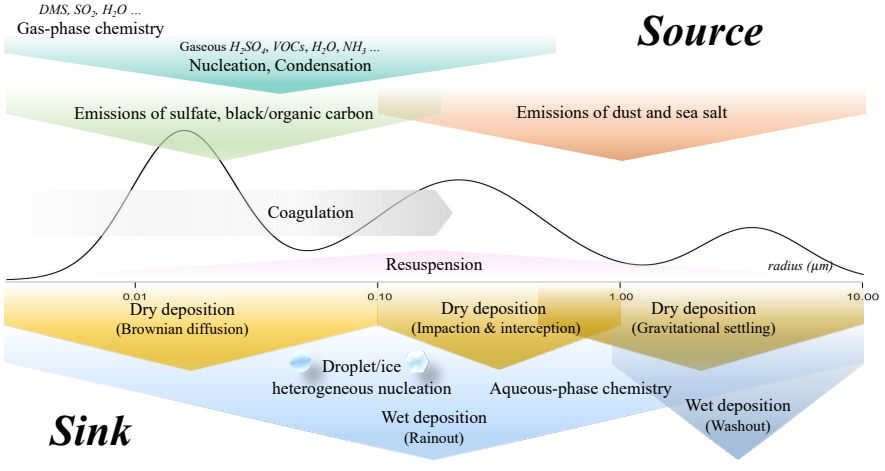


Figure 2. Schematic of major source and sink processes affecting aerosol size in PAMT and MAM7.

https://doi.org/10.5194/egusphere-2026-6615
Preprint. Discussion started: 10 November 2026
© Author(s) 2026. CC BY 4.0 License.

2.2.3 Aerosol Emissions

The emission inventories provided by CMIP6 include emissions of SO_2, NH_3, gaseous precursors of organic aerosols (VOCs), primary BC and OA from different emission sectors for the period 1750–2014 (Hoesly et al., 2018). However, it does not specify emission injection heights for and size distributions of primary emitted particles and precursor gases, for which we have followed the AeroCom protocols (Dentener et al., 2006). In addition, aviation emissions are released at prescribed altitudes according to the CMIP6 dataset (Hoesly et al., 2018). Surface emissions of DMS are based on the year-2000 dataset from the AeroCom initiative. Following the approach used in the Fifth Assessment Report (Neale et al., 2012), this study assumes that 2.5% of SO_2 emissions (in molar fraction) are emitted as primary SO4. In MAM7, the size distribution of emitted aerosols is assumed to follow a lognormal distribution as described in Eq. (1). The geometric standard deviation and median diameter for each source type are provided in Table 3. The volume-mean diameter is calculated as $D_{emit} = D_g \exp\left(1.5 \times \left(\ln\sigma_g\right)^2\right)$. Assuming spherical particles, the emitted number concentration (E_{number}) is derived from the emitted mass concentration (E_{mass}) using $E_{number} = E_{mass}/(\pi/6 \times \rho_a D_{emit}^3)$, where ρ_a is the particle density. For BC and OA, all emissions are assigned to the primary carbon mode. For SO4, emissions with D_{emit} equals 0.134 μm and 0.261 μm are assigned to the accumulation mode, while those with D_{emit} =0.0504 μm are assigned to the Aitken mode.

Table 3. Size distribution parameters for different types of primary emission aerosols (Liu et al., 2012).

Emission Source		Geometric standard deviation σ_g	Number mode diameter D_g（μm）	Volume-mean diameter D_{emit}（μm）
BC/OC		1.8	0.080	0.134
SO4	Domestic/transportation/volcano (Aitken)	1.8	0.030	0.0504
	Forest fire/grass fire/waste/agriculture/volcano (accum.)	1.8	0.080	0.134
	Energy/industry/shipping	-	-	0.261

In PAMT, the initial surface emissions of aerosol mass and number concentrations are kept identical to those in MAM7. These emissions are then distributed into the corresponding PAMT sections based on its prescribed particle size structure (Table 1 and Eq. (6)). Overall, the primary emissions of SO4, BC, and OA, as well as emissions of SO_2, DMS, and VOCs, are consistent between PAMT and MAM7. However, their treatment of secondary formation of SO4 and OA differs, as described in Sections 2.2.4–2.2.6. Dust and sea salt emissions are computed online in both PAMT and MAM7, although the specific parameterizations differ.

In PAMT, dust emissions occur only over bare soil areas, and the emission flux is proportional to the bare soil fraction (F_{bg}). Dust generation is essentially driven by the movement of soil particles induced by wind stress. A force balance on soil particles includes gravity, inter-particle cohesion, and surface wind shear stress (Marticorena and Bergametti, 1995). These forces together determine the threshold friction velocity for dust emission, u_{*t}. The actual dust emission flux is determined by the friction velocity (u_*), which is related to the 10-meter wind speed (U_{10}) and near-surface gusts (U_{gust}), that is, $u_* \propto$

https://doi.org/10.5194/egusphere-2026-6615
Preprint. Discussion started: 10 November 2026
© Author(s) 2026. CC BY 4.0 License.

$\left(U_{10}^2 + U_{gust}^2\right)^{1/2}$. When $u_* > u_{*t}$, the local wind stress is sufficient to overcome particle gravity and cohesion, leading to dust emission in that grid cell. The dust emission flux scales approximately with u_*^3 (Marticorena and Bergametti, 1995).

PAMT uses 17 soil types, each defined by the fractional composition of four particle sizes: coarse sand, medium/fine sand, silt, and clay, with spatial areas denoted as A_{st}. The mass flux of dust of a given dry particle size r_{du} ($F_{dust}(r_{du})$) is given by Peng et al. (2012):

$$F_{dust}(r_{du}) \propto \sum_{st=1}^{17} u_*\left(z_0, q_{surf}\right)^3 A_{st} S_{st}(r_{du}), \quad (10)$$

where z_0 is the surface roughness, q_{surf} is soil moisture, and $S_{st}(r_{du})$ is the particle size distribution for each soil type. In PAMT, emitted dust aerosols are divided into two sections. Within each section, $F_{dust}(r_{du})$ is constrained by F_{bg}, and then integrated over all particle sizes in that section to obtain the mass emission flux of dust.

In MAM7, dust aerosol emissions are calculated within the land surface module using the Dust Entrainment and Deposition Model (Mahowald et al., 2006a, b; Yoshioka et al., 2007). When the leaf area index falls below 0.3 m²/m², the fraction of the grid cell available for dust generation increases linearly as vegetation cover decreases (Okin, 2008). However, unlike PAMT, MAM7 does not include a detailed classification of surface types in its dust emission scheme.

The parameterization of sea salt in PAMT (Ma et al., 2008) follows the observationally based scheme of Lewis and Schwartz (2004), with retuning of parameters. The number size distribution of emitted sea salt aerosols at a height of 5-20 m above the surface can be expressed as:

$$n(r_{ss}) = \frac{dN_{ss}}{d\log(r_{ss})} = 30400(U_{10})^2 \exp\left\{-\frac{1}{2}\left[\frac{\ln(r_{ss}/0.068)}{\ln 2.8}\right]^2\right\}, \quad (11)$$

where N_{ss} is the emitted sea salt number concentration (unit: number of particles per kg), r_{ss} is the dry particle radius. This parameterization applies to sea salt aerosols, which are directly injected into the lowest model layer.

In MAM7, sea salt aerosols are treated using a size-segregated approach. For particles with geometric radii smaller than 1.4 μm, the parameterization of Mårtensson et al. (2003) is applied, whereas for larger particles, the scheme of Monahan et al. (1986) is used. Both parameterizations describe sea salt mass fluxes as functions of wind speed and were originally derived from laboratory experiments, assuming an equilibrium between sea salt emissions and deposition. In contrast, PAMT does not explicitly predict sea salt emission fluxes; instead, it employs parameterizations of observed aerosol size distributions under varying wind speeds based on multiple field experiments.

2.2.4 Chemistry

The PAMT module implemented in CIESM adopts the same gas-phase chemistry as in MAM7 (Emmons et al., 2010), including the production and consumption of H_2O_2, the oxidation of SO_2 and DMS, and the formation of gaseous H_2SO_4. In both PAMT and MAM7, the aqueous-phase chemistry accounts for the oxidation of H_2O_2 and O_3 in the volume of the droplets, meaning that only cloud-borne aerosols are affected, although the calculation methods for droplet pH differ between the two modules. In PAMT, the pH of solution droplets influences the rates of aqueous-phase reactions and is

https://doi.org/10.5194/egusphere-2026-6615
Preprint. Discussion started: 10 November 2026
© Author(s) 2026. CC BY 4.0 License.

calculated from the ion balance equation, that is, $[H^+] + [NH_4^+] + [Na^+] = [OH^-] + 2[SO_4^{2-}] + 2[SO_3^{2-}] + [HSO_3^-] + [NO_3^-] + [HCO_3^-] + [Cl^-]$. Monthly mean concentrations of nitrate and nitric acid are prescribed, and the nitrate content in cloud droplets is calculated by assuming thermodynamic equilibrium between gas-phase nitric acid and dissolved nitrate (von Salzen et al., 2000). The ion balance equation in PAMT is solved iteratively (von Salzen et al., 2000). In MAM7, the droplet pH is diagnosed from electroneutrality, considering major ions such as cloud-borne $[SO4^{2-}]$ and $[NH4^+]$ ion concentrations as well as dissolved trace gases following Henry's law equilibrium (Tie et al., 2001). Aqueous oxidation of SO_2 by H_2O_2 and O_3 and irreversible uptake of H_2SO_4 are included (Seinfeld and Pandis, 2006).

2.2.5 Aerosol Nucleation

Aerosol nucleation refers specifically to the formation of new particles from gaseous precursors. In the PAMT module, three options are available for aerosol nucleation of sulfate aerosols. The first, developed by Kulmala et al. (1998), describes homogeneous nucleation of sulfate particles considering both sulfuric acid and water vapor. The second, by Merikanto et al. (2007), uses a lookup table approach for nucleation involving sulfuric acid, ammonia, and water vapor. The third, based on cloud chamber experiments, was proposed by Dunne et al. (2016) and considers sulfuric acid, ammonia, organics, and water vapor. Currently, PAMT uses the parameterization proposed by Dunne et al. (2016), assuming sufficient ammonia is available for the formation of ammonium sulfate and accounting for the impact of galactic cosmic rays on nucleation rates. In contrast, MAM7 employs the scheme developed by Merikanto et al. (2007). Including ammonia in homogeneous nucleation increases the production of new particles, significantly affecting the number concentration of sulfate aerosols (Dunne et al., 2016).

2.2.6 Condensation and BC Aging

In PAMT, the condensation of gaseous H_2SO_4 and VOCs can coat pre-existing aerosols, such as SO4, SS, and OA, altering their composition and hygroscopicity. For the mass concentration of aerosol type j in section i ($M_{i,j}$), the mass increase due to gas condensation of a non-volatile gas with the concentration C_j (in kg kg^{-1}) is expressed using the modified form of the Fuchs-Sutugin equation (Russell et al., 1994; von Salzen, 2006) :

$$\left(\frac{\partial M_{i,j}}{\partial t}\right)_{\text{cond}} = 4\pi C_j D \int_{\varphi_{i-\frac{1}{2}}}^{\varphi_{i+\frac{1}{2}}} F\, A\, r\, R_p\, n(\varphi)\, d\varphi, \tag{12}$$

where D is the diffusivity of the gas in air (m^2 s^{-1}), r is the ratio of the total particle radius over the dry particle radius, F is a coefficient correcting for free molecular effects and A is a coefficient correcting for the interfacial mass transport limitations described by an accommodation coefficient (currently set to unity, Hanson, 2005). The aging of hydrophobic BC is treated using an e-folding method, with daytime and nighttime aging time scales of 1 hour and 24 hours (Croft et al., 2005), respectively. Consequently, the externally mixed (hydrophobic) BC transitions into the internally mixed aerosol (hydrophilic) mode after aging.

https://doi.org/10.5194/egusphere-2026-6615
Preprint. Discussion started: 10 November 2026
© Author(s) 2026. CC BY 4.0 License.

In MAM7, condensation of gaseous H_2SO_4, NH_3, and SOA onto aerosol modes is treated dynamically using standard mass transfer formulations (Seinfeld and Pandis, 2006) integrated over each modal size distribution (Binkowski and Shankar, 1995). A sticking coefficient of 0.65 is applied to H_2SO_4 (Pöschl et al., 1998) and assumed for other species. H_2SO_4 and NH_3 uptake are treated as irreversible, with NH_3 condensation ceasing when the NH4/SO4 molar ratio reaches 2. In contrast, SOA condensation is reversible and governed by its equilibrium vapor pressure. A three-layer sulfate coating is applied to freshly emitted BC, allowing them to age into the accumulation mode (Liu et al., 2012).

2.2.7 Aerosol Coagulation

In PAMT, the parameterization of aerosol coagulation is based on the approach by Tzivion et al. (1987) which approximates the aerosol number and mass size distributions by piecewise linear functions with 21 sections (Fraser-Leach et al., in preparation). Coagulation is only considered for internally mixed aerosol. The coagulation kernel is calculated by assuming Brownian diffusion and using Fuchs' interpolation method (Seinfeld and Pandis, 2006).

In contrast, MAM7 primarily treats coagulation as the conversion of number concentrations between different modes. Its numerical treatment is relatively simple, relying on methods from the Community Multiscale Air Quality model (Binkowski and Roselle, 2003), which essentially provides a numerical solution to the coagulation equation. Therefore, PAMT and MAM7 differ significantly in how they handle coagulation: PAMT uses a continuous and more densely segmented size spectrum, allowing for more precise coagulation calculations.

2.2.8 Water Uptake

PAMT and MAM7 both parameterize water uptake based on Köhler theory (Ghan and Zaveri, 2007; Köhler, 1936). However, because the two modules treat aerosol mixing states differently, the hygroscopicity of internally mixed particles also differs. Table 4 summarizes the hygroscopicity parameters (κ) used for various aerosol components in PAMT and MAM7 (Neale et al., 2012; Petters and Kreidenweis, 2007). For internally mixed aerosols composed of multiple species, the bulk hygroscopicity is calculated as a volume-weighted average of the component hygroscopicity, using the volume fractions of each species in the solution droplet as weights.

It should be noted that the κ values in Table 4 are given for relative humidity values above 99%. At lower humidity, the hygroscopicity can deviate substantially from these assumed constants. In PAMT, therefore, κ varies with relative humidity to more accurately represent aerosol hygroscopic growth, which were determined based on simulations with the Aerosol Inorganic Model (AIM) (Wexler and Clegg, 2002). In contrast, the current MAM7 does not account for relative-humidity dependence of κ.

In PAMT, the aerosol water content in each aerosol section is iteratively calculated to include the effect of size-dependent curvature (Kelvin effect). MAM7 also accounts for the Kelvin effect, but because it uses a modal approximation, the effect is considered implicitly through the Köhler-theory-based calculation of the critical supersaturation (Abdul-Razzak and Ghan, 2000).

https://doi.org/10.5194/egusphere-2026-6615
Preprint. Discussion started: 10 November 2026
© Author(s) 2026. CC BY 4.0 License.

Table 4. Hygroscopicity parameters of different aerosol components in PAMT and MAM7.

PAMT	SO4	BC	Internal OA	External OA	DU	SS
	0.507	0	0.14	0	0.05	1.28
MAM7	SO4 / NH4	BC	POA	SOA	DU	SS
	0.507	1e-10	0.10	0.14	0.068	1.16

2.2.9 Cloud Droplet Nucleation

Cloud droplets form when the supersaturation of vapor exceeds a critical value, allowing airborne aerosols to activate and grow by condensation. This process is known as aerosol activation or cloud droplet nucleation. The theoretical basis for describing activation is the Köhler equation and the droplet condensational growth equation (Köhler, 1936; Seinfeld and Pandis, 2006). However, analytical solutions to these equations are not available, so climate models rely on parameterized schemes. PAMT employs a cloud droplet nucleation scheme based on the Quasi-steady state approximated Droplet Growth Equation (QDGE), a numerically efficient method (Wang et al., 2022). The QDGE scheme captures subgrid-scale vertical activation processes and incorporates tunable parameters that allow an optimal balance between computational accuracy and efficiency. Compared with conventional physics-based parameterizations, it delivers improved performance in estimating the maximum supersaturation (S_{max}) and cloud droplet number concentration (Wang et al., 2022).

In large-scale stratiform clouds, S_{max}, typically <0.2%, occurs roughly 100 m above cloud base. This implies that the vertical gradient of supersaturation (S) is usually below 0.002% m^{-1} (Pandis et al., 1990). Based on this, QDGE assumes that S remains quasi-steady within a certain vertical range during numerical integration. Under this assumption, the evolution of activated aerosol particles can be written as:

$$\frac{dx}{du} = \delta - a_0\left(\frac{b_0}{x^{1/2}} - \frac{1}{x^{3/2}}\right), \tag{13}$$

where $x = {r_w}^2/2$, $u = tG \cdot \lfloor S \rfloor$, $a_0 = C_n/(2^{3/2} \cdot \lfloor S \rfloor)$, $b_0 = 2C_r/C_n$, r_w is the wet aerosol radius, δ is the sign function, t is the lifting time of an air parcel from cloud base, and the parameters G, C_n, and C_r encapsulate the effects of cloud thermodynamic conditions and the physicochemical properties of aerosol particles and cloud droplets (Wang et al., 2022). In practice, x is obtained from precomputed lookup tables generated using a parcel model based on a_0 and b_0, allowing QDGE to achieve high computational efficiency without sacrificing accuracy.

Since the vertical grid spacing (Δz) in climate models is typically too coarse to satisfy the quasi-steady assumption, QDGE subdivides each model layer into N_{sub} subgrid layers with the height $\Delta z_s = \Delta z/N_{sub}$. A typical Δz_s is 1–10 m, ensuring that the scheme adequately resolves S_{max} within Δz. By applying moist static energy conservation and iterative methods, the scheme solves for the parameters in Eq. (13) and retrieves the S_i in each subgrid layer. From the vertical profile of S_i, the S_{max} can be obtained. The corresponding critical radius is then computed from the Köhler equation, and integrating the

https://doi.org/10.5194/egusphere-2026-6615
Preprint. Discussion started: 10 November 2026
© Author(s) 2026. CC BY 4.0 License.

aerosol size distribution above this critical radius yields the initial cloud droplet number concentration (i.e., the number concentration of initial cloud-borne aerosols), which subsequently participates in cloud microphysical processes.

Overall, QDGE can be regarded as a simplified parcel model, enabling accurate and efficient calculation of S_{max}. In contrast, MAM7 uses the physics-based Abdul-Razzak and Ghan (ARG) parameterization (Abdul-Razzak and Ghan, 2000), which does not explicitly treat subgrid-scale processes and treats different aerosol modes as externally mixed populations while assuming internal mixing among aerosol species within each mode, in contrast to the treatment of aerosol mixing in PAMT.

2.2.10 Ice Nucleation

PAMT and MAM7 both use the default ice nucleation scheme implemented in CIESM (Liu et al., 2007). In CIESM, aerosol-induced ice nucleation is parameterized for both mixed-phase clouds and cirrus clouds (pure ice clouds). For cirrus clouds (T < –35 °C), the Liu–Penner (LP) scheme is applied (Liu et al., 2007; Liu and Penner, 2005), which accounts for the competition between homogeneous freezing of SO4 aerosols and heterogeneous freezing induced by DU particles. Because the role of BC as ice-nucleating particles (INPs) remains highly uncertain (Gettelman et al., 2012), the default CIESM configuration does not include BC-induced ice nucleation.

In the LP scheme, SO4 aerosols in the accumulation mode with diameters larger than 0.1 μm can participate in homogeneous freezing, while DU aerosols in the coarse mode are considered potential INPs for heterogeneous immersion freezing. Subgrid vertical velocity required in the nucleation calculations is diagnosed from turbulent kinetic energy (TKE). For mixed-phase clouds (–40 °C < T < –3 °C), condensational and deposition freezing follow Meyers et al. (1992) and immersion freezing follows Bigg (1953), with both depending solely on temperature and not explicitly accounting for aerosol effects. Contact freezing follows the parameterization of Young (1974), in which coarse-mode DU aerosols are considered potential INPs.

2.2.11 Dry Deposition

Both PAMT and MAM7 employ aerosol dry deposition schemes based on the parameterization developed by Zhang et al. (2001). The dry deposition velocity (V_d) of aerosol particles can be expressed as:

$$V_d = V_g + \frac{1}{(R_a + R_s)}, \tag{14}$$

where V_g is the gravitational settling velocity, R_a is the aerodynamic resistance above the canopy, and R_s is the surface resistance. However, PAMT and MAM7 differ in their practical implementations. PAMT introduces observational constraints and uses the version revised by Emerson et al. (2020) based on Zhang et al. (2001), and updates the gravitational settling scheme following Seinfeld and Pandis (2006) . In MAM7, aerosol particles are separated into two categories: the deposition velocity of interstitial aerosols is calculated using their wet radius, while that of cloud-borne aerosols is derived from droplet size.

https://doi.org/10.5194/egusphere-2026-6615
Preprint. Discussion started: 10 November 2026
© Author(s) 2026. CC BY 4.0 License.

In both PAMT and MAM7, incomplete particle attachment during gravitational dry deposition is represented by a Stokes-number-dependent sticking factor, meaning that the fraction of particles adhering to the surface decreases with increasing Stokes number. In MAM7, this factor is set to 1 for wet surfaces and decays exponentially for dry surfaces. In PAM, a similar exponential dependence is applied, but it is combined with a tunable STICK parameter (0.1 for externally mixed BC and OA, 1 for other species) and modified collection efficiency formulas, providing greater flexibility to account for different surface types and particle sizes.

2.2.12 Wet Deposition

In PAMT, wet deposition is computed separately for large-scale stratiform clouds and convective clouds, including both rainout and washout. The activation parameterization simulates the critical aerosol size, which separates interstitial and cloud-borne aerosols in the cloudy part of the grid cell from each other. We only allow rainout to affect cloud-borne aerosols, similar to aqueous-phase chemistry. Interstitial aerosol concentrations are affected by washout.

Rainout refers to the removal of aerosols from the atmosphere after they are activated into cloud droplets and subsequently converted into precipitation. In PAMT, the parameterization of aerosol rainout is expressed as:

$$\left(\frac{\partial M_{i,j}}{\partial t}\right)_{\text{raino}} = -\frac{(M_{i,j})_{cld}\cdot f_{M_{i,j}}^{act}}{\tau}, \left(\frac{\partial N_i}{\partial t}\right)_{\text{raino}} = -\frac{(N_i)_{cld}\cdot f_{N_i}^{act}}{\tau}, \quad (15)$$

where $(M_{i,j})_{cld}$ is the mass concentration in the cloudy portion of the grid cell, calculated as described in Eq. (7), and $(N_i)_{cld}$ is the corresponding number concentration. $f_{M_{i,j}}^{act}$ and $f_{N_i}^{act}$ are the activated fraction for mass and number concentrations of aerosol. τ is the time scale of conversion of cloud water to rainwater, which can be computed from the autoconversion rate, accretion rate, and cloud liquid water content.

The removal of aerosols by falling precipitation is known as washout. Ice-phase (snow) and liquid-phase (rain) washout are treated separately using different scavenging efficiencies. The scavenging fraction is proportional to the precipitation flux and accounts for the volume fraction of precipitation falling through clear-sky areas. In PAMT, the washout process is parameterized as (Scott, 1978):

$$\left(\frac{\partial M_{i,j}}{\partial t}\right)_{\text{washo}} = -\zeta \cdot P_r \cdot E_{c_M} \cdot (M_{i,j})_{clr}, \left(\frac{\partial N_i}{\partial t}\right)_{\text{washo}} = -\zeta \cdot P_r \cdot E_{c_N} \cdot (N_i)_{clr} \quad (16)$$

where $(M_{i,j})_{clr}$ and $(N_i)_{cld}$ are the mass and number concentrations of clear-sky aerosols, P_r is the precipitation rate adjusted by clear-sky fraction and scavenging efficiency, and the constant ζ is set to 5.2 for rain and 3.7 for snow. E_{c_M} and E_{c_N} are the collection efficiencies for mass and number, which is approximated as an aerosol-size dependent approximation of the below-cloud scavenging parameterization for rain by Croft et al. (2009). A piecewise power-law formulation is applied between prescribed lower and upper cutoff radii, and unity efficiency is assumed outside this range. The bulk collection efficiencies for number and mass are then obtained by integrating this size-dependent efficiency over the aerosol size distribution, thereby accounting for hygroscopic growth and size-resolved scavenging in an implicit manner.

https://doi.org/10.5194/egusphere-2026-6615
Preprint. Discussion started: 10 November 2026
© Author(s) 2026. CC BY 4.0 License.

When falling precipitation partially or completely evaporates, aerosols may be re-released into the atmosphere, a process known as resuspension. In PAMT, resuspension is represented by releasing previously scavenged aerosols back to the clear-sky portion of the grid cell in proportion to the fraction of precipitation that evaporates (rain) or sublimates (snow) during its descent, while conserving mass by reducing the remaining precipitating flux accordingly. This process is parameterized as:

$$\left(\frac{\partial M_{i,j}}{\partial t}\right)_{\text{resus}} = \frac{F_{p_M_{i,j}} \cdot f_{evp}}{\Delta t}, \left(\frac{\partial N_i}{\partial t}\right)_{\text{resus}} = \frac{F_{p_N_i} \cdot f_{evp}}{\Delta t}, \quad (17)$$

where $F_{p_M_{i,j}}$ and $F_{p_N_i}$ are the fluxes of aerosol mass and number carried by precipitation, f_{evp} is the fraction of precipitation that evaporates (for rain) or sublimates (for snow), and Δt is the time step.

In MAM7, the treatment of aerosol wet deposition is generally similar. The parameterization is mainly based on (Barth et al., 2000; Rasch et al., 2000), and it is modified to be consistent with cloud macro- and microphysics. For rainout, cloud fraction, cloud water, and precipitation production profiles are used to calculate first-order cloud-water loss rates, which are then multiplied by solubility factors to determine aerosol loss rates. For washout, the first-order removal rate is given by [(solubility factor)×(scavenging coefficient)×(precipitation rate)], where the solubility factor serves as a tuning parameter. The scavenging coefficient is explicitly calculated and varies with particle size (Easter et al., 2004). Aerosols removed at one altitude can be resuspended at lower altitudes if precipitation evaporates. In MAM7, a fraction of cloud-scavenged aerosols is resuspended, equal to the fraction of precipitation that evaporates below the cloud.

2.2.13 Summary of PAMT

PAMT and MAM7 differ significantly in their representation of aerosol mixing state and size distribution. There are also differences in the parameterizations of aerosol source and sink processes between the two modules. A summary of the similarities and differences for all parameterizations is provided in Table 2.

2.3 Module coupling

Integrating the PAMT into CIESM requires a systematic restructuring of the aerosol-related physical processes originally implemented in CAM5.3 (Fig. 3). In the baseline configuration (i.e., CIESM-MAM7), the computation of aerosol processes is distributed across multiple components of the model. During the integration of PAMT, all parameterizations and process handlers associated with MAM7 are first disabled to avoid conflicts or double counting. Subsequently, the PAMT module is embedded and linked to the corresponding atmospheric physics routines. The key modifications required to achieve full two-way coupling between PAMT and CIESM are described below.

https://doi.org/10.5194/egusphere-2026-6615
Preprint. Discussion started: 10 November 2026
© Author(s) 2026. CC BY 4.0 License.

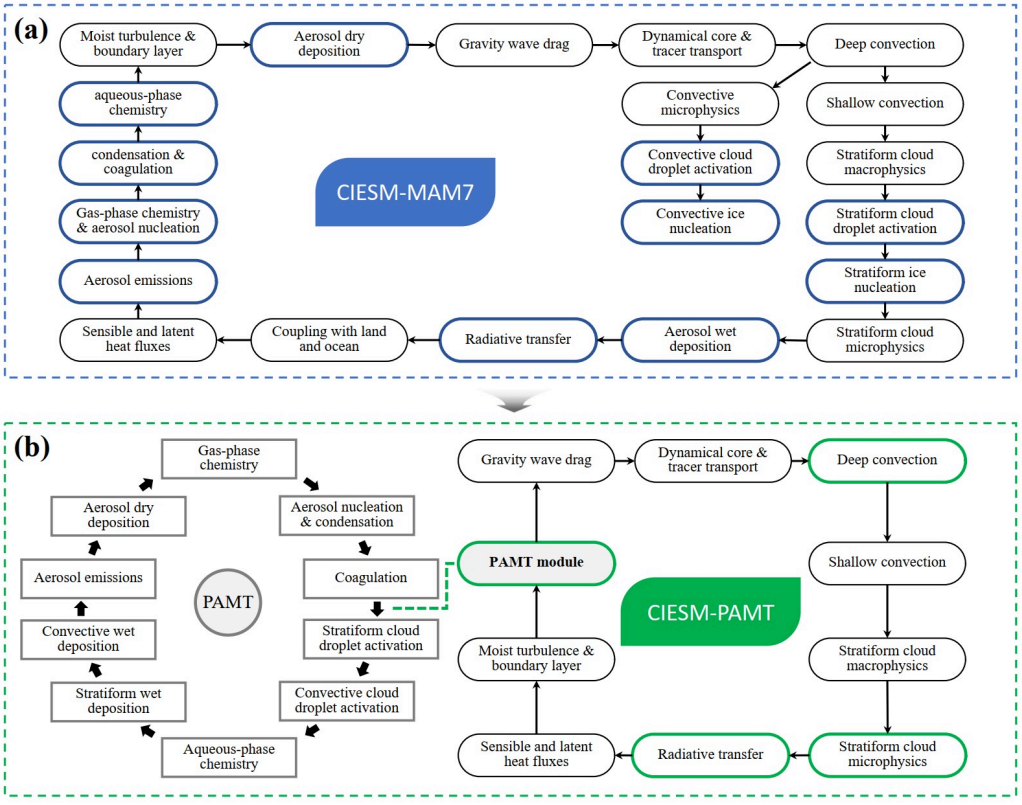


Figure 3. Schematic of online aerosol coupling in CIESM with PAMT and MAM7. Panel (a) shows the default coupling scheme CIESM-MAM7 (processes related to aerosols are marked in blue), and panel (b) shows the coupling scheme after integrating the new PAMT module (processes related to aerosols are marked in green).

2.3.1 Treatment of Tracers

In CIESM, the PAMT module introduces 29 additional tracers that can be transported across grid cells. Among them, 24 tracers represent aerosol number mixing ratios and component-specific mass mixing ratios within different sections, while the remaining 5 tracers represent concentrations of gases. These tracers are transported by the resolved three-dimensional wind field using the finite-volume dynamical core with a conservative flux-form semi-Lagrangian transport scheme (Lin and Rood, 1997, 1996). Subgrid-scale vertical redistribution of aerosols is represented through deep convection (ZM scheme) (Zhang and McFarlane, 1995), shallow convection (Park and Bretherton, 2009), and turbulent mixing based on a diagnostic turbulent kinetic energy (TKE) scheme (Bretherton and Park, 2009). In deep convective clouds, aerosols and trace gases are vertically transported within a grid column using updraft and downdraft mass fluxes from the ZM scheme (Neale et al., 2012). Consistent with the default CAM5.3 configuration, convective transport is currently treated separately from wet removal. Therefore, key quantities diagnosed by the ZM scheme, including cloud water, rain water, evaporation, detrainment rates, cloud fraction, and related variables, are passed to the aerosol module to compute convective wet deposition. Shallow convection transports aerosols in an analogous manner using mass fluxes diagnosed from the shallow convection

https://doi.org/10.5194/egusphere-2026-6615
Preprint. Discussion started: 10 November 2026
© Author(s) 2026. CC BY 4.0 License.

parameterization, while wet deposition is also handled within the aerosol module. Turbulent mixing is represented using a diagnostic TKE scheme, which parameterizes boundary-layer vertical diffusion of aerosols and provides a characteristic velocity scale used in stratiform cloud nucleation and aerosol resuspension processes. In addition, aerosol mass and number are modified by source and sink processes as described in Table 2.

2.3.2 Interface Construction

During each time step, the PAMT module requires a comprehensive set of input variables, which can be grouped into several categories. Atmospheric state variables include temperature, pressure, humidity, wind fields, and boundary layer height, which control aerosol thermodynamics and transport. Cloud and precipitation properties from both stratiform and convective parameterizations (e.g., cloud fraction, liquid water content, precipitation rates, and evaporation) are used to represent wet scavenging and in-cloud processes. Tracers of aerosol (number and mass mixing ratios in Table 1) and gas (e.g., SO_2, H_2O_2, DMS, H_2SO_4, and SOAG) are prognostic variables that are transported and undergo coupled physical and chemical processes within PAMT (Fig. 3b). In addition, prescribed oxidants (O_3, OH, NO_3, and HO_2) and background gases (e.g., CO_2) are provided from external forcing datasets and are used in in-cloud oxidation and proton molarity (pH) calculations, but are not modified by the PAMT module. Surface properties, including land–sea fraction, vegetation type, soil moisture, surface wind speed, and dust-related parameters, are used to constrain emissions, dry deposition, and natural aerosol sources.

These variables are passed from the atmospheric component of CIESM to PAMT through a dedicated interface, and subsequently processed within the module following the workflow illustrated in Fig. 3b. After these calculations, updated tracer mixing ratios are first computed within the PAMT module. Rather than directly overwriting the state variables in CIESM, PAMT diagnoses the corresponding tendencies as the difference between the updated and original tracer concentrations divided by the model time step. These tendencies are passed to the host model through the physics tendency structure and are then used to advance tracer concentrations within the time integration framework of the atmospheric model component. In addition, selected diagnostic quantities (e.g., column-integrated tendencies and aerosol-related variables) are archived for analysis but do not directly affect the model state.

2.3.3 Impacts on Clouds

The impacts of PAMT on clouds are primarily represented through its provision of cloud condensation nuclei (CCN) and ice-nucleating particles (INPs), which directly influence cloud droplet nucleation (Section 2.2.9) and ice nucleation (Section 2.2.10). In CIESM, stratiform cloud microphysics is treated using the Morrison and Gettelman (2008) (i.e., MG1.5), while convective microphysics is represented by a diagnostic scheme embedded in the ZM convection parameterization (Song and Zhang, 2011) (i.e., ZMm). Aerosol effects are not explicitly considered in the shallow convection scheme. Notably, ZMm was developed with reference to MG1.5, and therefore adopts consistent formulations for cloud droplet and ice nucleation.

For stratiform clouds, CCN concentrations are diagnosed within the PAMT module based on the large-scale cloud properties (e.g., cloud liquid water content, cloud fraction), thermodynamic conditions (e.g., water vapor, temperature), vertical

https://doi.org/10.5194/egusphere-2026-6615
Preprint. Discussion started: 10 November 2026
© Author(s) 2026. CC BY 4.0 License.

velocity, and environmental variables provided by the host atmospheric model. The resulting CCN number mixing ratio is stored in pointer variables and subsequently accessed by the MG1.5 microphysics scheme during droplet nucleation. Compared to CCN, the treatment of INPs is more straightforward: the number mixing ratios of sulfate and dust aerosols predicted by PAMT are directly passed to the stratiform microphysics scheme and used in heterogeneous ice nucleation. In convective clouds, CCN and INPs are treated in an analogous manner. However, the cloud properties used for CCN calculation correspond to convective clouds, and the updraft velocity is taken as the vertical velocity in cumulus updrafts diagnosed by the ZMm scheme (Song and Zhang, 2011).

It is important to note that, due to the modular design of PAMT, all aerosol processes are handled within a separate module. As a result, aerosol and cloud processes are not executed sequentially within the same microphysics routines, as is the case in MAM7, where CCN and INPs are computed and used directly within MG1.5 or ZMm (Fig. 3a), but are instead coupled through external interfaces (Fig. 3b). This structural separation may weaken the coupling between aerosol and cloud processes to some extent, and further analysis is needed in future work.

2.3.4 Impacts on the Radiation

To enable interactive aerosol-radiation coupling, PAMT calculates aerosol optical properties, including extinction coefficient, single-scattering albedo, and asymmetry factor, for each given spectral band (14 shortwave and 16 longwave bands) (Neale et al., 2012). These quantities are then passed to the CIESM radiative transfer module, named RRTMG (Iacono et al., 2008; Mlawer et al., 1997), to calculate atmospheric heating rates and radiative fluxes, thereby representing aerosol–radiation interactions within the model. However, existing CIESM interfaces were originally designed for MAM3/MAM7. Therefore, for each longwave and shortwave band in RRTMG, we generated an offline lookup table of aerosol optical parameters, taking into account the mixing states represented in PAMT (Fig. 1), using the following approach.

In the radiation calculations, five aerosol species are considered: SO4, BC, OA, DU, and SS, as shown in Fig. 1. Hygroscopic growth modifies aerosol size and effective refractive index, thereby altering aerosol optical properties and radiative fluxes. For hygroscopic components, the water uptake under subsaturated conditions is parameterized using the κ-hygroscopicity framework of Petters and Kreidenweis (2007), which relates aerosol chemical composition to equilibrium hygroscopic growth as a function of relative humidity. Aerosol optical properties are taken from Li et al. (2001, 2008) for SO4 and SS, Peng et al. (2012) for DU, d'Almeida (1991) for BC, and Peters et al. (2010) for OA.

A key feature of the aerosol radiation algorithm is the explicit treatment of internal mixing among SO4, BC, and OA. These components are assumed to coexist within the same particles, such that hygroscopic growth of the host material (e.g., SO4 or OA) modifies the effective optical environment of absorbing inclusions (BC). The optical properties of internally mixed aerosols are parameterized in a six-dimensional state space, defined by effective radius and effective variance (particle size), relative humidity (hygroscopic growth), and the fractional contributions of SO4, OA, and BC (composition, summing to unity). Each point in this parameter space represents a realizable state of the internally mixed aerosol, for which extinction coefficient, single-scattering albedo, and asymmetry factor are evaluated. Compared with external mixing, the internal-

https://doi.org/10.5194/egusphere-2026-6615
Preprint. Discussion started: 10 November 2026
© Author(s) 2026. CC BY 4.0 License.

mixing treatment enhances absorption through lensing effects and provides a physically consistent representation of composition-dependent aerosol radiation interactions.

In addition, the CCN and INP concentrations diagnosed by the aerosol module are passed to the stratiform and convective microphysics schemes to compute droplet and ice nucleation, representing aerosol–cloud interactions. Aerosol-induced radiative effects further modify large-scale circulation, which in turn alters aerosol sources and sinks, constituting a fully two-way coupled process.

2.3.5 Others

Several other adjustments were made to aerosol-related parameterizations when implementing PAMT in CIESM. We replaced the default COSP1.3 (the Cloud Feedback Model Intercomparison Project Observational Simulator Package, version 1.3) (Bodas-Salcedo et al., 2011) in CIESM with the COSP1.4 implementation of (Guo et al., 2020), incorporated the effect of pre-existing ice crystals on homogeneous freezing (Shi et al., 2015), and adjusted the prescribed minimum in-cloud cloud droplet number concentration from 0 to 30 cm^{-3} based on observational constraints (Jia and Quaas, 2023), consistent with the range of 20–40 cm^{-3} adopted by Neubauer et al. (2019).

3 Model Configuration and Experimental Setup

3.1 Forcing Data, Nudging, and Simulation Configuration

After successfully implementing the PAMT into CIESM, simulations using the same atmospheric general circulation model can be conducted to compare the outputs of the two different aerosol modules (PAMT and MAM7). To minimize the influence of internal variability and uncertainties associated with different forcing agents, both CIESM-MAM7 and CIESM-PAMT are driven with identical prescribed observational sea surface temperature (SST) and sea ice cover that include interannual variability (Eyring et al., 2016), as well as consistent emissions of SO4, BC, OA, and their precursors based on the CMIP6 emission inventory (see Section 2.2.3).

In addition, to further reduce the impact of natural variability on the simulations, this study applies Newtonian relaxation (nudging) to constrain horizontal wind fields in CIESM. The nudging reference data are taken from the latest global horizontal wind reanalysis dataset released by the European Centre for Medium-Range Weather Forecasts (ECMWF), namely ECMWF Reanalysis version 5 (ERA5) (Hersbach et al., 2020). The nudging technique adjusts the simulated winds in all model levels toward the observations-constrained fields of the reanalysis, ensuring that the model atmosphere remains close to reality (Kooperman et al., 2012). This approach helps ensure that differences between simulations primarily arise from differences in aerosol and their effects on clouds and radiation, rather than from discrepancies in meteorological conditions. A key parameter in nudging is the relaxation timescale, which determines how strongly the model is nudged toward observations, and a 6-hour timescale recommended by Kooperman et al. (2012) is adopted in this study.

https://doi.org/10.5194/egusphere-2026-6615
Preprint. Discussion started: 10 November 2026
© Author(s) 2026. CC BY 4.0 License.

For the simulations, CIESM is configured with a finite-volume grid of 1.9° × 2.5° for the atmosphere and land, and a displaced-pole ocean/sea-ice grid with a resolution of 1.125° × 0.27–0.54° (i.e., f19_g16). The vertical grid consists of 30 layers using the hybrid sigma-pressure grid. The model time step is 30 minutes. The simulations span 15 years (2000–2014), and observational datasets corresponding to this period are used for performance evaluation.

3.2 Model Tuning and Aerosol Diagnostics

Hourdin et al. (2017) pointed out that uncertainties associated with parameter tuning in model development constitute an important process that should be transparent. Therefore, prior to the simulations, a limited set of tunable parameters related to cloud fraction, convective transport, and cloud evaporation were adjusted following a transparent tuning strategy aimed at achieving a realistic global radiation balance and cloud climatology. The tuning was performed only for CIESM-MAM7, while CIESM-PAMT directly adopted the same parameter settings to ensure a consistent comparison between the two aerosol modules. Details of the tuning strategy and the final parameter values are provided in Appendix A.

To facilitate a comprehensive evaluation following the AeroCom phase III (AeroCom3) protocol (Gliß et al., 2021), several additional aerosol diagnostics were implemented in CIESM, including the aerosol surface emission flux (Tg $year^{-1}$), aerosol lifetime (days), aerosol burden (Tg), optical depth (OD, unitless), mass extinction coefficient (MEC, m^2 g^{-1}), Ångström exponent (AE, unitless), and fine-/coarse-mode aerosol optical depth (AOD_f and AOD_c, unitless). For variables not directly available from the model output, particularly AOD_f and AOD_c in PAMT, dedicated diagnostic procedures were developed based on aerosol optical properties and size distributions. A detailed description of the diagnostic framework is provided in Appendix B.

4 Datasets for Model Evaluation

The observational datasets used in this study can be categorized by their relative reliability into, in descending order, in-situ measurements (including ground-based and shipborne observations), satellite observations, reanalysis products, and multi-model results. Each category is introduced below.

4.1 In-situ Measurements

In-situ measurements are widely regarded as the most accurate means of observing aerosols and are commonly used to calibrate satellites and evaluate model performance. For aerosol studies, in-situ observations provide information on aerosol optical properties as well as mass and number concentrations of different species. However, most existing in-situ sites are located on land. To compensate for the lack of marine observations, this study also incorporates a set of shipborne measurements. The spatial distribution of all in-situ observation sites used in this study is shown in Fig. 4.

https://doi.org/10.5194/egusphere-2026-6615
Preprint. Discussion started: 10 November 2026
© Author(s) 2026. CC BY 4.0 License.

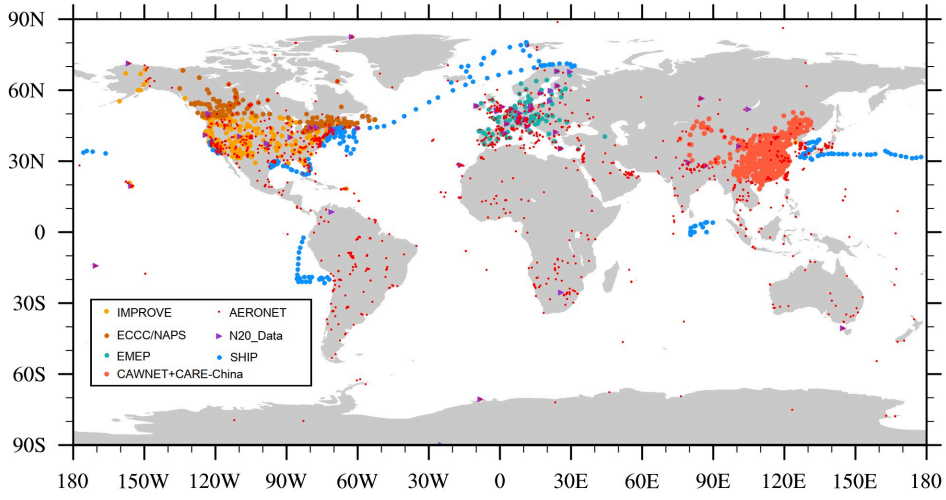


Figure 4. Spatial distribution of aerosol observation sites used in this study. Observation networks include the Aerosol Robotic Network (AERONET) (Holben et al., 1998), the Interagency Monitoring of PROtected Visual Environments (IMPROVE) (Hyslop and White, 2008), the Environment and Climate Change Canada/National Air Pollution Surveillance (ECCC/NAPS) (Bari and Kindzierski, 2018), the European Monitoring and Evaluation Programme (EMEP) (Tørseth et al., 2012), the multiple international research cruises since 1991 (SHIP), the China Atmosphere Watch Network (CAWNET) (Zhang et al., 2012), and the Campaign on Atmospheric Aerosol Research network of China (CARE-China) (Xin et al., 2015).

The Aerosol Robotic Network (AERONET) is a global ground-based remote sensing network built on sun photometers (Holben et al., 1998) and is widely regarded as the most reliable method for long-term aerosol optical property measurements. AERONET includes more than 500 long-term monitoring sites worldwide (Fig. 4) and has provided aerosol optical observations since 1992. To ensure consistency with previous multi-model evaluations, this study uses the dataset use by Gliß et al. (2021) to evaluate simulated aerosol optical properties. Specifically, AOD and AE were obtained from the AERONET Version 3 (Level 2) sun photometer products, while AOD_f and AOD_c, were derived from the Level 2 spectral deconvolution algorithm (SDA) products. Cloud-screened and quality-assured daily observations were used directly without additional quality control. Only sites below 1000 m altitude were retained, while data from short-term DRAGON campaigns were excluded to avoid regional overrepresentation (Holben et al., 2018). To match the model output at 550 nm, AOD, AOD_f, and AOD_c reported at 500 nm were converted to 550 nm using AE. Monthly means were calculated from daily observations for comparison with model simulations. For in situ hourly data, daily means were first computed using at least six valid hourly observations, followed by monthly averaging requiring at least seven valid daily values, and months not meeting these coverage criteria were excluded. It should be noted that SDA-derived AOD_f and AOD_c are based on optical partitioning rather than a strict particle size threshold and may therefore differ from the model-defined fine and coarse modes.

To evaluate aerosol mass concentrations over land, this study collects several ground-based observations (Fig. 4). These datasets include the Interagency Monitoring of PROtected Visual Environments (IMPROVE) in the United States (Hyslop and White, 2008), the Environment and Climate Change Canada / National Air Pollution Surveillance (ECCC/NAPS) in Canada (Bari and Kindzierski, 2018), the European Monitoring and Evaluation Programme (EMEP) in Europe (Tørseth et al.,

https://doi.org/10.5194/egusphere-2026-6615
Preprint. Discussion started: 10 November 2026
© Author(s) 2026. CC BY 4.0 License.

2012), as well as the China Atmosphere Watch Network (CAWNET) (Zhang et al., 2012) and the Campaign on Atmospheric Aerosol Research network of China (CARE-China) (Xin et al., 2015) in China. These networks provide mass concentrations of different aerosol species and size fractions, including BC, OA, and SO4, as well as particles with dry diameters smaller than 2.5 μm (PM2.5) and 10 μm (PM10). IMPROVE includes approximately 200 sites across the United States and provides data since 2000. EMEP comprises around 110 sites in Europe with data availability also starting from 2000. CAWNET and CARE-China include more than 100 sites in China, offering measurements since 2006, with most sites located in eastern China (Fig. 4). ECCC/NAPS provides surface observations across Canada dating back to 2005, with measurements primarily focused on PM2.5 and PM10 mass concentrations, while the availability of species-resolved aerosol mass concentrations is relatively limited.

To evaluate the performance of CIESM in simulating aerosols over the ocean, this study compiles shipborne observations from various regions worldwide. The Pacific Marine Environmental Laboratory of the National Oceanic and Atmospheric Administration (NOAA PMEL) has conducted multiple international research cruises since 1991 (referred to as SHIP) (Meinig et al., 2019). For this study, we selected cruises from 2000–2014 that include near-surface SO4 mass concentration measurements to evaluate the model's SO4 simulations over ocean (Fig. 4). These cruises include ACEASIA, CALNEX, DYNAMO, ICEALOT, NEAQS2002, NEAQS2004, TEXAQS2006, VOCALS, WACS, and WACS2. ACEASIA provides aerosol over the East China Sea, the Sea of Japan, and the central Pacific; DYNAMO covers the Indian Ocean; ICEALOT samples near-polar marine aerosols; NEAQS2002, NEAQS2004, TEXAQS, WACS, and WACS2 capture aerosols around the coastal regions of North American; and VOCALS provides aerosol data off the west coast of South America.

Previous studies have shown that aerosol number concentrations exhibit greater model uncertainties than mass concentrations (Mann et al., 2014). Therefore, this study incorporates some number-concentration datasets to evaluate CIESM. N20 represents the aerosol number concentration for particles with diameter larger than 20 nm and can be measured using aerosol spectrometers. The N20 observational dataset (N20_Data) used here includes observations from three Canadian stations (Whistler, Alert, and Egbert) (D'Andrea et al., 2013), one U.S. Southern Great Plains site (ARM SGP) (McComiskey and Ferrare, 2016), several European sites (LEEDS) (Mann et al., 2014), and 14 global sites from the Global Atmosphere Watch network (GAW) network (Asmi et al., 2013).

4.2 Satellite Observations

Given the limited spatial coverage of in situ observations, satellite observations are further used to evaluate the model's performance in simulating aerosol optical properties at the global scale.

Commonly used satellite instruments for observing aerosol optical properties include the Moderate Resolution Imaging Spectroradiometer (MODIS) and the Advanced Along Track Scanning Radiometer (AATSR). MODIS is carried on NASA's satellites Terra (launched in 1999) and Aqua (launched in 2002) (Platnick et al., 2003). MODIS provides global AOD retrievals. Using AERONET for evaluation, Wei et al. (2019) showed that MODIS performs well with the AERONET-based AOD values on different spatial scales among satellites. However, MODIS still overestimates AOD compared with

https://doi.org/10.5194/egusphere-2026-6615
Preprint. Discussion started: 10 November 2026
© Author(s) 2026. CC BY 4.0 License.

AERONET, with MODIS-Aqua and MODIS-Terra showing biases of +9% and +17%, respectively (Gliß et al., 2021). AATSR, one of the nine instruments aboard the European Space Agency (ESA)'s Envisat satellite, operated from 2002 to 2012. AATSR retrievals provide optical parameters including AOD, AOD_f, AOD_c, and AE. In this study, we use the Swansea University product (AATSR-SU) (Bevan et al., 2012). It should be noted that compared with AERONET, AATSR-SU also shows biases of +1.6%, –14.7%, and +14.3% for AOD_f, AOD_c, and AE, respectively (Gliß et al., 2021).

4.3 Reanalysis Datasets

Reanalysis products provide comprehensive datasets by assimilating a wide range of atmospheric, land, and ocean observations into numerical models, yielding long-term, high-accuracy datasets that are physically consistent with observations. To further evaluate the optical depth (OD) and burden ($Burden$) of different aerosol species (BC, OA, SO4, DU, and SS), this study uses two reanalysis datasets, including the Modern-Era Retrospective Analysis for Research and Applications, Version 2 (MERRA-2) (Gelaro et al., 2017) and the Monitoring Atmospheric Composition and Climate (MACC) (Inness et al., 2013). Both MERRA-2 and MACC provide aerosol optical depth for individual species, while MERRA-2 additionally offers burden information for each aerosol component. Both MACC and MERRA-2 assimilate satellite observations of AOD, primarily MODIS retrievals, providing observation-constrained estimates of aerosol loading for model evaluation.

4.4 Multi-model Data from AeroCom3

This section introduces a comprehensive dataset that integrates the strengths of multiple observational products and has undergone rigorous quality control, making it highly suitable for model evaluation.

Since 2002, the Aerosol Comparisons between Observations and Models initiative (AeroCom) has coordinated multi-model aerosol simulations from modeling groups worldwide. Its aim is to provide up-to-date understanding of aerosol forcing uncertainties and best estimates. The most recent project with relatively comprehensive results is its third phase (AeroCom3). Multi-model results are generally considered more robust than single-model simulations and tend to exhibit greater consistency with observations. Gliß et al. (2021) evaluated aerosol optical properties and aerosol life-cycle metrics from 14 global climate models participating in AeroCom3, showing that current models systematically underestimate aerosol optical parameters, leading to an overall ~15% low bias in modeled aerosol radiative forcing. Given its extensive use of observational datasets and multi-model simulations, AeroCom3 provides an excellent reference for evaluating CIESM's aerosol optical properties. Therefore, this study performs CIESM simulations using the same experimental setup and compares the results against AeroCom3 datasets. The evaluation uses AERONET observations, satellite products (AATSR-SU and the merged dataset MERGED-FMI), and multi-model results (AeroCom_Mean). The variables involved include AOD, AOD_f, AOD_c, and AE, as well as OD, MEC, surface emission flux, lifetime, and burden for individual aerosol components. All datasets correspond to the year 2010.

https://doi.org/10.5194/egusphere-2026-6615
Preprint. Discussion started: 10 November 2026
© Author(s) 2026. CC BY 4.0 License.

4.5 Summary of Aerosol Datasets

The datasets used in this study to evaluate the aerosol simulations in CIESM include ground-based and shipborne observations, satellite products, reanalysis datasets, and multi-model ensemble results. The variables cover aerosol optical properties, number concentrations, and mass concentrations, with spatial sampling ranging from surface sites to the vertical column, and from regional to global scales. The temporal coverage spans 2000–2014, consistent with the CIESM simulation period. A summary of all datasets is provided in Table 5.

Table 5. Overview of aerosol datasets used for model evaluation in this study.

Type	Dataset	Variable	Region	Time period	Reference
Site	AERONET (from AeroCom3)	AOD, AOD_f, AOD_c, and AE	Global	2010	(Gliß et al., 2021; Holben et al., 1998)
	IMPROVE	Mass concentration of BC, OA, SO4, PM2.5, and PM10	United States	2000 - 2014	(Hyslop and White, 2008)
	EMEP		Europe	2000 - 2014	(Tørseth et al., 2012)
	ECCC/NAPS		Canada	2005 - 2014	(Bari and Kindzierski, 2018)
	CAWNET, CARE-China		China	2006 - 2014	(Xin et al., 2015; Zhang et al., 2012)
	SHIP	Mass concentration of SO4	Ocean	2000 - 2014	(Meinig et al., 2019)
	N20_Data	$N20$ (Aerosol number concentration with a particle size larger than 20 nm)	Global	2000 - 2014	(D'Andrea et al., 2013)
Satellite	MERGED-FMI (AeroCom3)	AOD	Global	2010	(Gliß et al., 2021; Sogacheva et al., 2020)
	AATSR-SU (AeroCom3)	AOD_f, AOD_c, and AE	Global	2010	(Bevan et al., 2012; Gliß et al., 2021)
Reanalysis	MERRA-2	Optical depths and burdens of BC, OA, SO4, DU, and SS	Global	2000 - 2014	(Gelaro et al., 2017)
	MACC	Optical depths of BC, OA, SO4, DU, and SS	Global	2003 - 2012	(Inness et al., 2013)
Model	AeroCom_Mean	AOD, AOD_f, AOD_c, and AE from 14 models, along with the optical depth, burden, mass extinction coefficient, surface emission flux, and lifetime of different aerosol components	Global	2010	(Gliß et al., 2021)

5 Results

This section presents the aerosol simulations from CIESM-MAM7 and CIESM-PAMT, including aerosol optical properties, mass concentrations, and number concentrations. The evaluation of aerosol optical properties mainly follows the framework of the AeroCom3 (Gliß et al., 2021). In the evaluation, the reliability of datasets is considered to decrease in the following order: ground-based/shipborne observations, satellite observations, reanalysis datasets, and multi-model results.

https://doi.org/10.5194/egusphere-2026-6615
Preprint. Discussion started: 10 November 2026
© Author(s) 2026. CC BY 4.0 License.

5.1 CIESM performance compared to reference datasets

5.1.1 Spatial distributions of aerosol optical properties

First, we evaluate the spatial distributions of AOD, AOD_f, AOD_c, and AE simulated by CIESM under different aerosol modules. Figure 5 shows the global distributions of aerosol optical metrics from CIESM-PAMT/MAM7, AeroCom3, satellite products, and AERONET observations. To ensure comparability of the global means, model results have been masked to exclude regions without satellite coverage.

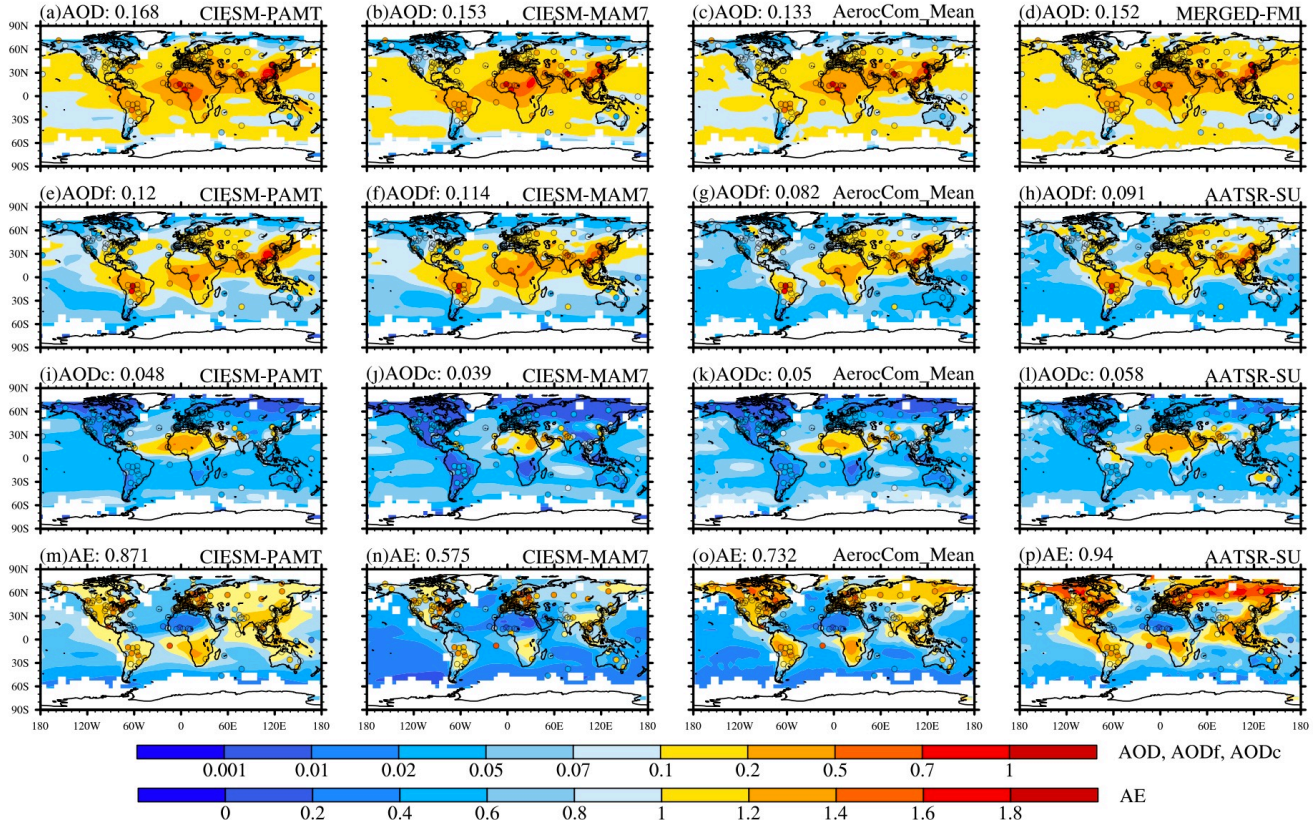


Figure 5. Simulated aerosol optical properties from CIESM. Columns 1 and 2 show CIESM-PAMT and CIESM-MAM7 results, respectively; column 3 shows the AeroCom3 multi-model mean (AeroCom_Mean), and column 4 shows satellite observations. Rows 1–4 (top to bottom) represent ***AOD***, fine-mode ***AOD*** (***AOD***$_f$), coarse-mode ***AOD*** (***AOD***$_c$), and Ångström exponent (***AE***). Colored circles refer to AERONET observations. Only 2010 data are used.

Overall, both CIESM-PAMT and CIESM-MAM7 reproduce the broad spatial patterns of aerosol optical properties reasonably well, and their global means are close to AeroCom3 and satellite estimates. Compared with CIESM-MAM7 (0.153, 0.114, 0.039, and 0.575), CIESM-PAMT yields higher AOD, AOD_f, AOD_c, and AE overall (0.168, 0.120, 0.048, and 0.871). These values of AOD and AOD_f simulated by CIESM are generally larger than the AeroCom3 ensemble mean (AeroCom_Mean, 0.133 and 0.082) and satellite retrievals (0.152 and 0.091). In contrast, the simulated AOD_c is consistently

https://doi.org/10.5194/egusphere-2026-6615
Preprint. Discussion started: 10 November 2026
© Author(s) 2026. CC BY 4.0 License.

lower than both the AeroCom_Mean (0.050) and satellite retrievals (0.058). The AE simulated by CIESM-PAMT is higher than the AeroCom_Mean (0.732) but lower than the satellite retrieval (0.940), whereas CIESM-MAM7 underestimates AE relative to both AeroCom_Mean and satellite observation.

Specifically, the observed maxima in AOD are well reproduced in the simulations with MAM7 and PAMT (Figs. 5a-d). High values of AOD are concentrated in anthropogenic source regions such as East Asia and India, and in natural aerosol source regions such as central–western Africa and northern–central South America (dust and biogenic organics). Notably, CIESM-PAMT matches satellite observations better over northern Africa and does not produce the spurious high-AOD region in northeastern Africa that is seen in CIESM-MAM7.

High AOD_f values are mainly distributed over industrialized and densely populated regions, including East Asia, India, Europe, and the eastern coast of North America, as well as regions strongly affected by biogenic and biomass-burning emissions, such as central Africa and central South America, where OA and BC are the dominant aerosol species (Figs. 5e–h). High AOD_f is also evident in coastal areas. Overall, CIESM reproduces the spatial distribution and major hotspots of elevated AOD_f reasonably well. Nevertheless, compared with satellite retrievals, CIESM underestimates AOD_f at high latitudes (e.g., > 60°N), a bias commonly found in current-generation climate models (Fig. 5g). Conversely, AOD_f is generally overestimated over remote open-ocean regions.

Both CIESM-PAMT and CIESM-MAM7 underestimate AOD_c relative to AeroCom3 and satellite products (Figs. 5i–l). Over land, high AOD_c values are primarily concentrated in major dust source regions, including northern Africa, the Arabian Peninsula, central Australia, and parts of East Asia such as the Gobi Desert. Both CIESM configurations successfully capture these major dust-related AOD_c maxima, with CIESM-PAMT showing closer agreement with satellite observations over northern Africa (Fig. 5i). In addition, satellite and AERONET observations indicate systematically higher AOD_c over South America and Siberia compared to AeroCom3 estimates. CIESM-PAMT reproduces these enhanced AOD_c signals well (Fig. 5i), whereas CIESM-MAM7 substantially underestimates AOD_c across these regions (Fig. 5j). Over the oceans, satellite observations reveal elevated AOD_c over regions influenced by dust transport, such as the tropical North Atlantic and the Arabian Sea, as well as over the North Atlantic and Southern Ocean. These large-scale spatial patterns are generally well represented by CIESM-PAMT, demonstrating improved performance relative to CIESM-MAM7 (Figs. 5i-j).

AE is a key metric characterizing aerosol extinction and is closely related to aerosol composition and mixing state. It is often interpreted as an effective indicator of particle size because AE generally decreases with increasing particle size (i.e., small AE typically corresponds to larger particles). However, when particle sizes exceed the visible wavelength, the AE–size relationship can be substantially distorted, particularly for multi-component aerosols, so AE differences in the visible band cannot be attributed solely to particle size differences (Schuster et al., 2006). As shown in Figs. 5m–p, CIESM-PAMT yields higher AE than CIESM-MAM7, which is more consistent with satellite-derived AE. The higher AE may reflect a generally smaller particle size in CIESM-PAMT, which is consistent with its higher AOD_f (Fig. 5e-f). It may also arise from differences in the representation of mixing state or from differences in the AE calculation method (Eq. (S1) in Appendix B).

https://doi.org/10.5194/egusphere-2026-6615
Preprint. Discussion started: 10 November 2026
© Author(s) 2026. CC BY 4.0 License.

These possibilities warrant further investigation. Also, close inspection of Fig. 5p shows that satellite-derived AE at high latitudes is higher than AERONET, suggesting that satellite retrievals may have a positive bias in polar regions.

5.1.2 Regional evaluation against AERONET observations

To evaluate the performance of CIESM across different regions and to identify where the main simulation biases occur, this study follows the AeroCom3 framework and presents scatter comparisons between model-simulated AOD, AOD_f, AOD_c, and AE and AERONET observations over nine major global regions (Fig. 6 and Table 6).

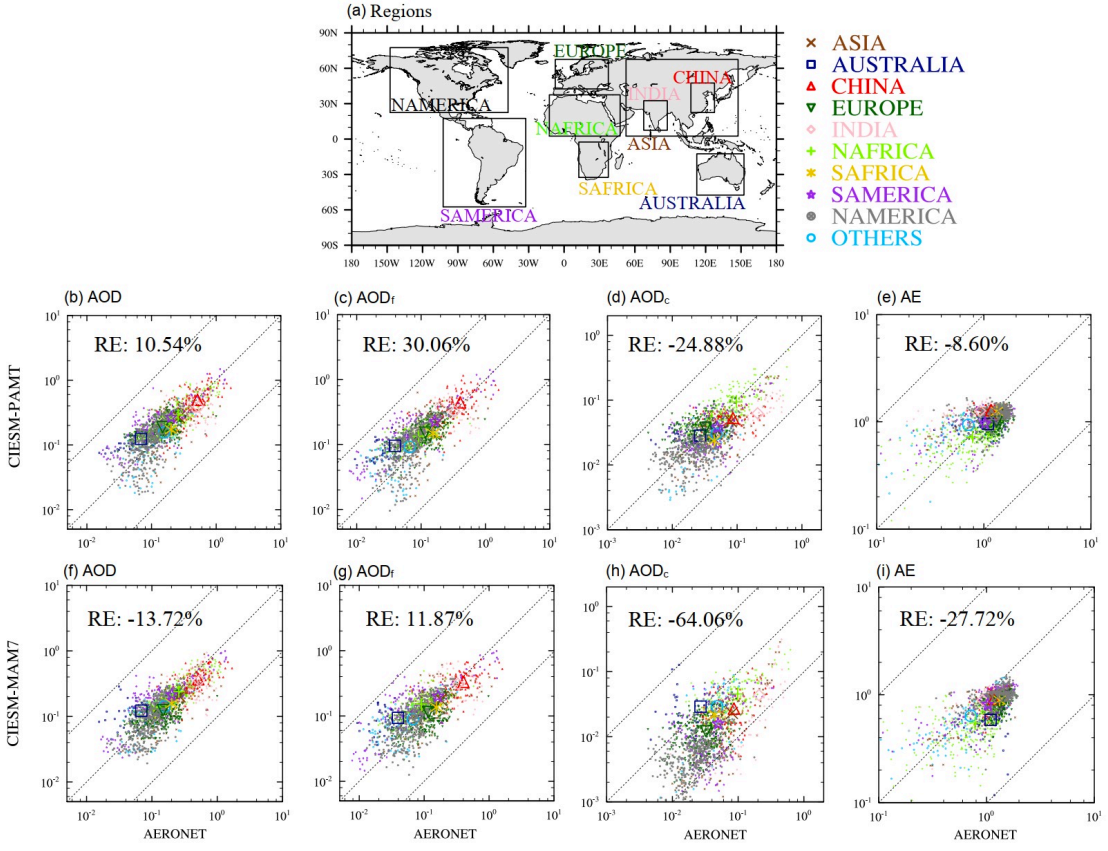


Figure 6. Scatter plots comparing CIESM-simulated aerosol optical properties with monthly AERONET observations for 2010. The variables include $\boldsymbol{AOD}$, $\boldsymbol{AOD_f}$, $\boldsymbol{AOD_c}$, and $\boldsymbol{AE}$. Different colors denote the nine AeroCom3 regions. Small markers represent individual monthly mean values, whereas large markers indicate regional mean values averaged over all collocated data within each region. The global mean relative error (RE) is reported in the upper-right corner of each panel.

To ensure data representativeness, the AERONET observations were subject to strict sampling requirements (Section 4.1), including at least six valid hourly observations per day and at least seven valid daily observations per month. Months that did not satisfy these coverage criteria were excluded. As a result, the available AERONET records do not necessarily provide complete monthly coverage throughout the year for every station. Because Fig. 5 is intended to illustrate the large-scale spatial distribution of aerosol optical properties, these sampling constraints were not explicitly considered, and annual means

https://doi.org/10.5194/egusphere-2026-6615
Preprint. Discussion started: 10 November 2026
© Author(s) 2026. CC BY 4.0 License.

were calculated directly from the available monthly observations. In contrast, the station-scale evaluation presented in this section applies a more rigorous collocation procedure. Monthly mean model outputs were matched to the corresponding months with valid AERONET observations and bilinearly interpolated to the station locations. The resulting station-based comparisons are presented in Fig. 6 and Table 6.

Table 6. Relative errors (RE, %) of CIESM-PAMT and CIESM-MAM7 relative to AERONET observations. Light green shading highlights the better-performing model. No shading is applied when both models have absolute relative errors below 5%, indicating comparable performance.

Region	CIESM-PAMT				CIESM-MAM7			
	AOD	AOD_f	AOD_c	AE	AOD	AOD_f	AOD_c	AE
ASIA	0.7	20.1	-41.4	-2.7	-23.8	-1.6	-71.2	-25.5
AUSTRALIA	80.0	141.0	6.0	-12.3	78.3	136.3	8.5	-46.5
CHINA	-3.2	10.5	-38.8	10.1	-28.4	-17.8	-68.7	-21.2
EUROPE	26.6	30.7	14.9	-23.8	-16.1	-1.6	-62.8	-34.7
INDIA	-26.5	-2.3	-69.8	37.1	-33.6	-6.2	-79.0	-3.3
NAFRICA	12.7	47.3	-4.1	-7.9	-7.3	67.0	-53.6	-29.9
SAFRICA	-14.1	-3.5	-46.2	-5.7	-21.4	-11.8	-50.4	-32.8
SAMERICA	34.8	40.9	-21.7	-4.5	9.3	24.1	-67.6	-19.8
NAMERICA	24.8	47.6	-32.5	-7.8	0.5	29.3	-74.0	-24.8
OTHERS	-0.2	37.5	-37.5	30.9	-8.7	34.2	-38.9	-10.9
ALL	10.5	30.1	-24.9	-8.6	-13.7	11.9	-64.1	-27.7

Different colors indicate different regions (Fig. 6a), and the global mean relative error (RE) is shown in the lower-right corner of each panel (Figs. 6b-i). Overall, CIESM coupled with the PAMT shows significant improvements in AOD, AOD_c, and AE compared with CIESM-MAM7, reflected by smaller biases. Compared with CIESM-MAM7, CIESM-PAMT shows substantial improvement in global RE: from −13.7% to 10.5% for AOD, −64.1% to -24.9% for AOD_c, and −27.7% to −8.6% for AE. Although CIESM-PAMT and CIESM-MAM7 produce similar global mean AOD_f values (0.120 vs. 0.114; Figs. 5e–f), the RE of PAMT at grid cells collocated with AERONET observations is substantially larger than that of MAM7 (30.1% vs. 11.9%; Figs. 6c, g). Since AERONET sites are predominantly located over continental regions, this discrepancy indirectly suggests that CIESM-PAMT exhibits larger biases in simulating AOD_f over land.

More specifically, CIESM-PAMT overestimates AOD mainly in Australia, Europe, North Africa and Americas, and underestimates it mainly in India and South Africa (|RE| > 10%). The overestimation of AOD over Australia, North Africa and Americas is primarily associated with an overestimation of AOD_f (Table 6). The overestimation of AOD in Europe is associated with both AOD_f and AOD_c (Fig. 6c, d, Table 6). The AOD underestimation in India and South Africa is mainly due to underestimated AOD_c. Correspondingly, regions with AOD_f overestimation generally exhibit low AE, and vice versa (Fig. 6e). In contrast to CIESM-PAMT, CIESM-MAM7 shows varying degrees of AOD underestimation in most regions

https://doi.org/10.5194/egusphere-2026-6615
Preprint. Discussion started: 10 November 2026
© Author(s) 2026. CC BY 4.0 License.

except Australia, and the biases are mainly linked to AOD_f (Fig. 6f, g). In fact, satellite observations and AERONET site measurements differ noticeably over Australia (Fig. 5d, h, l, p). Satellites detect higher AOD, AOD_f, and AOD_c over the central Australian dust source region, while AERONET values remain low, likely because the stations are mostly located along the desert margins.

5.1.3 Zonal distributions of aerosol optical properties

To further evaluate the large-scale characteristics of the simulations, we next analyze the zonal distributions of aerosol optical properties. Figure 7 shows the zonal AOD, AOD_f, AOD_c, and AE from CIESM compared with satellite and AERONET observations.

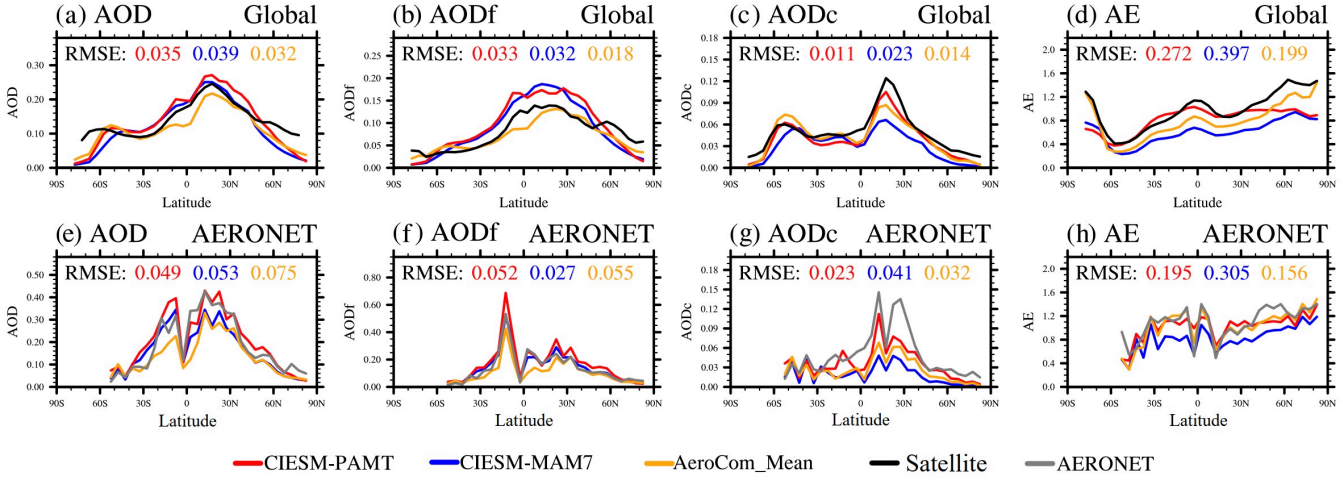


Figure 7. Zonal mean distributions of AOD, AOD_f, AOD_c, and AE from models and observations. AeroCom_Mean represents the monthly AeroCom3 multi-model mean. Four columns correspond to different variables. The first row shows comparisons with satellite observations, while the second row shows comparisons at grid cells collocated with AERONET sites. The root-mean-square error (RMSE) between the CIESM simulations and the corresponding observations is indicated at the top of each panel.

Following the AeroCom3 protocol, monthly mean AERONET observations and CIESM simulations were regridded to a common 5° × 5° grid and matched in space and time prior to the zonal averaging. Note that AOD, AOD_f, AOD_c, and AE are derived from different AERONET products and therefore do not necessarily share the same temporal coverage. For example, the highest AOD_f values near 15° S, which even exceed the corresponding AOD values, are primarily associated with Amazonian sites (e.g., Ji_Parana_SE) where valid AOD_f retrievals are available only during August–October, whereas AOD observations span a much longer period. However, because simulations are collocated with AERONET observations on a monthly basis, the evaluation is largely unaffected by differences in temporal sampling among the observational datasets.

As shown in Fig. 7, CIESM is able to reasonably reproduce the latitudinal variation patterns of aerosol optical properties. Overall, AeroCom_Mean generally underestimates these variables relative to observations, a bias that is substantially reduced in CIESM simulations, particularly for coarse-mode aerosol particles. Consistent with the previous analysis, CIESM

https://doi.org/10.5194/egusphere-2026-6615
Preprint. Discussion started: 10 November 2026
© Author(s) 2026. CC BY 4.0 License.

exhibits larger biases relative to satellite observations than AeroCom_Mean. However, it shows better overall agreement with AERONET observations, especially for AOD, AOD_f, and AOD_c. Compared with CIESM-MAM7, CIESM-PAMT produces higher values of AOD, AOD_c, and AE, which are in better agreement with AERONET observations, particularly for AOD_c and AE (Figs. 7g, h). In contrast, although PAMT and MAM7 yield similar global mean AOD_c (Figs. 5e, f), noticeable discrepancies remain when compared with AERONET observations (Fig. 7f); nevertheless, the bias is still smaller than that in AeroCom_Mean, as indicated by the RMSE values.

To clarify the current stage of CIESM's development, this study presents the global annual averages (2010) of surface emissions, lifetimes, burdens, optical depths, and mass extinction coefficients for different aerosol components simulated by CIESM-PAMT, CIESM-MAM7, and AeroCom3 (median and range), as shown in Table 7. Overall, most of the results from both CIESM-PAMT and CIESM-MAM7 fall within the AeroCom3 range, indicating that the overall performance of CIESM is broadly consistent with current mainstream models and is reasonable. Specifically, CIESM-PAMT generally produces higher values for aerosol optical properties than CIESM-MAM7, particularly for OA and SO4.

Table 7. Comparison of CIESM simulations with the multi-model median (and range). Values in red indicate that CIESM results fall outside the multi-model range (minimum to maximum).

Variable		CIESM-PAMT	CIESM-MAM7	AeroCom3
Surface emission [Tg year^{-1}]	BC	9.4	9.4	9.7 (8.4 - 9.8)
	DU	965	1703	1440 (848 - 5650)
	POA	46.2	46.2	74.6 (62.0 - 81.5)
	OA	151.6	151.2	116.0 (48.0 - 246.0)
	SO4	132.7	163.2	143.0 (94.3 - 240.0)
	SS	1845	5269	4980 (2030 - 50000)
Lifetime [day]	BC	6.3	6.9	5.5 (2.9 - 9.6)
	DU	5.6	3.3	3.7 (1.4 - 7.0)
	OA	5.8	7.4	6.0 (3.4 - 9.3)
	SO4	4.7	5.6	4.9 (1.8 - 7.0)
	SS	1.57	0.54	0.56 (0.19 - 3.13)
Burden [Tg]	BC	0.159	0.176	0.131 (0.068 - 0.260)
	DU	14.8	15.1	16.6 (5.7 - 22.3)
	OA	2.34	2.99	1.91 (0.79 - 2.99)
	SO4	1.7	2.5	1.8 (0.66 - 2.95)
	SS	7.9	7.7	8.7 (2.5 - 26.4)
Optical depth	BC	0.002	0.006	0.002 (0.001 - 0.004)
	DU	0.014	0.024	0.021 (0.011 - 0.031)
	OA	0.048	0.038	0.022 (0.009 - 0.041)
	SO4	0.054	0.030	0.035 (0.010 - 0.047)
	SS	0.040	0.046	0.044 (0.013 - 0.078)
	AOD	0.159	0.145	0.128 (0.097 - 0.148)

https://doi.org/10.5194/egusphere-2026-6615
Preprint. Discussion started: 10 November 2026
© Author(s) 2026. CC BY 4.0 License.

Mass extinction coefficient [$mg^2\ g^{-1}$]	BC	10.0	18.7	10.3 (3.7 - 13.7)
	DU	0.85	1.24	0.74 (0.39 - 1.68)
	OA	10.9	12.1	6.1 (4.3 - 13.3)
	SO4	16.0	5.8	8.5 (3.8 - 17.2)
	SS	2.67	2.79	2.84 (0.93 - 4.11)

From the evaluation of CIESM against AeroCom3, the following conclusions can be drawn: 1) The results from CIESM-PAMT and CIESM-MAM7 mostly lie within the uncertainty range of AeroCom3, indicating that CIESM's current performance is consistent with mainstream models and is reasonable. 2) Compared with CIESM-MAM7, CIESM-PAMT shows clear improvements in simulating AOD, AOD_c, and AE. Although its simulated values are generally higher than those from AeroCom3 and satellite observations, they show better agreement with AERONET measurements. In particular, the AE simulated by CIESM-PAMT is substantially closer to both satellite and AERONET observations than that simulated by CIESM-MAM7. Given that AE is highly sensitive to aerosol size distributions, this improvement provides independent support for the conclusion of von Salzen (2006) that the PLA represents aerosol size distributions more realistically than the conventional modal approach.

5.2 Aerosol Types in CIESM

Since satellite and AERONET observation mainly provide total aerosol optical depth and not component-specific values, this study uses reanalysis datasets MERRA-2 and MACC as additional references for comparing the optical depth (OD) and column mass ($Burden$) of different aerosol components (BC, DU, OA, SS, and SO4), as shown in Fig. 8. MERRA-2 provides both OD and $Burden$, while MACC only provides OD.

Compared with CIESM-PAMT, CIESM-MAM7 simulates significantly higher BC optical depth, which falls outside the uncertainty range of AeroCom3 but is closer to MERRA-2 values (Fig. 8a). This discrepancy is likely related to the optical calculation of BC in CIESM-MAM7, as its MEC for BC is notably higher than the multi-model results (Table 7). Assessment of BC optical depth remains highly uncertain, as substantial differences exist among the reanalysis products (Fig. 8a). Consequently, comparisons with these products alone are insufficient to determine which simulation better represents BC optical properties, highlighting the need for additional observational constraints such as absorption aerosol optical depth measurements. For BC burden, both CIESM-PAMT and CIESM-MAM7 produce similar results that fall within the AeroCom3 uncertainty but are noticeably lower than MERRA-2, especially at mid-to-high latitudes.

https://doi.org/10.5194/egusphere-2026-6615
Preprint. Discussion started: 10 November 2026
© Author(s) 2026. CC BY 4.0 License.

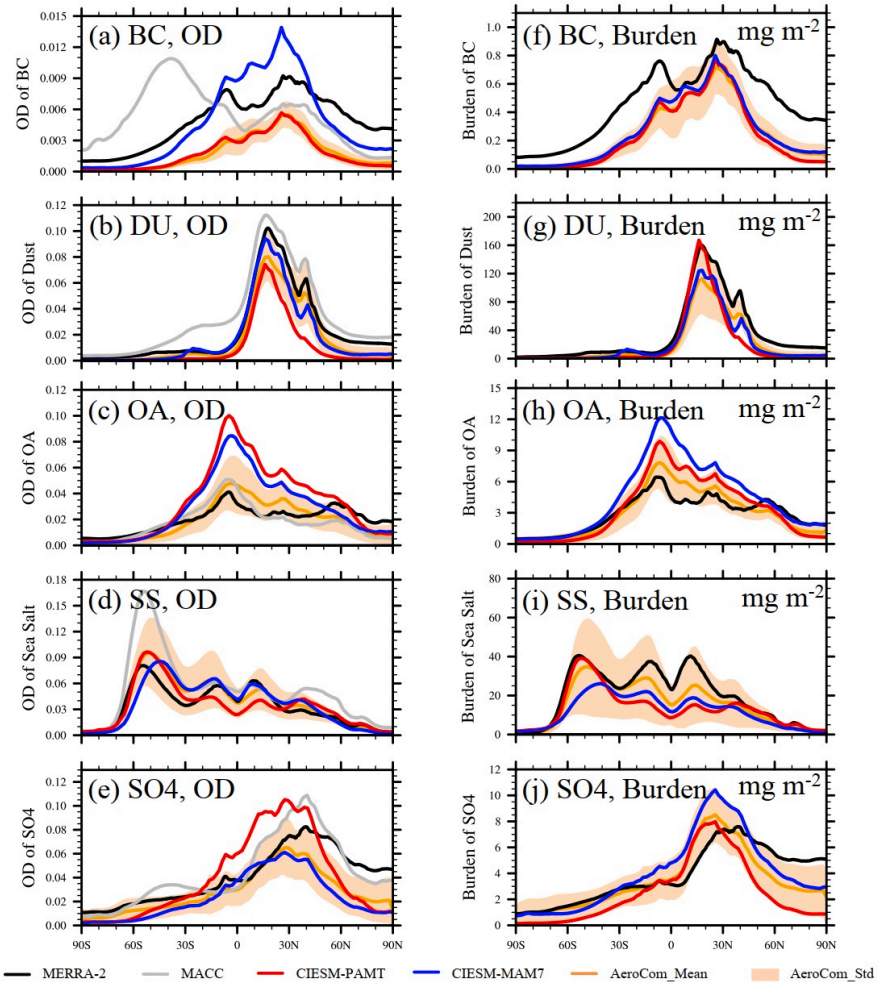


Figure 8. Zonal mean distributions of aerosol optical depth and burden for different aerosol types simulated by CIESM. Data include CIESM, reanalysis (MERRA-2 and MACC), and AeroCom3 simulations (multi-model mean AeroCom_Mean and geometric standard deviation AeroCom_Std). Columns represent optical depth and burden, and rows represent BC, DU, OA, SS, and SO4 aerosols.

For DU, the simulated burden in CIESM-PAMT is closer to MERRA-2 than that in CIESM-MAM7, whereas the OD simulated by CIESM-MAM7 shows closer agreement with the reanalysis products (Figs. 8b, g). Overall, results for both aerosol modules remain within the AeroCom3 uncertainty range. However, CIESM-PAMT fails to capture the peak around 45°N, indicating an underestimation of dust over northern hemisphere deserts such as the Taklamakan and Gobi. Simulations of OA are similar between CIESM-PAMT and CIESM-MAM7, with both overestimating burden and OD to varying degrees, especially in mid-to-low latitudes (Figs. 8c, h). POA emissions in OA are generally lower than in AeroCom3 (Table 7), but overall OA is higher than AeroCom3, suggesting overly strong SOA formation in CIESM. For SS, simulations of both OD and burden are comparable between CIESM-PAMT and CIESM-MAM7, falling within the AeroCom3 uncertainty range (Figs. 8d, i). Specifically, CIESM-PAMT shows closer agreement with the reanalysis products over the Southern Ocean, whereas CIESM-MAM7 shows slightly closer agreement in subtropical oceans. For SO4, CIESM-PAMT simulates lower

https://doi.org/10.5194/egusphere-2026-6615
Preprint. Discussion started: 10 November 2026
© Author(s) 2026. CC BY 4.0 License.

burden than CIESM-MAM7 (Fig. 8j) but significantly higher OD (Fig. 8e), which is related to the higher MEC for SO4 in PAMT (Table 7).

5.3 Aerosol Mass Concentrations in CIESM

5.3.1 Comparison between PAMT and MAM7

Figure 9 shows the aerosol mass size distributions of different aerosol components simulated by CIESM-PAMT and CIESM-MAM7. Overall, the total aerosol mass size distribution exhibits a clear bimodal structure, with the accumulation-mode peak primarily associated with internally mixed aerosols (SO4, BC, and OA) and the coarse-mode peak dominated by natural aerosols (SS and DU) (Figs. 9a, h). For DU and SS, both aerosol modules produce unimodal size distributions. However, compared with CIESM-MAM7 (Figs. 9j, k), the spectral peaks of DU and SS in CIESM-PAMT occur at smaller particle sizes (Figs. 9c, d). More pronounced differences are found for internally mixed aerosols. While the combined SO4+BC+OA distribution exhibits a single mode in CIESM-MAM7 (Fig. 9i), it shows a distinct bimodal structure in CIESM-PAMT (Fig. 9b), largely driven by the bimodal distribution of organic aerosol (OA) (Fig. 9g). These differences in aerosol mass size distributions can influence key aerosol processes, such as aerosol activation, coagulation, and dry and wet deposition, thereby contributing to differences in spatial distributions between the two aerosol modules.

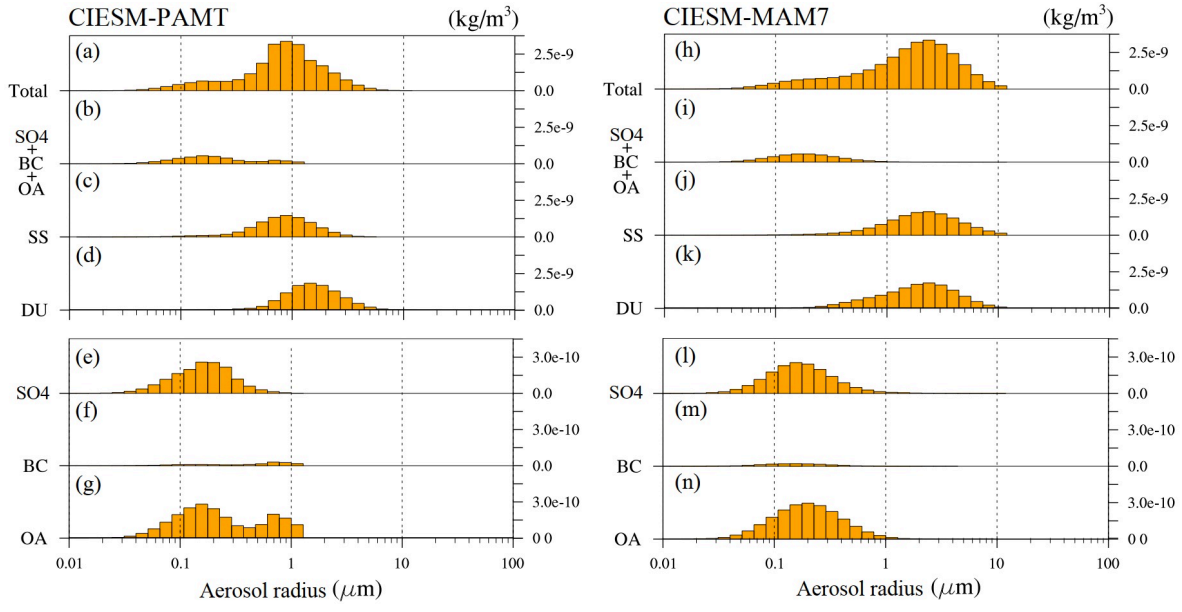


Figure 9. Near-surface aerosol mass size distributions simulated by CIESM-PAMT and CIESM-MAM7. Rows correspond to total aerosols, fine-mode aerosols (SO4+BC+OA), sea salt (SS), dust (DU), and individual fine-mode components (SO4, BC, and OA). The x-axis represents the aerosol particle radius after hygroscopic growth (wet radius), while the y-axis shows the corresponding dry aerosol mass concentration (excluding aerosol water) within each size bin. The aerosol size distribution is divided into 30 radius bins, and each bar represents the dry aerosol mass concentration (kg m^{-3}) contained within the corresponding wet-radius interval.

https://doi.org/10.5194/egusphere-2026-6615
Preprint. Discussion started: 10 November 2026
© Author(s) 2026. CC BY 4.0 License.

The zonal vertical distributions of aerosol mass concentrations for different components in CIESM-PAMT/MAM7 are shown in Fig. 10. The results indicate that both PAMT and MAM7 simulate the vertical distribution of aerosols in a generally consistent manner, with high concentrations in source regions and lower concentrations in non-source areas and the upper atmosphere. Specifically, CIESM-MAM7 shows stronger vertical transport for SO4, BC, and OA compared with CIESM-PAMT, allowing these aerosols to reach higher altitudes. In contrast, CIESM-MAM7 simulates weaker vertical transport for DU and SS, resulting in lower concentrations in the upper atmosphere and regions far from dust sources compared with CIESM-PAMT. This behavior is broadly consistent with Mahmood et al. (2016), who showed that convective transport of BC is more efficient in NCAR CESM-MAM than in CanAM-PAM, suggesting that differences in aerosol transport processes contribute to the contrasting aerosol distributions simulated by the two aerosol modules. Since the wind fields in both CIESM-PAMT and CIESM-MAM7 are nudged during simulations, long-range aerosol transport is mainly controlled by particle size and source–sink processes.

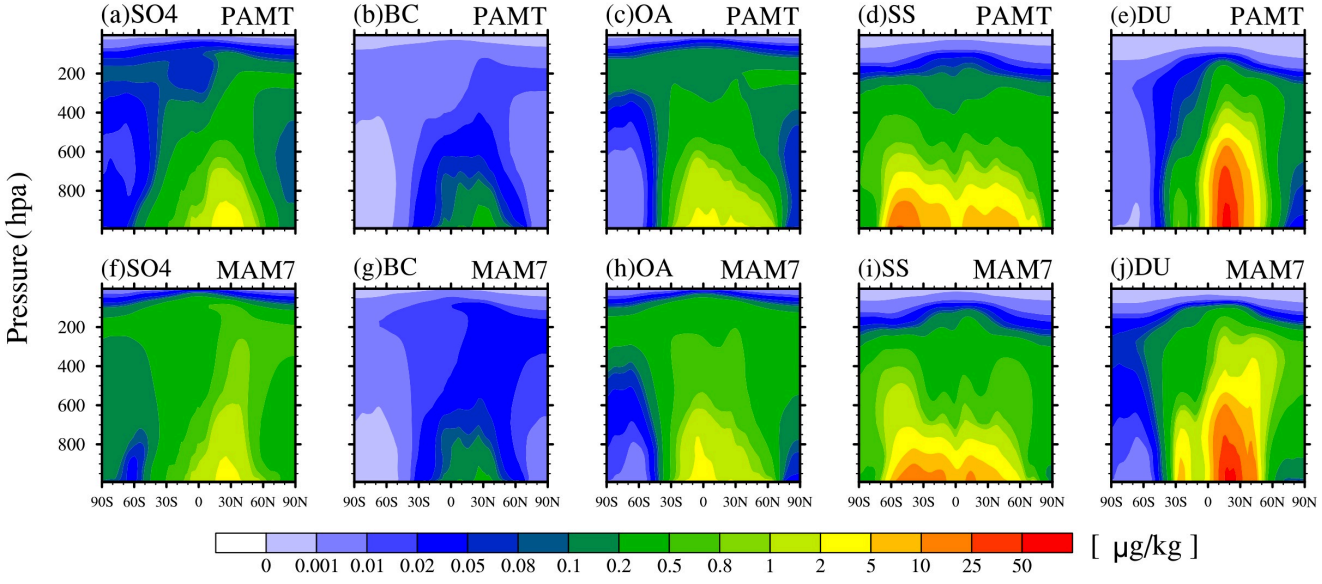


Figure 10. Zonal vertical distributions of aerosol mass concentrations simulated by CIESM-PAMT and CIESM-MAM7. Columns represent SO4, BC, OA, SS, and DU. Rows show CIESM-PAMT and CIESM-MAM7 results. Units: μg kg^{-1}.

Table 8 summarizes the sources (emissions, gas-to-particle conversion, and in-cloud production), sinks (convective wet deposition, stratiform wet deposition, and dry deposition), burdens, and lifetimes of different aerosol species simulated by CIESM-PAMT/MAM7. Overall, the two aerosol modules produce similar emissions for SO4, BC, and OA, as well as comparable gas-to-particle conversion rates for OA. In contrast, substantial differences are found in SO4 formation pathways, particularly in gas-to-particle conversion and in-cloud production. For SS and DU, whose emissions are calculated online, source strengths differ considerably between the two modules, with generally higher emissions in CIESM-MAM7. Consistent with the near balance between total sources and sinks, BC and OA exhibit similar overall source and sink magnitudes in both modules, whereas SO4, SS, and DU generally show larger source and sink terms in CIESM-MAM7.

https://doi.org/10.5194/egusphere-2026-6615
Preprint. Discussion started: 10 November 2026
© Author(s) 2026. CC BY 4.0 License.

Table 8. Source–sink budgets of different aerosol types in CIESM-PAMT and CIESM-MAM7.

Process	CIESM-PAMT					CIESM-MAM7				
	SO4	BC	OA	SS	DU	SO4	BC	OA	SS	DU
Sources [Tg year^{-1}]	133.7	8.6	146.6	1839.3	1020.3	166.0	8.6	146.3	5303.2	1770.5
Emission	5.3	8.6	42.1	1839.3	1020.3	5.2	8.6	42.0	5303.2	1770.5
Gas_to_particle conversion	58.3	/	104.6	/	/	35.7	/	104.3	/	/
In-cloud production	70.1	/	/	/	/	125.1	/	/	/	/
Sinks [Tg year^{-1}]	133.3	8.6	145.6	1835.7	1019.4	165.3	8.6	145.8	5299.7	1769.5
Convective wet deposition	41.2	2.8	49.7	241.8	234.3	24.5	1.3	28.7	357.9	114.9
Stratiform wet deposition	84.0	4.8	72.6	1265.5	252.4	120.5	5.6	96.1	1688.5	701.3
Dry deposition	8.1	0.95	23.3	328.4	532.7	20.3	1.7	21.0	3253.3	953.3
Burden [Tg]	1.8	0.15	2.3	8.0	15.7	2.6	0.17	3.0	7.9	16.2
Lifetime [day]	4.9	6.4	5.8	1.6	5.6	5.9	7.0	7.5	0.5	3.4

In details, SO4 exhibits notable differences in both source and sink processes between CIESM-PAMT and CIESM-MAM7. Although the total SO4 source is lower in CIESM-PAMT than in CIESM-MAM7 (133.7 vs. 166.0 Tg yr^{-1}), gas-to-particle conversion contributes more sulfate production (58.3 vs. 35.7 Tg yr^{-1}), whereas in-cloud production is lower (70.1 vs. 125.1 Tg yr^{-1}). Differences are also evident in the sink terms, with stronger convective wet deposition (41.2 vs. 24.5 Tg yr^{-1}) but weaker stratiform wet deposition (84.0 vs. 120.5 Tg yr^{-1}) and dry deposition (8.1 vs. 20.3 Tg yr^{-1}) in CIESM-PAMT. Correspondingly, the sulfate burden and lifetime are reduced in CIESM-PAMT (1.8 Tg and 4.9 days) relative to CIESM-MAM7 (2.6 Tg and 5.9 days). For both BC and OA, CIESM-PAMT produces shorter atmospheric lifetimes than CIESM-MAM7 (6.4 and 5.8 days vs. 7.0 and 7.5 days, respectively). Convective wet deposition is stronger in CIESM-PAMT (2.8 vs. 1.3 Tg yr^{-1} for BC and 49.7 vs. 28.7 Tg yr^{-1} for OA), while stratiform wet deposition and/or dry deposition are generally lower than in CIESM-MAM7. Despite differences in sink partitioning, the overall source and sink magnitudes for OA and BC remain broadly comparable between the two aerosol modules. SS shows the largest discrepancy in source strength between the two aerosol modules. The total sea-salt source in CIESM-PAMT (1839.3 Tg yr^{-1}) is substantially lower than that in CIESM-MAM7 (5303.2 Tg yr^{-1}), whereas the simulated burdens are very similar (8.0 vs. 7.9 Tg). Consequently, the sea-salt lifetime is considerably longer in CIESM-PAMT (1.6 days) than in CIESM-MAM7 (0.5 days). The relative contributions of individual sink processes also differ, with dry deposition contributing more strongly in CIESM-MAM7 and wet deposition contributing more strongly in CIESM-PAMT. Similarly, DU emissions are lower in CIESM-PAMT than in CIESM-MAM7 (1020.3 vs. 1770.5 Tg yr^{-1}), while the simulated burdens remain comparable (15.7 vs. 16.2 Tg). As a result, the dust lifetime is substantially longer in CIESM-PAMT (5.6 days) than in CIESM-MAM7 (3.4 days). Compared with CIESM-MAM7, CIESM-PAMT exhibits lower stratiform wet deposition (252.4 vs. 953.3 Tg yr^{-1}) and higher convective wet deposition (234.3 vs. 114.9 Tg yr^{-1}), whereas dry deposition contributes a comparable fraction of the total aerosol removal in both aerosol modules (~53%).

https://doi.org/10.5194/egusphere-2026-6615
Preprint. Discussion started: 10 November 2026
© Author(s) 2026. CC BY 4.0 License.

In summary, changes in aerosol representation and the associated process treatments substantially modify the source–sink budgets of aerosols in CIESM. The differences between CIESM-PAMT and CIESM-MAM7 are pronounced for SO4 formation pathways and for the source–sink budgets of SS and DU, whereas BC and OA exhibit relatively similar global budgets despite differences in sink partitioning.

5.3.2 Evaluation against In-Situ Observations

Ground-based observations are considered the most reliable data for evaluating model performance. To evaluate CIESM's simulation of surface mass concentrations of BC, OA, and SO4, this study collected observations from the United States (IMPROVE), Europe (GAW/EMEP), Canada (ECCC), and China (CAWNET+CARE-China) for the period 2000–2014. Figure 11 shows the spatial distributions and scatter comparisons of BC, OA, and SO4 simulated by CIESM-PAMT/MAM7 against these observations, along with the mean relative errors (RE) for each simulation. Overall, both aerosol modules in CIESM tend to underestimate surface BC and OA concentrations, while the simulated SO4 agrees well with observations, showing only a slight overestimation (~2%). Compared with CIESM-MAM7, CIESM-PAMT shows improvements in reproducing surface concentrations of BC, OA, and SO4, with relative errors reduced from −29.8%, −34.1%, and 2.3% to −6.7%, −20.5%, and 2.2%, respectively (Figs. 11g-l). Specifically, the underestimation of BC in CIESM is mainly concentrated in the United States and Canada, whereas the simulation for Europe is generally consistent with observations. In China, the simulation is overall reasonable, with some regional underestimation that is improved in PAMT. The underestimation of OA is mainly observed in China, where PAMT performs slightly better. For SO4, both CIESM-PAMT and CIESM-MAM7 show similar performance and good agreement with observations. Simulations over the United States, Europe, and China tend to be slightly high, while those over Canada are underestimated. However, only one suitable observation site is available in Canada (the Alert station; 62.5°W, 82.5°N), limiting the representativeness of this evaluation. This limitation is partly attributable to the sparse aerosol composition measurements available from the ECCC/NAPS network and partly to the stringent data-screening criteria adopted in this study, whereby annual means were derived from seasonal averages, and each seasonal average required observations from at least three months. Nevertheless, Figs. 11a–f show that both CIESM-PAMT and CIESM-MAM7 underestimate BC, OA, and SO4 concentrations at the Alert station, consistent with findings from previous studies (Mahmood et al., 2016). In summary, the improvements in CIESM-PAMT for BC and OA mainly reflect a reduction in the underestimation seen in CIESM-MAM7 over the United States and China, while SO4 simulations remain largely consistent with the original aerosol module.

https://doi.org/10.5194/egusphere-2026-6615
Preprint. Discussion started: 10 November 2026
© Author(s) 2026. CC BY 4.0 License.

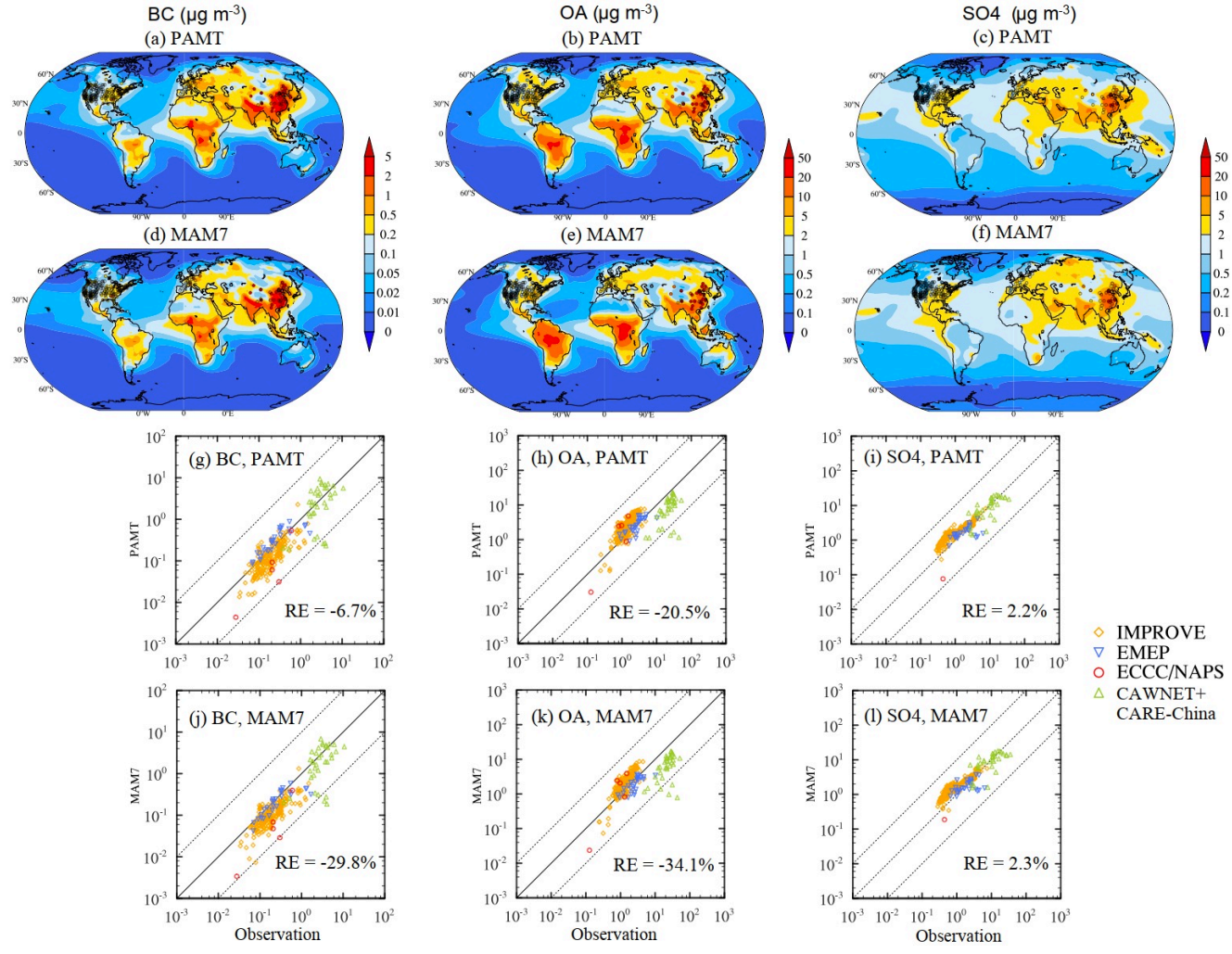


Figure 11. Comparison of surface mass concentrations of BC, OA, and SO4 simulated by CIESM-PAMT and CIESM-MAM7 with observations. Panels (a–f) show spatial distributions, and panels (g–l) show scatter plots. Observation sites include IMPROVE, EMEP, ECCC/NAPS, and CAWNET+CARE-China during 2000-2014. Units: μg m^{-3}.

Surface-based stations cannot capture aerosol mass concentrations over the ocean. Therefore, this study collected shipborne observations from 2000 to 2014 to evaluate near-surface SO4 aerosol mass concentrations in marine regions, as shown in Fig. 12 and Table 9. Figure 12 presents the tracks of the 10 cruises (Fig. 12a), the observed SO4 concentrations, and their comparison with the CIESM simulations (Figs. 12 b-c). The relative errors for each cruise and for all cruises combined are summarized in Table 9. Compared with observations, CIESM generally overestimates SO4 concentrations across different ocean regions, particularly along the U.S. East Coast (NEAQS2002, NEAQS2004, WACS, and WACS2), the western coast of South America (VOCALS), and the Indian Ocean (DYNAMO). Simulated SO4 concentrations are underestimated in the Sea of Japan and the Pacific (ACEASIA), the U.S. West Coast (CALNEX), and the Gulf of Mexico (TEXAQS2006). In near-polar regions (ICEALOT), CIESM-MAM7 underestimates SO4, whereas CIESM-PAMT shows a slight overestimation.

https://doi.org/10.5194/egusphere-2026-6615
Preprint. Discussion started: 10 November 2026
© Author(s) 2026. CC BY 4.0 License.

Overall, the simulations of marine SO4 by CIESM-PAMT and CIESM-MAM7 are similar, with both generally overestimating concentrations (REs of 64.9% and 54.6%, respectively).

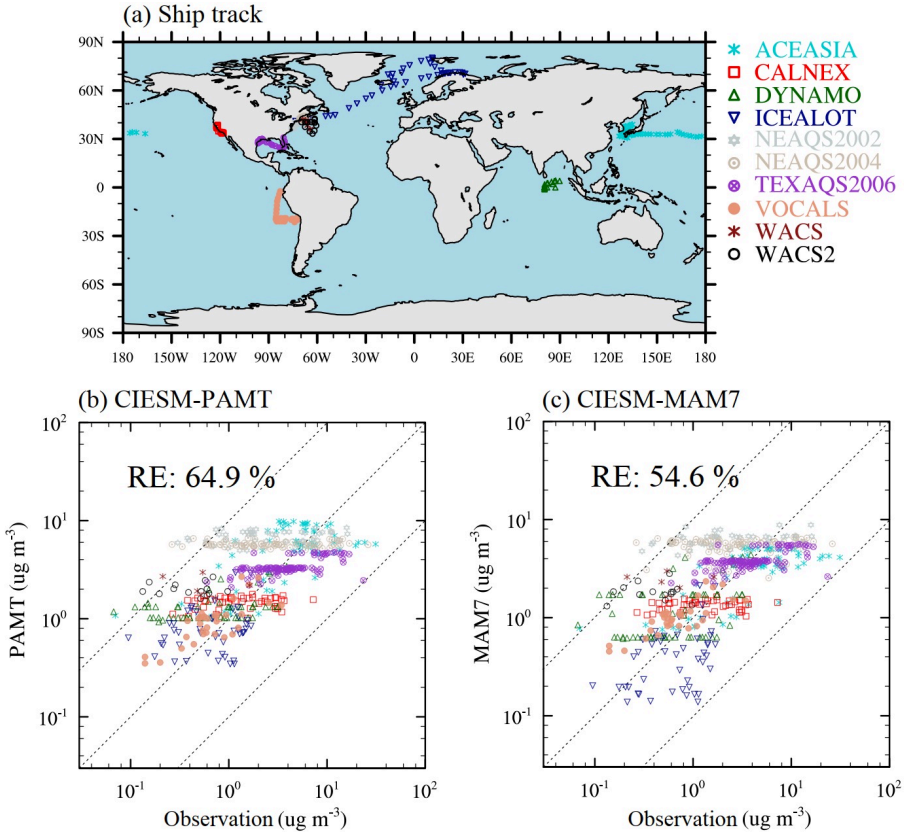


Figure 12. SO4 mass concentrations simulated by CIESM-PAMT and CIESM-MAM7 compared with shipborne observations during 2000-2014. Panels (a) show spatial distributions, and panels (b–c) show scatter plots. Units: μg m^{-3}. The relative error (RE, %) of all ship tracks is reported in the upper-right corner of each panel.

Table 9. Relative errors (RE, %) of CIESM-PAMT and CIESM-MAM7 relative to SHIP observations for SO4 mass concentrations. Light green shading highlights the better-performing model. No shading is applied when both models have absolute relative errors below 5%, indicating comparable performance.

Module	Ship track										
	ACEASIA	CALNEX	DYNAMO	ICEALOT	NEAQS 2002	NEAQS 2004	TEXAQS 2006	VOCALS	WACS	WACS2	ALL
PAMT	-5.8	-13.4	36.6	5.8	60.1	28.2	-31.0	19.1	217.4	331.6	64.9
MAM7	-44.4	-20.4	38.2	-38.4	44.9	20.7	-21.5	23.6	248.1	295.0	54.6

Figure 13 shows the comparison between CIESM-PAMT/MAM7 simulated fine particulate matter (PM2.5) and particulate matter with aerodynamic diameter less than 10 μm (PM10) mass concentrations and ground-based observations. The results indicate a significant underestimation of both PM2.5 and PM10 by CIESM. For PM2.5, the underestimation is similar for both CIESM-PAMT and CIESM-MAM7, approximately 30.5%, with the largest discrepancies occurring in China. Similar

https://doi.org/10.5194/egusphere-2026-6615
Preprint. Discussion started: 10 November 2026
© Author(s) 2026. CC BY 4.0 License.

low biases have been reported in previous multi-model evaluations, where most global aerosol models tend to underestimate surface PM2.5 concentrations (Whaley et al., 2022). For PM10, the underestimation is more pronounced in CIESM-PAMT (RE = −57.5%), mainly over China and Canada. The overall coarse particle size of fine aerosols (BC, OA, and SO4) in CIESM-PAMT (Fig. 9) enhances removal processes, leading to lower column concentrations in the atmosphere (Table 8). Although DU and SS particles in CIESM-PAMT are smaller than in CIESM-MAM7, their low surface emission fluxes (Table 8) and efficient vertical transport (Fig. 10) result in lower near-surface concentrations. In northeastern China, proximity to the Gobi and Taklamakan deserts combined with strong anthropogenic emissions contributes to the pronounced underestimation in this region by CIESM-PAMT.

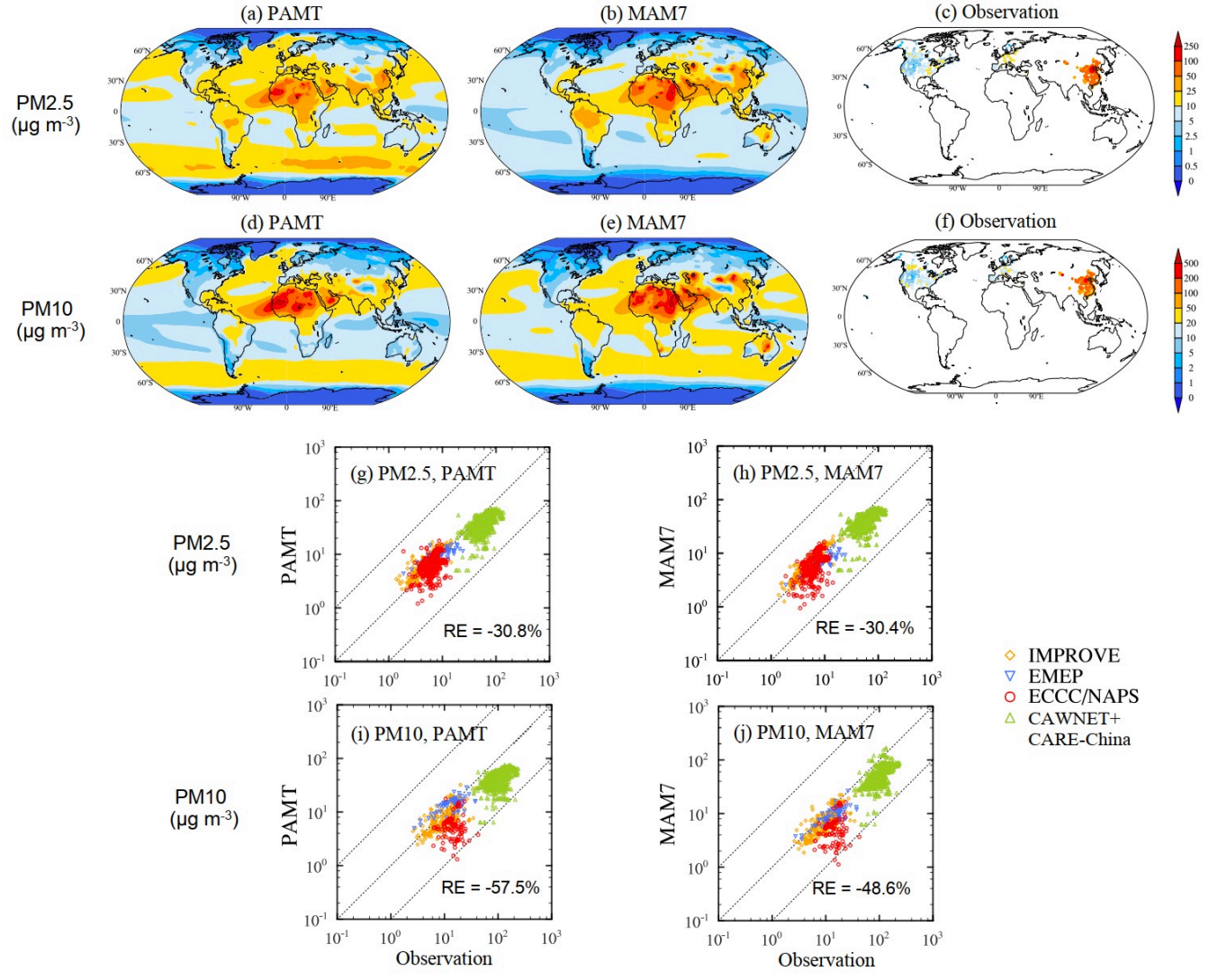


Figure 13. Spatial distributions and scatter plots comparing simulated PM2.5 and PM10 with observations. Observation sites include IMPROVE, EMEP, ECCC/NAPS, and CAWNET+CARE-China during 2000-2014. Units: μg m^{-3}.

https://doi.org/10.5194/egusphere-2026-6615
Preprint. Discussion started: 10 November 2026
© Author(s) 2026. CC BY 4.0 License.

5.4 Aerosol Number Concentrations in CIESM

This study compares the zonal vertical distributions of aerosol number concentrations simulated by CIESM-PAMT/MAM7, as shown in Fig. 14. Compared with the differences in the vertical distribution of aerosol mass concentration between the two modules, the discrepancies in their simulation of aerosol number concentration are even more pronounced. CIESM-PAMT predicts higher total aerosol number concentrations as well as higher concentrations across different size bins, both in surface source regions and at higher altitudes, compared with CIESM-MAM7.

The formation of ultrafine particles (diameter < 20 nm) is mainly associated with gas_to_particle conversion. The conversion efficiency in CIESM-PAMT is higher than in CIESM-MAM7 (Table 8), leading to the generation of more fine particles. Coagulation, which involves the collision and coalescence of aerosol particles, is crucial for the growth of ultrafine particles into fine particles (tens to hundreds of nanometers). Coagulation reduces the total number of aerosols while increasing the mean radius of the size distribution. In CIESM-PAMT, the coagulation scheme divides the aerosol size distribution into 21 sections and explicitly accounts for collisions within and between these bins, allowing a more detailed and accurate simulation of the coagulation process. In contrast, CIESM-MAM7 only considers coagulation among a few modes. Condensation is also an important process for aerosol growth. Both CIESM-PAMT and CIESM-MAM7 account for the condensation of sulfate and volatile organic gases, which are mainly emitted from the surface, so their impact is more pronounced in the lower atmosphere. Sensitivity experiments in which nucleation and coagulation processes were turned on and off show that differences in these processes between the two modules are the primary factor controlling the number of fine particles with diameters of tens to hundreds of nanometers (Wang et al., in preparation).

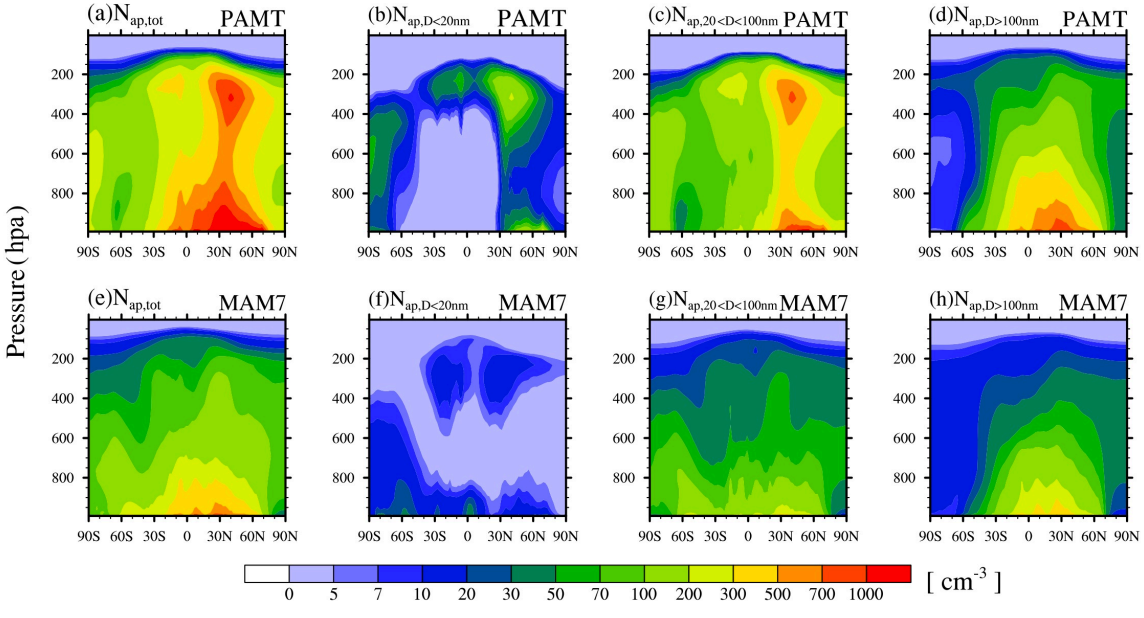


Figure 14. Vertical distributions of aerosol number concentrations simulated by CIESM-PAMT and CIESM-MAM7. Columns represent total aerosol number (N_{ap_tot}), particles smaller than 20 nm ($N_{ap,D<20nm}$), particles between 20–100 nm ($N_{ap,20nm<D<100nm}$), and particles larger than 100 nm ($N_{ap,D>100nm}$). Units: cm^{-3}.

https://doi.org/10.5194/egusphere-2026-6615
Preprint. Discussion started: 10 November 2026
© Author(s) 2026. CC BY 4.0 License.

Figure 15 shows the spatial distribution of aerosol number concentrations larger than 20 nm ($N20$) simulated by CIESM-PAMT and CIESM-MAM7, along with scatter comparisons against ground-based observations. Spatially, CIESM-PAMT predicts higher $N20$ concentrations over land than CIESM-MAM7, while the distributions over oceans are similar but still slightly higher. Compared with observations, both modules underestimate $N20$, with relative errors of −48% for CIESM-PAMT and −80% for CIESM-MAM7. Overall, CIESM-PAMT demonstrates superior performance over CIESM-MAM7 in simulating aerosol number concentrations.

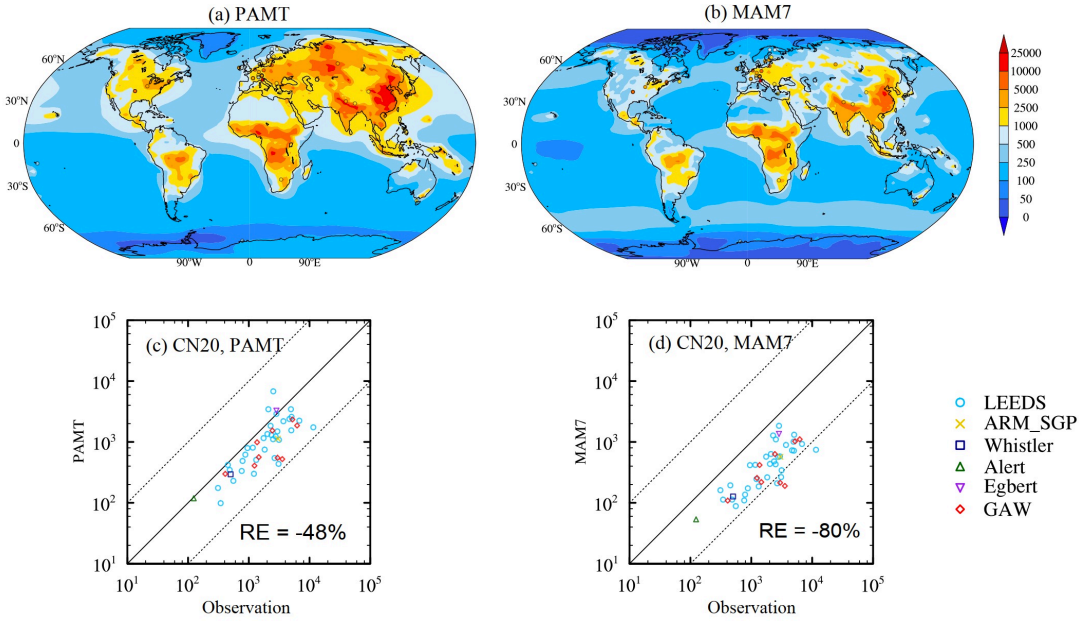


Figure 15. Surface distributions and scatter plots of number concentrations of aerosols larger than 20 nm (N20) simulated by CIESM-PAMT and CIESM-MAM7 during 2000-2014. Units: cm^{-3}.

5.5 Evaluation of Aerosol Simulations over the Arctic

Polar regions have attracted considerable attention because of their unique geographical setting and high sensitivity to climate change (AMAP, 2021; Mahmood et al., 2016; von Salzen et al., 2022; Whaley et al., 2022). Since the existing ground-based aerosol sites are predominantly located in the Arctic (>60°N), this section focuses on evaluating the performance of CIESM-PAMT/MAM7 in simulating Arctic aerosols. The results are summarized in Fig. 16 and Table 10.

Table 10. Relative errors (RE, %) of CIESM-PAMT and CIESM-MAM7 with respect to in situ observations over the Arctic (> 60°N). For SO4, the values in parentheses are based on shipborne observations from the ICEALOT campaign at latitudes north of 60°N. Light green shading indicates the better-performing model. No shading is applied when both models have absolute relative errors below 5%, indicating comparable performance.

Model	AOD	AOD_f	AOD_c	AE	BC	OA	SO4	CN20	PM2.5	PM10
CIESM-PAMT	-18.8	2.7	-51.0	-7.6	9.8	50.2	8.0 (-16.7)	-36.3	-4.9	-46.6
CIESM-MAM7	-39.3	-15.1	-85.5	-17.1	-35.0	13.0	70.0 (-52.2)	-77.5	-28.4	-58.2

https://doi.org/10.5194/egusphere-2026-6615
Preprint. Discussion started: 10 November 2026
© Author(s) 2026. CC BY 4.0 License.

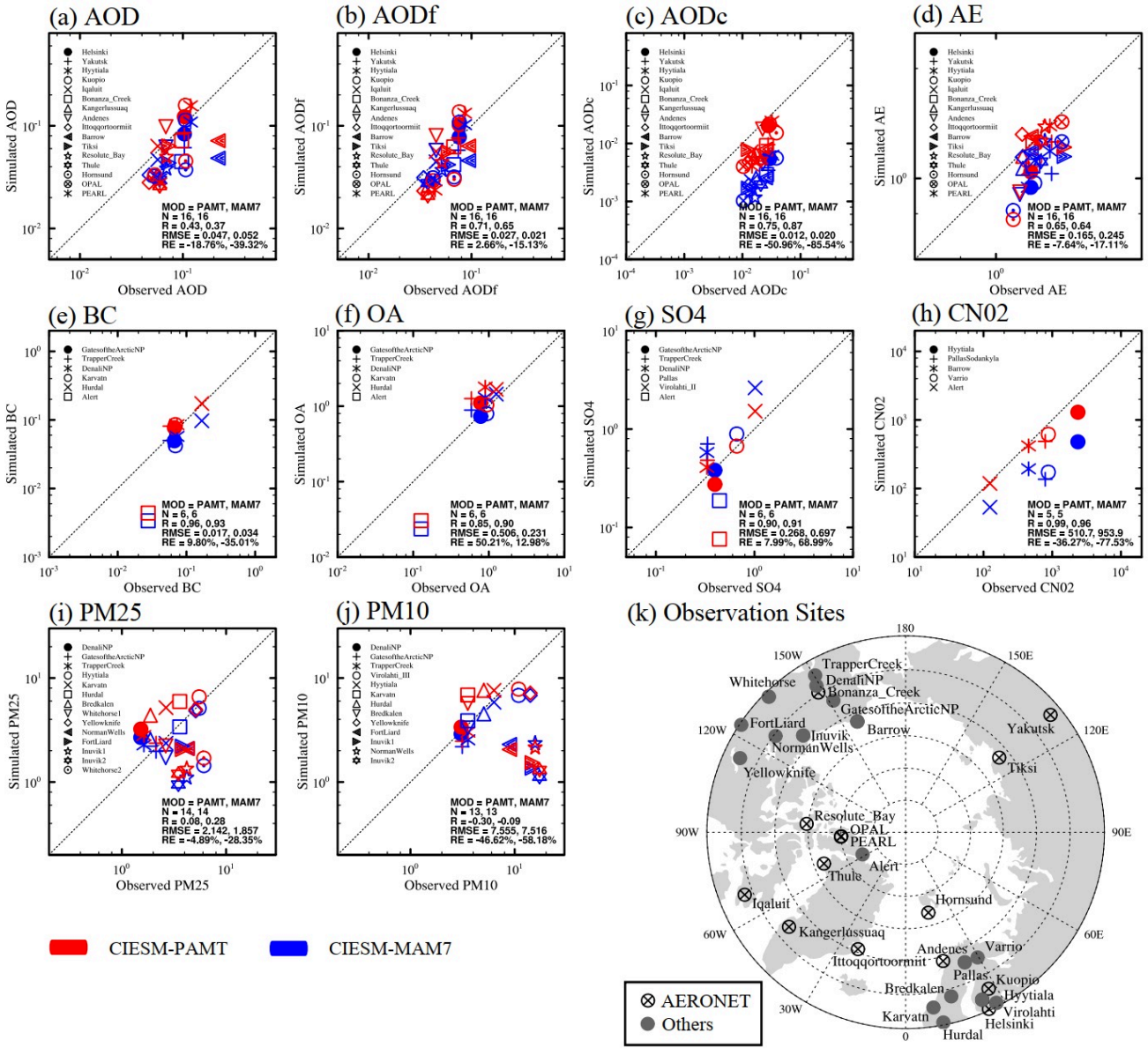


Figure 16. Comparison of ground-based observations and model simulations over the Arctic (>60°N). Panels (a–j) show scatterplots of annual mean values for different variables, and panel (k) presents the spatial distribution of the observation sites. To maintain consistency with the other analyses in this study, annual mean aerosol optical properties (***AOD***, $\boldsymbol{AOD_f}$, $\boldsymbol{AOD_c}$, and ***AE***) were calculated by averaging the monthly mean observations and corresponding model simulations shown in Fig. 6 for 2010. For all other variables, annual means were derived for the period 2000–2014 by averaging seasonal means, with each seasonal mean requiring observations from at least three months. Red and blue symbols denote CIESM-PAMT and CIESM-MAM7, respectively. The number of sites (N), correlation coefficient (R), root mean square error (RMSE), and relative error (RE) are reported in the lower-right corner of each panel.

Before the implementation of the new aerosol module, CIESM-MAM7 systematically underestimated Arctic aerosol optical properties (AOD, AOD_f, AOD_c, and AE), whereas these systematic biases were substantially reduced in CIESM-PAMT (Figs.

https://doi.org/10.5194/egusphere-2026-6615
Preprint. Discussion started: 10 November 2026
© Author(s) 2026. CC BY 4.0 License.

16a–d; Table 10). In particular, although CIESM-PAMT exhibited an overall positive bias in AOD_f at the global scale (Section 5.1.2), it performed considerably better over the Arctic and effectively corrected the underestimation found in CIESM-MAM7 (Fig. 16b). CIESM-PAMT also showed overall improved performance in simulating the mass concentrations of individual aerosol components (Figs. 16e–g; Table 10). For BC, CIESM-MAM7 underestimated concentrations at all Arctic sites, with the largest bias occurring at Alert (Fig. 16e). CIESM-PAMT substantially alleviated this underestimation, bringing the simulated values at most sites much closer to the observations, although BC remained underestimated at Alert. For OA, CIESM-PAMT produced generally higher concentrations than CIESM-MAM7. While this increased the existing positive bias at most sites, OA concentrations at Alert were still underestimated. In contrast to carbonaceous aerosols, SO4 concentrations simulated by CIESM-PAMT were generally lower than those from CIESM-MAM7 (Fig. 16g). This effectively reduced the widespread overestimation of SO4 over the Arctic but also resulted in a more pronounced underestimation at the Alert site. For the aerosol number concentration CN20, CIESM-PAMT also demonstrated clear improvements (Fig. 16h). Although both model versions underestimated CN20, the bias was substantially reduced in CIESM-PAMT. Similar improvements were found for PM2.5 and PM10 (Figs. 16i–j). CIESM-MAM7 showed pronounced underestimation for both variables, whereas the higher concentrations simulated by CIESM-PAMT generally reduced the negative bias, as reflected by the smaller relative errors. However, the increased concentrations also introduced noticeable positive biases at several sites, leading to larger RMSE values, indicating that further improvements are still needed.

Overall, CIESM-PAMT consistently performs better than CIESM-MAM7 in reproducing Arctic aerosol optical properties, mass concentrations, and number concentrations (Table 10). These improvements provide a more reliable foundation for future investigations of aerosol processes and aerosol–climate interactions in the Arctic using CIESM-PAMT.

6 Conclusions

In this study, a new aerosol module PAMT (Piecewise lognormal approximation Aerosol Model for Tsinghua University) was coupled into a climate model CIESM to improve its representation of aerosol processes. Compared with the original MAM7 scheme, PAMT reduces the number of aerosol tracers from 31 to 24, significantly lowering computational complexity. At the same time, it introduces a Piecewise Lognormal Approximation method (PLA) to represent the aerosol size distribution, which achieves a better balance between computational efficiency and simulation accuracy. The coupling of PAMT also incorporates updated parameterizations for key aerosol processes, some of which are based on recent field and laboratory studies (Table 2).

Table 11 summarizes CIESM-PAMT and CIESM-MAM7 simulations of different aerosol variables, evaluated against high-reliability datasets including ground-based, shipborne, and satellite observations, excluding reanalysis and multi-model results. The results indicate that, relative to the satellite observations, both CIESM-PAMT and CIESM-MAM7 overestimate AOD and AOD_f, while underestimating AOD_c and AE. Overall, CIESM-MAM7 shows better agreement with the satellite observations for AOD and AOD_f, whereas CIESM-PAMT performs better in simulating AOD_c and AE. Nevertheless,

https://doi.org/10.5194/egusphere-2026-6615
Preprint. Discussion started: 10 November 2026
© Author(s) 2026. CC BY 4.0 License.

comparisons with ground-based observations suggest an overall improvement in aerosol optical properties when using PAMT. The relative errors for AOD, AOD_c, and AE decrease from −13.7%, −64.1%, and −27.7% in CIESM-MAM7 to 10.5%, −24.9%, and −8.6% in CIESM-PAMT, respectively. Both aerosol modules overestimate AOD_f, with relative errors of 11.9% and 30.1% for CIESM-MAM7 and CIESM-PAMT, respectively, indicating a more pronounced positive bias in CIESM-PAMT. For mass and number concentrations of different aerosol species and sizes, CIESM-PAMT shows relative errors of −6.7%, −20.5%, and −48% for BC, OA, and $N20$, respectively, all improvements over CIESM-MAM7 (-29.8%, -34.1%, and -80.0%). Both modules perform similarly for SO4 (2.2% vs. 2.3%) and PM2.5 (−30.8% vs. −30.4%), while CIESM-PAMT is slightly less accurate than MAM7 for PM10 (−57.5% vs. −48.6%) and shipborne sulfate (64.9% vs. 54.6%). When the evaluation is further restricted to the Arctic (> 60°N), CIESM-PAMT exhibits consistent improvements over CIESM-MAM7 in simulating aerosol optical properties, aerosol mass concentrations, and aerosol number concentrations (Table 10).

Overall, CIESM-PAMT reasonably reproduces the spatiotemporal distribution of major aerosol species and their optical properties, particularly improving the simulation of organic aerosols and aerosol optical depth. These results demonstrate that coupling the new module effectively enhances CIESM's ability to simulate the global aerosol system and its radiative effects, providing a solid foundation for further studies on aerosol–cloud interactions.

Table 11. Summary of CIESM-PAMT/MAM7 simulation results compared with observational data, including observations and relative errors. Light green highlights well-performing coupling schemes. No annotation is made when both models have biases below 5%, indicating no significant difference between the two.

Variable		CIESM-PAMT	CIESM-MAM7	Observation	Data source
Values	AOD	0.168	0.153	0.152	MERGED-FMI
	AOD_f	0.120	0.114	0.091	AATSR-SU
	AOD_c	0.048	0.039	0.058	AATSR-SU
	AE	0.871	0.575	0.940	AATSR-SU
Relative error [%]	AOD	10.54	-13.72	/	AERONENT
	AOD_f	30.06	11.87	/	AERONENT
	AOD_c	-24.88	-64.06	/	AERONENT
	AE	-8.60	-27.72	/	AERONENT
	BC	-6.7	-29.8	/	Ground site
	OA	-20.5	-34.1	/	Ground site
	SO4	2.2	2.3	/	Ground site
	SO4	64.87	54.59	/	Ship
	PM2.5	-30.8	-30.4	/	Ground site
	PM10	-57.5	-48.6	/	Ground site
	$N20$	-48	-80	/	Ground site

https://doi.org/10.5194/egusphere-2026-6615
Preprint. Discussion started: 10 November 2026
© Author(s) 2026. CC BY 4.0 License.

Despite these advances, several issues require further investigation. First, dust aerosols do not account for sulfate coatings, which may influence cloud condensation nuclei activity and cloud microphysics. Second, PAMT currently does not explicitly simulate the evolution of gaseous ammonia, potentially leading to biases in ammonium aerosols over regions with strong agricultural emissions. Third, wet deposition is not fully coupled with convective transport, so the treatment of convective wet removal remains relatively simple. Overall, the ultimate goal is to develop a physically consistent and computationally efficient aerosol–climate model, providing high-quality model foundations and scientific support for the next phase of international coupled model comparison projects.

This paper mainly presents the coupling of PAMT in CIESM and its evaluation for aerosols. A comprehensive evaluations of cloud properties in simulations with CIESM-PAMT (total/high/middle/low/ice/liquid cloud fractions, liquid/ice cloud water paths, cloud droplet effective radius, cloud droplet number concentration, and so on), precipitation, radiation (top-of-atmosphere and cloud radiative effects), and aerosol–cloud interactions are presented in Part 2 of this series.

https://doi.org/10.5194/egusphere-2026-6615
Preprint. Discussion started: 10 November 2026
© Author(s) 2026. CC BY 4.0 License.

Appendix A: Tuning Strategy

In CIESM, tunable parameters mainly include the evaporation efficiency of convective clouds (ke), cloud-fraction adjustment factors for deep convection (cldfrc_dp1 and cldfrc_dp2) and shallow convection (cldfrc_sh1 and cldfrc_sh2), the convective entrainment rate (dmpdz), and the minimum relative humidity for high stable clouds (cldfrc_rhminh) (Neale et al., 2012). Although default values exist for these parameters, our goal is to adjust as few parameters as possible while sequentially satisfying the following priorities: 1) the longwave and shortwave radiative fluxes at top of atmosphere to closely match observations, with an approximately balanced global, annual mean net radiation; 2) the longwave, shortwave, and net cloud radiative effects to agree with observations; and 3) cloud fraction, cloud water path, and precipitation are as close to observations as possible. Given that tuning is just performed as a pre-simulation adjustment, the adjustment criterion is based on agreement with global annual means rather than reproducing detailed two- or three-dimensional spatial patterns. This approach helps avoid excessive parameter compensation that may compromise the physical consistency of the model. Each tuning factor must be varied within a physically reasonable range, and tuning should first aim at achieving TOA radiative balance before addressing the other criteria. Since MAM7 is the aerosol module originally embedded in CIESM, the above tuning strategy is primarily applied to CIESM-MAM7. After the tuning parameters are determined, no further adjustments are made for CIESM-PAMT, which directly adopts these values to ensure consistent parameter settings between the two modules during evaluation. The results show that running CIESM-PAMT with the parameters tuned for CIESM-MAM7 also satisfies the TOA radiative balance requirement.

After extensive sensitivity tests, we recommend the following parameter settings for CIESM: ke = 5e-7, cldfrc_dp1 = 0.03, cldfrc_dp2 = 200, cldfrc_sh1 = 0.04, cldfrc_sh2 = 500, dmpdz = −2e-3, and cldfrc_rhminh = 0.85. Among these, ke (default: 3.5e-5) and cldfrc_dp1 (default: 0.05) are based on sensitivity tests, while the remaining parameters retain their default model values.

Appendix B: Additional Diagnostic Variables

In evaluating the aerosol simulations of CIESM, this study follows the AeroCom phase III (AeroCom3) (Gliß et al., 2021). Accordingly, several diagnostic variables required by AeroCom3 are added to CIESM. Based on the AeroCom3 protocol, the diagnostics introduced in this study include: aerosol surface emission flux (Tg year^{-1}), aerosol lifetime (days), aerosol burden (Tg), optical depth (OD, unitless), mass extinction coefficient (MEC, $\mathrm{m}^2\ \mathrm{g}^{-1}$), Ångström exponent ($AE$, unitless), and fine-/coarse-mode aerosol optical depth (AOD_f and AOD_c, unitless).

In PAMT, aerosol optical properties are calculated from the wet aerosol size distribution and chemical composition using Mie theory (Section 2.3.4). For internally mixed particles, the effective complex refractive index is derived using the Maxwell–Garnett approximation (Maxwell Garnett, 1905), after which aerosol extinction coefficients are computed and vertically integrated to obtain AOD. A similar framework is employed in MAM7, but volume mixing is used instead of the

https://doi.org/10.5194/egusphere-2026-6615
Preprint. Discussion started: 10 November 2026
© Author(s) 2026. CC BY 4.0 License.

Maxwell–Garnett mixing rule for internally mixed aerosols, as the differences between the two approaches are found to be negligible (Ghan and Zaveri, 2007).

In AeroCom3, AE is calculated using AOD at 870 nm and 440 nm (or 550 nm), following a prescribed formula. However, neither PAMT nor MAM7 provides AOD output at 870 nm and 440 nm. Instead, PAMT outputs AOD at 860 and 550 nm, while MAM7 provides AOD at 850, 550, and 350 nm. Therefore, this study uses the available AOD wavelengths adopt the similar calculation and computes AE as follows:

$$AE_{PAMT} = -\frac{\ln(AOD_{550}/AOD_{860})}{\ln(550/860)},\ AE_{MAM7} = -\frac{\ln(AOD_{350}/AOD_{850})}{\ln(350/850)}, \quad \text{(S1)}$$

where AOD_{350}, AOD_{550}, AOD_{850}, and AOD_{860} represent AOD at 350 nm, 550 nm, 850 nm, and 860 nm, respectively.

AeroCom3 evaluates not only AOD and AE, but also fine- and coarse-mode AOD (AOD_f and AOD_c). However, most participating models do not explicitly output these quantities. Instead, different diagnostic strategies are applied (Gliß et al., 2021). A commonly adopted approach is to attribute AOD from particles with dry or wet radii smaller than 0.5 µm to AOD_f, and the remainder to $AODc$. Some models further distinguish aerosol types by mode or section, for example assigning coarse SS and DU to $AODc$, while others are classified as fine mode (see (Gliß et al., 2021), Supplement 1.ods).

In CIESM-MAM7, AOD is directly diagnosed for each aerosol mode. The "coarse sea salt" and "coarse dust" modes are broadly consistent with the AeroCom3 definition of coarse-mode particles (radius > 0.5 µm) (Table 1). Therefore, AOD_c is defined as the sum of optical depths from these two modes, while AOD_f is obtained from all remaining modes.

In contrast, the CIESM-PAMT is more complex. As summarized in Table 1, the sectional size ranges do not align exactly with a 0.5 µm separation. PAMT diagnoses 5 extinction coefficients within each grid cell, including internally mixed BC/OA/SO4 (INT SEC1+ SEC2+ SEC3), externally mixed BC and OA (BC SEC and OC SEC), as well as sea salt (SS SEC1+ SEC2) and dust (DU SEC1+ SEC12). In addition, PAMT uses the Maxwell–Garnett approximation to calculate the optical properties and aerosol optical depth of internally mixed aerosols while accounting for the lensing effect associated with internally mixed black carbon (BC) and sulfate aerosols. Therefore, AOD_f and AOD_c cannot be directly obtained from existing output fields, and a diagnostic approach is required.

The aerosol optical depth is defined as the vertical integral of the extinction coefficient (β_{ext}). According to Mie theory, for a given wavelength, aerosol composition, and relative humidity, the extinction coefficient can be expressed as (Hand and Malm, 2007):

$$\beta_{ext} = \int_0^\infty Q_{ext}(r)\pi r^2 n(r)dr = \overline{Q_{ext}}\pi \int_0^\infty r^2 n(r)dr, \quad \text{(S2)}$$

where $\overline{Q_{ext}}$ denotes a bulk extinction efficiency representative of each aerosol type.

Assuming spherical particles with an effective radius r_{eff} and aerosol mass concentration M_a, and using the definition of effective radius as well as the relation between particle size and mass, the second moment of the size distribution can be written as:

$$\int_0^\infty r^2 n(r)dr = \frac{3M_a}{4\pi\rho r_{eff}}, \quad \text{(S3)}$$

https://doi.org/10.5194/egusphere-2026-6615
Preprint. Discussion started: 10 November 2026
© Author(s) 2026. CC BY 4.0 License.

which leads to:

$$\beta_{ext} = \frac{3\overline{Q_{ext}}M_a}{4\rho r_{eff}}. \quad \text{(S4)}$$

This expression indicates that aerosol extinction is proportional to aerosol mass loading and extinction efficiency, but inversely proportional to effective radius (Hand and Malm, 2007).

For each aerosol species, the fine-mode (wet radius < 0.5 μm) and coarse-mode contributions can be expressed using mass fractions f_m and $(1 - f_m)$, effective radii r_f and r_c, and corresponding extinction efficiencies Q_f and Q_c. Assuming linear additivity of extinction coefficients under the independent scattering approximation, the fractional contribution of fine-mode extinction can be written as:

$$\frac{\beta_f}{\beta_{ext}} = \frac{f_m Q_f / r_f}{f_m Q_f / r_f + (1-f_m) Q_c / r_c}, \quad \text{(S5)}$$

where f_m is diagnosed by integrating the aerosol size distribution in PAMT. In addition, PAMT provides effective radius (ER) and effective variance (EV) for 5 extinction coefficients. Assuming a lognormal size distribution with prescribed geometric standard deviation ($\sigma_g = 2$), the geometric mean radius can be reconstructed from ER and EV. Combined with the prescribed size ranges (Table 1) and the 0.5 μm cutoff, the effective radii r_f and r_c for each extinction coefficient are diagnosed accordingly. The extinction efficiency $\overline{Q_{ext}}$ is estimated based on Mie theory and representative size regimes. For coarse-mode particles, $Q_c = 2$ is assumed. For internally mixed BC/OA/SO4 and externally mixed BC and OA, $Q_f = 1.8$ is used. For dust and sea salt, $Q_f = 1.7$ and $Q_f = 1.9$ are adopted, respectively. Finally, the vertically integrated fine-mode extinction yields AOD_f, while the remaining contribution is defined as AOD_c.

Code and data availability. The CIESM source code is publicly available at http://doi.org/10.5281/zenodo.3596317 (YishuangLiang and hxmhuang, 2020) , and documentation for the PAM can be accessed at https://gitlab.com/PAMdev/canam5.1-pam and described by https://cccma.gitlab.io/PAM/PAMcode.html. AeroCom3 data can be obtained from https://aerocom.met.no/tools/aeroval. AERONET data are available at https://aeronet.gsfc.nasa.gov/new_web/download_all_v3_aod.html, IMPROVE data can be downloaded from https://views.cira.colostate.edu/fed/, and EMEP data are accessible via https://www.emep.int/ and http://ebas-data.nilu.no/Default.aspx. ECCC/NAPS data can be obtained from https://open.canada.ca/data/en/dataset/1b36a356-defd-4813-acea-47bc3abd859b, SHIP data from https://www.pmel.noaa.gov/acg/, and MERGED-FMI data from https://nsdc.fmi.fi/data/data_aod. AATSR-SU data are available at https://catalogue.ceda.ac.uk/uuid/5dd3881e89c8419bbdba4ab06aa91112/, MERRA-2 data at https://gmao.gsfc.nasa.gov/reanalysis/MERRA-2, and MACC reanalysis data at https://www.ecmwf.int/en/forecasts/dataset/macc-reanalysis. Last accessed: 1 December, 2025.

https://doi.org/10.5194/egusphere-2026-6615
Preprint. Discussion started: 10 November 2026
© Author(s) 2026. CC BY 4.0 License.

Author contribution. MW completed the coupling of PAMT with CAM5.3 and performed aerosol evaluations, except for AeroCom3 and Arctic. Building on this foundation, HW coupled PAMT with CIESM, expanded the observational datasets, conducted the simulations and analyses, and drafted the manuscript. YP led the study and designed the experiments. KVS provided the PAM code and guided the model coupling and evaluation. JL generated the aerosol optical property lookup tables using Mie scattering. LFL contributed to the description of the PAMT scheme and helped refine the manuscript. HL and JQ provided guidance on the acquisition and use of satellite datasets. JX and XZ provided the CARE-China and CAWNET datasets, respectively, and contributed to the processing and application of these data. YP, KVS, HL, and JQ supervised the work and further refined the manuscript. All authors contributed to the final version of the paper.

Competing interests. The authors declare that they have no conflict of interest.

Acknowledgements. This work is supported by the National Key Research and Development Program of China (2024YFB3907900, 2024YFB3908300, 2024YFB390870101), the European Union Horizon Europe project “CleanCloud” (101137639), and the National Key Scientific and Technological Infrastructure project “Earth System Numerical Simulation Facility” (EarthLab).

Financial support. This work has been supported by the National Key Research and Development Program of China (grant no. 2024YFB3907900).

https://doi.org/10.5194/egusphere-2026-6615
Preprint. Discussion started: 10 November 2026
© Author(s) 2026. CC BY 4.0 License.

References

Abdul-Razzak, H. and Ghan, S. J.: A parameterization of aerosol activation: 2. Multiple aerosol types, Journal of Geophysical Research: Atmospheres, 105, 6837–6844, https://doi.org/10.1029/1999JD901161, 2000.

Albrecht, B. A.: Aerosols, Cloud Microphysics, and Fractional Cloudiness, Science (1979)., 245, 1227–1230, https://doi.org/10.1126/science.245.4923.1227, 1989.

AMAP: AMAP Assessment 2021: Impacts of Short-lived Climate Forcers on Arctic Climate, Air Quality, and Human Health, Arctic Monitoring and Assessment Programme (AMAP), x + 375pp p., https://www.amap.no/documents/doc/amap-assessment-2021-impacts-of-short-lived-climate-forcers-on-arctic-climate-air-quality-and-human-health/3614, 2021.

Asmi, A., Collaud Coen, M., Ogren, J. A., Andrews, E., Sheridan, P., Jefferson, A., Weingartner, E., Baltensperger, U., Bukowiecki, N., Lihavainen, H., Kivekäs, N., Asmi, E., Aalto, P. P., Kulmala, M., Wiedensohler, A., Birmili, W., Hamed, A., O'Dowd, C., G Jennings, S., Weller, R., Flentje, H., Fjaeraa, A. M., Fiebig, M., Myhre, C. L., Hallar, A. G., Swietlicki, E., Kristensson, A., and Laj, P.: Aerosol decadal trends – Part 2: In-situ aerosol particle number concentrations at GAW and ACTRIS stations, Atmos. Chem. Phys., 13, 895–916, https://doi.org/10.5194/acp-13-895-2013, 2013.

Bari, Md. A. and Kindzierski, W. B.: Characterization of air quality and sources of fine particulate matter (PM2.5) in the City of Calgary, Canada, Atmos. Pollut. Res., 9, 534–543, https://doi.org/10.1016/j.apr.2017.11.014, 2018.

Barth, M. C., Rasch, P. J., Kiehl, J. T., Benkovitz, C. M., and Schwartz, S. E.: Sulfur chemistry in the National Center for Atmospheric Research Community Climate Model: Description, evaluation, features, and sensitivity to aqueous chemistry, Journal of Geophysical Research: Atmospheres, 105, 1387–1415, https://doi.org/10.1029/1999JD900773, 2000.

Bellouin, N., Quaas, J., Gryspeerdt, E., Kinne, S., Stier, P., Watson-Parris, D., Boucher, O., Carslaw, K. S., Christensen, M., Daniau, A. -L., Dufresne, J. -L., Feingold, G., Fiedler, S., Forster, P., Gettelman, A., Haywood, J. M., Lohmann, U., Malavelle, F., Mauritsen, T., McCoy, D. T., Myhre, G., Mülmenstädt, J., Neubauer, D., Possner, A., Rugenstein, M., Sato, Y., Schulz, M., Schwartz, S. E., Sourdeval, O., Storelvmo, T., Toll, V., Winker, D., and Stevens, B.: Bounding Global Aerosol Radiative Forcing of Climate Change, Reviews of Geophysics, 58, https://doi.org/10.1029/2019RG000660, 2020.

Bevan, S. L., North, P. R. J., Los, S. O., and Grey, W. M. F.: A global dataset of atmospheric aerosol optical depth and surface reflectance from AATSR, Remote Sens. Environ., 116, 199–210, https://doi.org/10.1016/j.rse.2011.05.024, 2012.

Bigg, E. K.: The formation of atmospheric ice crystals by the freezing of droplets, Quarterly Journal of the Royal Meteorological Society, 79, 510–519, https://doi.org/10.1002/qj.49707934207, 1953.

Binkowski, F. S. and Roselle, S. J.: Models-3 Community Multiscale Air Quality (CMAQ) model aerosol component 1. Model description, Journal of Geophysical Research: Atmospheres, 108, https://doi.org/10.1029/2001JD001409, 2003.

Binkowski, F. S. and Shankar, U.: The Regional Particulate Matter Model: 1. Model description and preliminary results, Journal of Geophysical Research: Atmospheres, 100, 26191–26209, https://doi.org/10.1029/95JD02093, 1995.

https://doi.org/10.5194/egusphere-2026-6615
Preprint. Discussion started: 10 November 2026
© Author(s) 2026. CC BY 4.0 License.

Bodas-Salcedo, A., Webb, M. J., Bony, S., Chepfer, H., Dufresne, J.-L., Klein, S. A., Zhang, Y., Marchand, R., Haynes, J. M., Pincus, R., and John, V. O.: COSP: Satellite simulation software for model assessment, Bull. Am. Meteorol. Soc., 92, 1023–1043, https://doi.org/10.1175/2011BAMS2856.1, 2011.

Bogenschutz, P. A., Gettelman, A., Hannay, C., Larson, V. E., Neale, R. B., Craig, C., and Chen, C.-C.: The path to CAM6: coupled simulations with CAM5.4 and CAM5.5, Geosci. Model Dev., 11, 235–255, https://doi.org/10.5194/gmd-11-235-2018, 2018.

Bretherton, C. S. and Park, S.: A New Moist Turbulence Parameterization in the Community Atmosphere Model, J. Clim., 22, 3422–3448, https://doi.org/10.1175/2008JCLI2556.1, 2009.

Chin, M., Wright, J. S., Bian, H., Tan, Q., Pan, X., Takemura, T., Matsui, H., Tsigaridis, K., Bauer, S., Ginoux, P., Peng, Y., Guo, Z., Fadnavis, S., Laakso, A., Burrows, J. P., Taha, G., Kar, J., Rozanov, A., Arosio, C., Rieger, L., and Bourassa, A.: Variability and trends of upper-tropospheric aerosols over the Asian summer monsoon region: an AeroCom multi-model study, Atmos. Chem. Phys., 26, 6035–6059, https://doi.org/10.5194/ACP-26-6035-2026, 2026.

Cole, J. N. S., von Salzen, K., Li, J., Scinocca, J., Plummer, D., Arora, V., McFarlane, N., Lazare, M., MacKay, M., and Verseghy, D.: The Canadian Atmospheric Model version 5 (CanAM5.0.3), Geosci. Model Dev., 16, 5427–5448, https://doi.org/10.5194/gmd-16-5427-2023, 2023.

Croft, B., Lohmann, U., and von Salzen, K.: Black carbon ageing in the Canadian Centre for Climate modelling and analysis atmospheric general circulation model, Atmos. Chem. Phys., 5, 1931–1949, https://doi.org/10.5194/acp-5-1931-2005, 2005.

Croft, B., Lohmann, U., Martin, R. V., Stier, P., Wurzler, S., Feichter, J., Posselt, R., and Ferrachat, S.: Aerosol size-dependent below-cloud scavenging by rain and snow in the ECHAM5-HAM, Atmos. Chem. Phys., 9, 4653–4675, https://doi.org/10.5194/acp-9-4653-2009, 2009.

d'Almeida, G. A. , K. P. S. E. P.: Atmospheric aerosols : Global climatology and radiative characteristics, A. Deepak Pub., Hampton, VA, https://api.semanticscholar.org/CorpusID:127815484, 1991.

Danabasoglu, G., Lamarque, J. -F., Bacmeister, J., Bailey, D. A., DuVivier, A. K., Edwards, J., Emmons, L. K., Fasullo, J., Garcia, R., Gettelman, A., Hannay, C., Holland, M. M., Large, W. G., Lauritzen, P. H., Lawrence, D. M., Lenaerts, J. T. M., Lindsay, K., Lipscomb, W. H., Mills, M. J., Neale, R., Oleson, K. W., Otto-Bliesner, B., Phillips, A. S., Sacks, W., Tilmes, S., van Kampenhout, L., Vertenstein, M., Bertini, A., Dennis, J., Deser, C., Fischer, C., Fox-Kemper, B., Kay, J. E., Kinnison, D., Kushner, P. J., Larson, V. E., Long, M. C., Mickelson, S., Moore, J. K., Nienhouse, E., Polvani, L., Rasch, P. J., and Strand, W. G.: The Community Earth System Model Version 2 (CESM2), J. Adv. Model. Earth Syst., 12, e2019MS001916, https://doi.org/10.1029/2019MS001916, 2020.

D'Andrea, S. D., Häkkinen, S. A. K., Westervelt, D. M., Kuang, C., Levin, E. J. T., Kanawade, V. P., Leaitch, W. R., Spracklen, D. V., Riipinen, I., and Pierce, J. R.: Understanding global secondary organic aerosol amount and size-resolved condensational behavior, Atmos. Chem. Phys., 13, 11519–11534, https://doi.org/10.5194/acp-13-11519-2013, 2013.

Dentener, F., Kinne, S., Bond, T., Boucher, O., Cofala, J., Generoso, S., Ginoux, P., Gong, S., Hoelzemann, J. J., Ito, A., Marelli, L., Penner, J. E., Putaud, J.-P., Textor, C., Schulz, M., van der Werf, G. R., and Wilson, J.: Emissions of primary

https://doi.org/10.5194/egusphere-2026-6615
Preprint. Discussion started: 10 November 2026
© Author(s) 2026. CC BY 4.0 License.

aerosol and precursor gases in the years 2000 and 1750 prescribed data-sets for AeroCom, Atmos. Chem. Phys., 6, 4321–4344, https://doi.org/10.5194/acp-6-4321-2006, 2006.

Digby, R. A. R., von Salzen, K., Monahan, A. H., Gillett, N. P., and Li, J.: The impact of uncertainty in black carbon's refractive index on simulated optical depth and radiative forcing, Atmos. Chem. Phys., 25, 3109–3130, https://doi.org/10.5194/acp-25-3109-2025, 2025.

Dunne, E. M., Gordon, H., Kürten, A., Almeida, J., Duplissy, J., Williamson, C., Ortega, I. K., Pringle, K. J., Adamov, A., Baltensperger, U., Barmet, P., Benduhn, F., Bianchi, F., Breitenlechner, M., Clarke, A., Curtius, J., Dommen, J., Donahue, N. M., Ehrhart, S., Flagan, R. C., Franchin, A., Guida, R., Hakala, J., Hansel, A., Heinritzi, M., Jokinen, T., Kangasluoma, J., Kirkby, J., Kulmala, M., Kupc, A., Lawler, M. J., Lehtipalo, K., Makhmutov, V., Mann, G., Mathot, S., Merikanto, J., Miettinen, P., Nenes, A., Onnela, A., Rap, A., Reddington, C. L. S., Riccobono, F., Richards, N. A. D., Rissanen, M. P., Rondo, L., Sarnela, N., Schobesberger, S., Sengupta, K., Simon, M., Sipilä, M., Smith, J. N., Stozkhov, Y., Tomé, A., Tröstl, J., Wagner, P. E., Wimmer, D., Winkler, P. M., Worsnop, D. R., and Carslaw, K. S.: Global atmospheric particle formation from CERN CLOUD measurements, Science (1979)., 354, 1119–1124, https://doi.org/10.1126/science.aaf2649, 2016.

Easter, R. C., Ghan, S. J., Zhang, Y., Saylor, R. D., Chapman, E. G., Laulainen, N. S., Abdul-Razzak, H., Leung, L. R., Bian, X., and Zaveri, R. A.: MIRAGE: Model description and evaluation of aerosols and trace gases, Journal of Geophysical Research: Atmospheres, 109, 20210, https://doi.org/10.1029/2004JD004571, 2004.

Emerson, E. W., Hodshire, A. L., DeBolt, H. M., Bilsback, K. R., Pierce, J. R., McMeeking, G. R., and Farmer, D. K.: Revisiting particle dry deposition and its role in radiative effect estimates, Proceedings of the National Academy of Sciences, 117, 26076–26082, https://doi.org/10.1073/pnas.2014761117, 2020.

Emmons, L. K., Walters, S., Hess, P. G., Lamarque, J.-F., Pfister, G. G., Fillmore, D., Granier, C., Guenther, A., Kinnison, D., Laepple, T., Orlando, J., Tie, X., Tyndall, G., Wiedinmyer, C., Baughcum, S. L., and Kloster, S.: Description and evaluation of the Model for Ozone and Related chemical Tracers, version 4 (MOZART-4), Geosci. Model Dev., 3, 43–67, https://doi.org/10.5194/gmd-3-43-2010, 2010.

Eyring, V., Bony, S., Meehl, G. A., Senior, C. A., Stevens, B., Stouffer, R. J., and Taylor, K. E.: Overview of the Coupled Model Intercomparison Project Phase 6 (CMIP6) experimental design and organization, Geosci. Model Dev., 9, 1937–1958, https://doi.org/10.5194/gmd-9-1937-2016, 2016.

Gelaro, R., McCarty, W., Suárez, M. J., Todling, R., Molod, A., Takacs, L., Randles, C. A., Darmenov, A., Bosilovich, M. G., Reichle, R., Wargan, K., Coy, L., Cullather, R., Draper, C., Akella, S., Buchard, V., Conaty, A., da Silva, A. M., Gu, W., Kim, G.-K., Koster, R., Lucchesi, R., Merkova, D., Nielsen, J. E., Partyka, G., Pawson, S., Putman, W., Rienecker, M., Schubert, S. D., Sienkiewicz, M., and Zhao, B.: The Modern-Era Retrospective Analysis for Research and Applications, Version 2 (MERRA-2), J. Clim., 30, 5419–5454, https://doi.org/10.1175/JCLI-D-16-0758.1, 2017.

Gettelman, A., Liu, X., Barahona, D., Lohmann, U., and Chen, C.: Climate impacts of ice nucleation, Journal of Geophysical Research: Atmospheres, 117, https://doi.org/10.1029/2012JD017950, 2012.

https://doi.org/10.5194/egusphere-2026-6615
Preprint. Discussion started: 10 November 2026
© Author(s) 2026. CC BY 4.0 License.

Ghan, S. J. and Easter, R. C.: Impact of cloud-borne aerosol representation on aerosol direct and indirect effects, Atmos. Chem. Phys., 6, 4163–4174, https://doi.org/10.5194/acp-6-4163-2006, 2006.

Ghan, S. J. and Zaveri, R. A.: Parameterization of optical properties for hydrated internally mixed aerosol, Journal of Geophysical Research: Atmospheres, 112, https://doi.org/10.1029/2006JD007927, 2007.

Ghan, S. J., Liu, X., Easter, R. C., Zaveri, R., Rasch, P. J., Yoon, J.-H., and Eaton, B.: Toward a Minimal Representation of Aerosols in Climate Models: Comparative Decomposition of Aerosol Direct, Semidirect, and Indirect Radiative Forcing, J. Clim., 25, 6461–6476, https://doi.org/10.1175/JCLI-D-11-00650.1, 2012.

Gliß, J., Mortier, A., Schulz, M., Andrews, E., Balkanski, Y., Bauer, S. E., Benedictow, A. M. K., Bian, H., Checa-Garcia, R., Chin, M., Ginoux, P., Griesfeller, J. J., Heckel, A., Kipling, Z., Kirkevåg, A., Kokkola, H., Laj, P., Le Sager, P., Lund, M. T., Lund Myhre, C., Matsui, H., Myhre, G., Neubauer, D., van Noije, T., North, P., Olivié, D. J. L., Rémy, S., Sogacheva, L., Takemura, T., Tsigaridis, K., and Tsyro, S. G.: AeroCom phase III multi-model evaluation of the aerosol life cycle and optical properties using ground- and space-based remote sensing as well as surface in situ observations, Atmos. Chem. Phys., 21, 87–128, https://doi.org/10.5194/acp-21-87-2021, 2021.

Glotfelty, T., He, J., and Zhang, Y.: Improving organic aerosol treatments in CESM/CAM5: Development, application, and evaluation, J. Adv. Model. Earth Syst., 9, 1506–1539, https://doi.org/10.1002/2016MS000874, 2017.

Guo, Z., Wang, M., Peng, Y., and Luo, Y.: Evaluation on the Vertical Distribution of Liquid and Ice Phase Cloud Fraction in Community Atmosphere Model Version 5.3 using Spaceborne Lidar Observations, Earth and Space Science, 7, https://doi.org/10.1029/2019EA001029, 2020.

Hand, J. L. and Malm, W. C.: Review of aerosol mass scattering efficiencies from ground-based measurements since 1990, Journal of Geophysical Research: Atmospheres, 112, https://doi.org/10.1029/2007JD008484, 2007.

Hanson, D. R.: Mass Accommodation of H2SO4 and CH3SO3H on Water−Sulfuric Acid Solutions from 6% to 97% RH, J. Phys. Chem. A, 109, 6919–6927, https://doi.org/10.1021/jp0510443, 2005.

Hersbach, H., Bell, B., Berrisford, P., Hirahara, S., Horányi, A., Muñoz-Sabater, J., Nicolas, J., Peubey, C., Radu, R., Schepers, D., Simmons, A., Soci, C., Abdalla, S., Abellan, X., Balsamo, G., Bechtold, P., Biavati, G., Bidlot, J., Bonavita, M., De Chiara, G., Dahlgren, P., Dee, D., Diamantakis, M., Dragani, R., Flemming, J., Forbes, R., Fuentes, M., Geer, A., Haimberger, L., Healy, S., Hogan, R. J., Hólm, E., Janisková, M., Keeley, S., Laloyaux, P., Lopez, P., Lupu, C., Radnoti, G., de Rosnay, P., Rozum, I., Vamborg, F., Villaume, S., and Thépaut, J.: The ERA5 global reanalysis, Quarterly Journal of the Royal Meteorological Society, 146, 1999–2049, https://doi.org/10.1002/qj.3803, 2020.

Hoesly, R. M., Smith, S. J., Feng, L., Klimont, Z., Janssens-Maenhout, G., Pitkanen, T., Seibert, J. J., Vu, L., Andres, R. J., Bolt, R. M., Bond, T. C., Dawidowski, L., Kholod, N., Kurokawa, J., Li, M., Liu, L., Lu, Z., Moura, M. C. P., O'Rourke, P. R., and Zhang, Q.: Historical (1750–2014) anthropogenic emissions of reactive gases and aerosols from the Community Emissions Data System (CEDS), Geosci. Model Dev., 11, 369–408, https://doi.org/10.5194/gmd-11-369-2018, 2018.

https://doi.org/10.5194/egusphere-2026-6615
Preprint. Discussion started: 10 November 2026
© Author(s) 2026. CC BY 4.0 License.

Holben, B. N., Eck, T. F., Slutsker, I., Tanré, D., Buis, J. P., Setzer, A., Vermote, E., Reagan, J. A., Kaufman, Y. J., Nakajima, T., Lavenu, F., Jankowiak, I., and Smirnov, A.: AERONET—A Federated Instrument Network and Data Archive for Aerosol Characterization, Remote Sens. Environ., 66, 1–16, https://doi.org/10.1016/S0034-4257(98)00031-5, 1998.

Holben, B. N., Kim, J., Sano, I., Mukai, S., Eck, T. F., Giles, D. M., Schafer, J. S., Sinyuk, A., Slutsker, I., Smirnov, A., Sorokin, M., Anderson, B. E., Che, H., Choi, M., Crawford, J. H., Ferrare, R. A., Garay, M. J., Jeong, U., Kim, M., Kim, W., Knox, N., Li, Z., Lim, H. S., Liu, Y., Maring, H., Nakata, M., Pickering, K. E., Piketh, S., Redemann, J., Reid, J. S., Salinas, S., Seo, S., Tan, F., Tripathi, S. N., Toon, O. B., and Xiao, Q.: An overview of mesoscale aerosol processes, comparisons, and validation studies from DRAGON networks, Atmos. Chem. Phys., 18, 655–671, https://doi.org/10.5194/acp-18-655-2018, 2018.

Hourdin, F., Mauritsen, T., Gettelman, A., Golaz, J.-C., Balaji, V., Duan, Q., Folini, D., Ji, D., Klocke, D., Qian, Y., Rauser, F., Rio, C., Tomassini, L., Watanabe, M., and Williamson, D.: The Art and Science of Climate Model Tuning, Bull. Am. Meteorol. Soc., 98, 589–602, https://doi.org/10.1175/BAMS-D-15-00135.1, 2017.

Huang, X., Tang, Q., Tseng, Y., Hu, Y., Baker, A. H., Bryan, F. O., Dennis, J., Fu, H., and Yang, G.: P-CSI v1.0, an accelerated barotropic solver for the high-resolution ocean model component in the Community Earth System Model v2.0, Geosci. Model Dev., 9, 4209–4225, https://doi.org/10.5194/gmd-9-4209-2016, 2016.

Hurrell, J. W., Holland, M. M., Gent, P. R., Ghan, S., Kay, J. E., Kushner, P. J., Lamarque, J.-F., Large, W. G., Lawrence, D., Lindsay, K., Lipscomb, W. H., Long, M. C., Mahowald, N., Marsh, D. R., Neale, R. B., Rasch, P., Vavrus, S., Vertenstein, M., Bader, D., Collins, W. D., Hack, J. J., Kiehl, J., and Marshall, S.: The Community Earth System Model: A Framework for Collaborative Research, Bull. Am. Meteorol. Soc., 94, 1339–1360, https://doi.org/10.1175/BAMS-D-12-00121.1, 2013.

Hyslop, N. and White, W.: An evaluation of interagency monitoring of protected visual environments (IMPROVE) collocated precision and uncertainty estimates, Atmos. Environ., 42, 2691–2705, https://doi.org/10.1016/j.atmosenv.2007.06.053, 2008.

Iacono, M. J., Delamere, J. S., Mlawer, E. J., Shephard, M. W., Clough, S. A., and Collins, W. D.: Radiative forcing by long-lived greenhouse gases: Calculations with the AER radiative transfer models, Journal of Geophysical Research: Atmospheres, 113, 13103, https://doi.org/10.1029/2008JD009944, 2008.

Inness, A., Baier, F., Benedetti, A., Bouarar, I., Chabrillat, S., Clark, H., Clerbaux, C., Coheur, P., Engelen, R. J., Errera, Q., Flemming, J., George, M., Granier, C., Hadji-Lazaro, J., Huijnen, V., Hurtmans, D., Jones, L., Kaiser, J. W., Kapsomenakis, J., Lefever, K., Leitão, J., Razinger, M., Richter, A., Schultz, M. G., Simmons, A. J., Suttie, M., Stein, O., Thépaut, J.-N., Thouret, V., Vrekoussis, M., and Zerefos, C.: The MACC reanalysis: an 8 yr data set of atmospheric composition, Atmos. Chem. Phys., 13, 4073–4109, https://doi.org/10.5194/acp-13-4073-2013, 2013.

IPCC: The Earth's Energy Budget, Climate Feedbacks and Climate Sensitivity, in: Climate Change 2021 – The Physical Science Basis, Cambridge University Press, 923–1054, https://doi.org/10.1017/9781009157896.009, 2023.

Jia, H. and Quaas, J.: Nonlinearity of the cloud response postpones climate penalty of mitigating air pollution in polluted regions, Nat. Clim. Chang., 13, 943–950, https://doi.org/10.1038/s41558-023-01775-5, 2023.

https://doi.org/10.5194/egusphere-2026-6615
Preprint. Discussion started: 10 November 2026
© Author(s) 2026. CC BY 4.0 License.

Jin, Z., Qiao, Y., Wang, Y., Fang, Y., and Yi, W.: A new parameterization of spectral and broadband ocean surface albedo, Opt. Express, 19, 26429, https://doi.org/10.1364/OE.19.026429, 2011.

Ke, Z., Liu, X., Wu, M., Shan, Y., and Shi, Y.: Improved Dust Representation and Impacts on Dust Transport and Radiative Effect in CAM5, J. Adv. Model. Earth Syst., 14, e2021MS002845, https://doi.org/10.1029/2021MS002845, 2022.

Köhler, H.: The nucleus in and the growth of hygroscopic droplets, Trans. Faraday Soc., 32, 1152–1161, https://doi.org/10.1039/TF9363201152, 1936.

Kooperman, G. J., Pritchard, M. S., Ghan, S. J., Wang, M., Somerville, R. C. J., and Russell, L. M.: Constraining the influence of natural variability to improve estimates of global aerosol indirect effects in a nudged version of the Community Atmosphere Model 5, Journal of Geophysical Research: Atmospheres, 117, https://doi.org/10.1029/2012JD018588, 2012.

Kulmala, M., Laaksonen, A., and Pirjola, L.: Parameterizations for sulfuric acid/water nucleation rates, Journal of Geophysical Research: Atmospheres, 103, 8301–8307, https://doi.org/10.1029/97JD03718, 1998.

Lewis, R. and Schwartz, E.: Sea Salt Aerosol Production: Mechanisms, Methods, Measurements and Models—A Critical Review, American Geophysical Union, Washington, D. C., https://doi.org/10.1029/GM152, 2004.

Li, J., Wong, J. G. D., Dobbie, J. S., and Chýlek, P.: Parameterization of the Optical Properties of Sulfate Aerosols, J. Atmos. Sci., 58, 193–209, https://doi.org/10.1175/1520-0469(2001)058<0193:POTOPO>2.0.CO;2, 2001.

Li, J., Ma, X., von Salzen, K., and Dobbie, S.: Parameterization of sea-salt optical properties and physics of the associated radiative forcing, Atmos. Chem. Phys., 8, 4787–4798, https://doi.org/10.5194/acp-8-4787-2008, 2008.

Liang, Y., Wang, L., Zhang, G. J., and Wu, Q.: Sensitivity test of parameterizations of subgrid-scale orographic form drag in the NCAR CESM1, Clim. Dyn., 48, 3365–3379, https://doi.org/10.1007/s00382-016-3272-7, 2017.

Lin, S. and Rood, R. B.: An explicit flux-form semi-lagrangian shallow-water model on the sphere, Quarterly Journal of the Royal Meteorological Society, 123, 2477–2498, https://doi.org/10.1002/qj.49712354416, 1997.

Lin, S.-J. and Rood, R. B.: Multidimensional Flux-Form Semi-Lagrangian Transport Schemes, Mon. Weather Rev., 124, 2046–2070, https://doi.org/10.1175/1520-0493(1996)124<2046:MFFSLT>2.0.CO;2, 1996.

Lin, Y., Huang, X., Liang, Y., Qin, Y., Xu, S., Huang, W., Xu, F., Liu, L., Wang, Y., Peng, Y., Wang, L., Xue, W., Fu, H., Zhang, G. J., Wang, B., Li, R., Zhang, C., Lu, H., Yang, K., Luo, Y., Bai, Y., Song, Z., Wang, M., Zhao, W., Zhang, F., Xu, J., Zhao, X., Lu, C., Chen, Y., Luo, Y., Hu, Y., Tang, Q., Chen, D., Yang, G., and Gong, P.: Community Integrated Earth System Model (CIESM): Description and Evaluation, J. Adv. Model. Earth Syst., 12, https://doi.org/10.1029/2019MS002036, 2020.

Liu, L., Zhang, C., Li, R., Wang, B., and Yang, G.: C-Coupler2: a flexible and user-friendly community coupler for model coupling and nesting, Geosci. Model Dev., 11, 3557–3586, https://doi.org/10.5194/gmd-11-3557-2018, 2018.

Liu, X. and Penner, J. E.: Ice nucleation parameterization for global models, Meteorologische Zeitschrift, 14, 499–514, https://doi.org/10.1127/0941-2948/2005/0059, 2005.

Liu, X., Penner, J. E., Ghan, S. J., and Wang, M.: Inclusion of Ice Microphysics in the NCAR Community Atmospheric Model Version 3 (CAM3), J. Clim., 20, 4526–4547, https://doi.org/10.1175/JCLI4264.1, 2007.

https://doi.org/10.5194/egusphere-2026-6615
Preprint. Discussion started: 10 November 2026
© Author(s) 2026. CC BY 4.0 License.

Liu, X., Easter, R. C., Ghan, S. J., Zaveri, R., Rasch, P., Shi, X., Lamarque, J.-F., Gettelman, A., Morrison, H., Vitt, F., Conley, A., Park, S., Neale, R., Hannay, C., Ekman, A. M. L., Hess, P., Mahowald, N., Collins, W., Iacono, M. J., Bretherton, C. S., Flanner, M. G., and Mitchell, D.: Toward a minimal representation of aerosols in climate models: description and evaluation in the Community Atmosphere Model CAM5, Geosci. Model Dev., 5, 709–739, https://doi.org/10.5194/gmd-5-709-2012, 2012.

Liu, X., Ma, P.-L., Wang, H., Tilmes, S., Singh, B., Easter, R. C., Ghan, S. J., and Rasch, P. J.: Description and evaluation of a new four-mode version of the Modal Aerosol Module (MAM4) within version 5.3 of the Community Atmosphere Model, Geosci. Model Dev., 9, 505–522, https://doi.org/10.5194/gmd-9-505-2016, 2016.

Lüpkes, C., Gryanik, V. M., Hartmann, J., and Andreas, E. L.: A parametrization, based on sea ice morphology, of the neutral atmospheric drag coefficients for weather prediction and climate models, Journal of Geophysical Research: Atmospheres, 117, 13112, https://doi.org/10.1029/2012JD017630, 2012.

Ma, X., von Salzen, K., and Li, J.: Modelling sea salt aerosol and its direct and indirect effects on climate, Atmos. Chem. Phys., 8, 1311–1327, https://doi.org/10.5194/acp-8-1311-2008, 2008.

Mahmood, R., von Salzen, K., Flanner, M., Sand, M., Langner, J., Wang, H., and Huang, L.: Seasonality of global and Arctic black carbon processes in the Arctic Monitoring and Assessment Programme models, Journal of Geophysical Research: Atmospheres, 121, 7100–7116, https://doi.org/10.1002/2016JD024849, 2016.

Mahowald, N. M., Muhs, D. R., Levis, S., Rasch, P. J., Yoshioka, M., Zender, C. S., and Luo, C.: Change in atmospheric mineral aerosols in response to climate: Last glacial period, preindustrial, modern, and doubled carbon dioxide climates, Journal of Geophysical Research: Atmospheres, 111, https://doi.org/10.1029/2005JD006653, 2006a.

Mahowald, N. M., Yoshioka, M., Collins, W. D., Conley, A. J., Fillmore, D. W., and Coleman, D. B.: Climate response and radiative forcing from mineral aerosols during the last glacial maximum, pre-industrial, current and doubled-carbon dioxide climates, Geophys. Res. Lett., 33, https://doi.org/10.1029/2006GL026126, 2006b.

Mann, G. W., Carslaw, K. S., Reddington, C. L., Pringle, K. J., Schulz, M., Asmi, A., Spracklen, D. V., Ridley, D. A., Woodhouse, M. T., Lee, L. A., Zhang, K., Ghan, S. J., Easter, R. C., Liu, X., Stier, P., Lee, Y. H., Adams, P. J., Tost, H., Lelieveld, J., Bauer, S. E., Tsigaridis, K., van Noije, T. P. C., Strunk, A., Vignati, E., Bellouin, N., Dalvi, M., Johnson, C. E., Bergman, T., Kokkola, H., von Salzen, K., Yu, F., Luo, G., Petzold, A., Heintzenberg, J., Clarke, A., Ogren, J. A., Gras, J., Baltensperger, U., Kaminski, U., Jennings, S. G., O'Dowd, C. D., Harrison, R. M., Beddows, D. C. S., Kulmala, M., Viisanen, Y., Ulevicius, V., Mihalopoulos, N., Zdimal, V., Fiebig, M., Hansson, H.-C., Swietlicki, E., and Henzing, J. S.: Intercomparison and evaluation of global aerosol microphysical properties among AeroCom models of a range of complexity, Atmos. Chem. Phys., 14, 4679–4713, https://doi.org/10.5194/acp-14-4679-2014, 2014.

Mårtensson, E. M., Nilsson, E. D., de Leeuw, G., Cohen, L. H., and Hansson, H. -C.: Laboratory simulations and parameterization of the primary marine aerosol production, Journal of Geophysical Research: Atmospheres, 108, n/a-n/a, https://doi.org/10.1029/2002JD002263, 2003.

https://doi.org/10.5194/egusphere-2026-6615
Preprint. Discussion started: 10 November 2026
© Author(s) 2026. CC BY 4.0 License.

Marticorena, B. and Bergametti, G.: Modeling the atmospheric dust cycle: 1. Design of a soil-derived dust emission scheme, Journal of Geophysical Research: Atmospheres, 100, 16415–16430, https://doi.org/10.1029/95JD00690, 1995.

Maxwell Garnett, J. C.: Colours in metal glasses, in metallic films and in metallic solutions.—II, Proceedings of the Royal Society of London. Series A, Containing Papers of a Mathematical and Physical Character, 76, 370–373, https://doi.org/10.1098/rspa.1905.0039, 1905.

McComiskey, A. and Ferrare, R. A.: Aerosol Physical and Optical Properties and Processes in the ARM Program, Meteorological Monographs, 57, 21.1-21.17, https://doi.org/10.1175/AMSMONOGRAPHS-D-15-0028.1, 2016.

Meinig, C., Burger, E. F., Cohen, N., Cokelet, E. D., Cronin, M. F., Cross, J. N., de Halleux, S., Jenkins, R., Jessup, A. T., Mordy, C. W., Lawrence-Slavas, N., Sutton, A. J., Zhang, D., and Zhang, C.: Public–Private Partnerships to Advance Regional Ocean-Observing Capabilities: A Saildrone and NOAA-PMEL Case Study and Future Considerations to Expand to Global Scale Observing, Front. Mar. Sci., 6, https://doi.org/10.3389/fmars.2019.00448, 2019.

Merikanto, J., Napari, I., Vehkamäki, H., Anttila, T., and Kulmala, M.: New parameterization of sulfuric acid-ammonia-water ternary nucleation rates at tropospheric conditions, Journal of Geophysical Research: Atmospheres, 112, 15207, https://doi.org/10.1029/2006JD007977, 2007.

Meyers, M. P., DeMott, P. J., and Cotton, W. R.: New Primary Ice-Nucleation Parameterizations in an Explicit Cloud Model, Journal of Applied Meteorology, 31, 708–721, https://doi.org/10.1175/1520-0450(1992)031<0708:NPINPI>2.0.CO;2, 1992.

Mlawer, E. J., Taubman, S. J., Brown, P. D., Iacono, M. J., and Clough, S. A.: Radiative transfer for inhomogeneous atmospheres: RRTM, a validated correlated-k model for the longwave, Journal of Geophysical Research: Atmospheres, 102, 16663–16682, https://doi.org/10.1029/97JD00237, 1997.

Monahan, E. C., Spiel, D. E., and Davidson, K. L.: A Model of Marine Aerosol Generation Via Whitecaps and Wave Disruption, American Meteorological Soc, 167–174, https://doi.org/10.1007/978-94-009-4668-2_16, 1986.

Morrison, H. and Gettelman, A.: A New Two-Moment Bulk Stratiform Cloud Microphysics Scheme in the Community Atmosphere Model, Version 3 (CAM3). Part I: Description and Numerical Tests, J. Clim., 21, 3642–3659, https://doi.org/10.1175/2008JCLI2105.1, 2008.

Neale, R. B., Gettelman, A., Park, S., Chen, C.-C., Lauritzen, P. H., Williamson, D. L., Conley, A. J., Kinnison, D., Marsh, D., Smith, A. K., Vitt, F. M., Garcia, R., Lamarque, J.-F., Mills, M. J., Tilmes, S., Morrison, H., Cameron-Smith, P., Collins, W. D., Iacono, M. J., Easter, R. C., Liu, X., Ghan, S. J., Rasch, P. J., and Taylor, M. A.: Description of the NCAR Community Atmosphere Model (CAM 5.0), https://doi.org/10.5065/WGTK-4G06, 2012.

Neubauer, D., Ferrachat, S., Siegenthaler-Le Drian, C., Stier, P., Partridge, D. G., Tegen, I., Bey, I., Stanelle, T., Kokkola, H., and Lohmann, U.: The global aerosol–climate model ECHAM6.3–HAM2.3 – Part 2: Cloud evaluation, aerosol radiative forcing, and climate sensitivity, Geosci. Model Dev., 12, 3609–3639, https://doi.org/10.5194/gmd-12-3609-2019, 2019.

Okin, G. S.: A new model of wind erosion in the presence of vegetation, J. Geophys. Res. Earth Surf., 113, 2–10, https://doi.org/10.1029/2007JF000758, 2008.

https://doi.org/10.5194/egusphere-2026-6615
Preprint. Discussion started: 10 November 2026
© Author(s) 2026. CC BY 4.0 License.

Pandis, S. N., Seinfeld, J. H., and Pilinis, C.: Chemical composition differences in fog and cloud droplets of different sizes, Atmospheric Environment. Part A. General Topics, 24, 1957–1969, https://doi.org/10.1016/0960-1686(90)90529-V, 1990.

Park, S. and Bretherton, C. S.: The University of Washington Shallow Convection and Moist Turbulence Schemes and Their Impact on Climate Simulations with the Community Atmosphere Model, J. Clim., 22, 3449–3469, https://doi.org/10.1175/2008JCLI2557.1, 2009.

Peng, Y., von Salzen, K., and Li, J.: Simulation of mineral dust aerosol with Piecewise Log-normal Approximation (PLA) in CanAM4-PAM, Atmos. Chem. Phys., 12, 6891–6914, https://doi.org/10.5194/acp-12-6891-2012, 2012.

Peters, D. M., Grainger, R. G., and Thomas, G.: Aerosol optical properties, in: DLR Forschungsberichte, 222–226, 2010.

Petters, M. D. and Kreidenweis, S. M.: A single parameter representation of hygroscopic growth and cloud condensation nucleus activity, Atmos. Chem. Phys., 7, 1961–1971, https://doi.org/10.5194/acp-7-1961-2007, 2007.

Platnick, S., King, M. D., Ackerman, S. A., Menzel, W. P., Baum, B. A., Riedi, J. C., and Frey, R. A.: The MODIS cloud products: algorithms and examples from terra, IEEE Transactions on Geoscience and Remote Sensing, 41, 459–473, https://doi.org/10.1109/TGRS.2002.808301, 2003.

Pöschl, U., Canagaratna, M., Jayne, J. T., Molina, L. T., Worsnop, D. R., Kolb, C. E., and Molina, M. J.: Mass Accommodation Coefficient of H2SO4 Vapor on Aqueous Sulfuric Acid Surfaces and Gaseous Diffusion Coefficient of H2SO4 in N2/H2O, J. Phys. Chem. A, 102, 10082–10089, https://doi.org/10.1021/jp982809s, 1998.

Qin, Y., Lin, Y., Xu, S., Ma, H., and Xie, S.: A Diagnostic PDF Cloud Scheme to Improve Subtropical Low Clouds in NCAR Community Atmosphere Model (CAM5), J. Adv. Model. Earth Syst., 10, 320–341, https://doi.org/10.1002/2017MS001095, 2018.

Quaas, J., Andrews, T., Bellouin, N., Block, K., Boucher, O., Ceppi, P., Dagan, G., Doktorowski, S., Eichholz, H. M., Forster, P., Goren, T., Gryspeerdt, E., Hodnebrog, Ø., Jia, H., Kramer, R., Lange, C., Maycock, A. C., Mülmenstädt, J., Myhre, G., O'Connor, F. M., Pincus, R., Samset, B. H., Senf, F., Shine, K. P., Smith, C., Stjern, C. W., Takemura, T., Toll, V., and Wall, C. J.: Adjustments to Climate Perturbations—Mechanisms, Implications, Observational Constraints, AGU Advances, 5, https://doi.org/10.1029/2023AV001144, 2024.

Rasch, P. J., Barth, M. C., Kiehl, J. T., Schwartz, S. E., and Benkovitz, C. M.: A description of the global sulfur cycle and its controlling processes in the National Center for Atmospheric Research Community Climate Model, Version 3, Journal of Geophysical Research: Atmospheres, 105, 1367–1385, https://doi.org/10.1029/1999JD900777, 2000.

Rosenfeld, D., Kokhanovsky, A., Goren, T., Gryspeerdt, E., Hasekamp, O., Jia, H., Lopatin, A., Quaas, J., Pan, Z., and Sourdeval, O.: Frontiers in Satellite-Based Estimates of Cloud-Mediated Aerosol Forcing, Reviews of Geophysics, 61, https://doi.org/10.1029/2022RG000799, 2023.

Russell, L. M., Pandis, S. N., and Seinfeld, J. H.: Aerosol production and growth in the marine boundary layer, Journal of Geophysical Research: Atmospheres, 99, 20989–21003, https://doi.org/10.1029/94JD01932, 1994.

Salzmann, M., Ferrachat, S., Tully, C., Münch, S., Watson-Parris, D., Neubauer, D., Siegenthaler-Le Drian, C., Rast, S., Heinold, B., Crueger, T., Brokopf, R., Mülmenstädt, J., Quaas, J., Wan, H., Zhang, K., Lohmann, U., Stier, P., and Tegen, I.:

https://doi.org/10.5194/egusphere-2026-6615
Preprint. Discussion started: 10 November 2026
© Author(s) 2026. CC BY 4.0 License.

The Global Atmosphere-aerosol Model ICON-A-HAM2.3–Initial Model Evaluation and Effects of Radiation Balance Tuning on Aerosol Optical Thickness, J. Adv. Model. Earth Syst., 14, e2021MS002699, https://doi.org/10.1029/2021MS002699, 2022.

Schuster, G. L., Dubovik, O., and Holben, B. N.: Angstrom exponent and bimodal aerosol size distributions, Journal of Geophysical Research: Atmospheres, 111, https://doi.org/10.1029/2005JD006328, 2006.

Scott, B. C.: Parameterization of Sulfate Removal by Precipitation, Journal of Applied Meteorology, 17, 1375–1389, https://doi.org/10.1175/1520-0450(1978)017<1375:POSRBP>2.0.CO;2, 1978.

Seinfeld, J. H. and Pandis, S. N.: Atmospheric Chemistry and Physics：From Air Pollution to Climate Change, 2nd edition., John Wiley & Sons Inc, 2006.

Shangguan, W., Dai, Y., Duan, Q., Liu, B., and Yuan, H.: A global soil data set for earth system modeling, J. Adv. Model. Earth Syst., 6, 249–263, https://doi.org/10.1002/2013MS000293, 2014.

Shi, X., Liu, X., and Zhang, K.: Effects of pre-existing ice crystals on cirrus clouds and comparison between different ice nucleation parameterizations with the Community Atmosphere Model (CAM5), Atmos. Chem. Phys., 15, 1503–1520, https://doi.org/10.5194/acp-15-1503-2015, 2015.

Sogacheva, L., Popp, T., Sayer, A. M., Dubovik, O., Garay, M. J., Heckel, A., Hsu, N. C., Jethva, H., Kahn, R. A., Kolmonen, P., Kosmale, M., de Leeuw, G., Levy, R. C., Litvinov, P., Lyapustin, A., North, P., Torres, O., and Arola, A.: Merging regional and global aerosol optical depth records from major available satellite products, Atmos. Chem. Phys., 20, 2031–2056, https://doi.org/10.5194/acp-20-2031-2020, 2020.

Song, X. and Zhang, G. J.: Microphysics parameterization for convective clouds in a global climate model: Description and single-column model tests, J. Geophys. Res., 116, D02201, https://doi.org/10.1029/2010JD014833, 2011.

Stevens, B., Fiedler, S., Kinne, S., Peters, K., Rast, S., Müsse, J., Smith, S. J., and Mauritsen, T.: MACv2-SP: a parameterization of anthropogenic aerosol optical properties and an associated Twomey effect for use in CMIP6, Geosci. Model Dev., 10, 433–452, https://doi.org/10.5194/gmd-10-433-2017, 2017.

Tegen, I., Neubauer, D., Ferrachat, S., Siegenthaler-Le Drian, C., Bey, I., Schutgens, N., Stier, P., Watson-Parris, D., Stanelle, T., Schmidt, H., Rast, S., Kokkola, H., Schultz, M., Schroeder, S., Daskalakis, N., Barthel, S., Heinold, B., and Lohmann, U.: The global aerosol–climate model ECHAM6.3–HAM2.3 – Part 1: Aerosol evaluation, Geosci. Model Dev., 12, 1643–1677, https://doi.org/10.5194/gmd-12-1643-2019, 2019.

Tie, X., Brasseur, G., Emmons, L., Horowitz, L., and Kinnison, D.: Effects of aerosols on tropospheric oxidants: A global model study, Journal of Geophysical Research: Atmospheres, 106, 22931–22964, https://doi.org/10.1029/2001JD900206, 2001.

Tørseth, K., Aas, W., Breivik, K., Fjæraa, A. M., Fiebig, M., Hjellbrekke, A. G., Lund Myhre, C., Solberg, S., and Yttri, K. E.: Introduction to the European Monitoring and Evaluation Programme (EMEP) and observed atmospheric composition change during 1972–2009, Atmos. Chem. Phys., 12, 5447–5481, https://doi.org/10.5194/acp-12-5447-2012, 2012.

https://doi.org/10.5194/egusphere-2026-6615
Preprint. Discussion started: 10 November 2026
© Author(s) 2026. CC BY 4.0 License.

Twomey, S.: The Influence of Pollution on the Shortwave Albedo of Clouds, J. Atmos. Sci., 34, 1149–1152, https://doi.org/10.1175/1520-0469(1977)034<1149:TIOPOT>2.0.CO;2, 1977.

Tzivion, S., Feingold, G., and Levin, Z.: An Efficient Numerical Solution to the Stochastic Collection Equation, J. Atmos. Sci., 44, 3139–3149, https://doi.org/10.1175/1520-0469(1987)044<3139:AENSTT>2.0.CO;2, 1987.

von Salzen, K.: Piecewise log-normal approximation of size distributions for aerosol modelling, Atmos. Chem. Phys., 6, 1351–1372, https://doi.org/10.5194/acp-6-1351-2006, 2006.

von Salzen, K., Leighton, H. G., Ariya, P. A., Barrie, L. A., Gong, S. L., Blanchet, J. -P., Spacek, L., Lohmann, U., and Kleinman, L. I.: Sensitivity of sulphate aerosol size distributions and CCN concentrations over North America to SOx emissions and H2O2 concentrations, Journal of Geophysical Research: Atmospheres, 105, 9741–9765, https://doi.org/10.1029/2000JD900027, 2000.

von Salzen, K., Whaley, C. H., Anenberg, S. C., Van Dingenen, R., Klimont, Z., Flanner, M. G., Mahmood, R., Arnold, S. R., Beagley, S., Chien, R.-Y., Christensen, J. H., Eckhardt, S., Ekman, A. M. L., Evangeliou, N., Faluvegi, G., Fu, J. S., Gauss, M., Gong, W., Hjorth, J. L., Im, U., Krishnan, S., Kupiainen, K., Kühn, T., Langner, J., Law, K. S., Marelle, L., Olivié, D., Onishi, T., Oshima, N., Paunu, V.-V., Peng, Y., Plummer, D., Pozzoli, L., Rao, S., Raut, J.-C., Sand, M., Schmale, J., Sigmond, M., Thomas, M. A., Tsigaridis, K., Tsyro, S., Turnock, S. T., Wang, M., and Winter, B.: Clean air policies are key for successfully mitigating Arctic warming, Commun. Earth Environ., 3, 222, https://doi.org/10.1038/s43247-022-00555-x, 2022.

von Salzen, K., Akingunola, A., Cole, J. N. S., Digby, R. A. R., Doherty, S. J., Fraser-Leach, L., Gryspeerdt, E., Sigmond, M., and Wood, R.: Reduced aerosol pollution diminished cloud reflectivity over the North Atlantic and Northeast Pacific, Nat. Commun., 16, 9433, https://doi.org/10.1038/s41467-025-65127-x, 2025.

Wang, H., Peng, Y., von Salzen, K., Yang, Y., Zhou, W., and Zhao, D.: Evaluation of a quasi-steady-state approximation of the cloud droplet growth equation (QDGE) scheme for aerosol activation in global models using multiple aircraft data over both continental and marine environments, Geosci. Model Dev., 15, 2949–2971, https://doi.org/10.5194/gmd-15-2949-2022, 2022.

Wang, H., Peng, Y., Di Noia, A., Shang, H., Letu, H., van Diedenhoven, B., Hasekamp, O. P., Liu, Y., and Quaas, J.: Global quantification of the dispersion effect with POLDER satellite data, Nat. Commun., 16, 7087, https://doi.org/10.1038/s41467-025-62238-3, 2025.

Wang, Y., Zhang, G. J., and Craig, G. C.: Stochastic convective parameterization improving the simulation of tropical precipitation variability in the NCAR CAM5, Geophys. Res. Lett., 43, 6612–6619, https://doi.org/10.1002/2016GL069818, 2016.

Wei, J., Peng, Y., Mahmood, R., Sun, L., and Guo, J.: Intercomparison in spatial distributions and temporal trends derived from multi-source satellite aerosol products, Atmos. Chem. Phys., 19, 7183–7207, https://doi.org/10.5194/acp-19-7183-2019, 2019.

https://doi.org/10.5194/egusphere-2026-6615
Preprint. Discussion started: 10 November 2026
© Author(s) 2026. CC BY 4.0 License.

Wexler, A. S. and Clegg, S. L.: Atmospheric aerosol models for systems including the ions H+, NH4+, Na+, SO42−, NO3−, Cl−, Br−, and H2O, Journal of Geophysical Research: Atmospheres, 107, 4207, https://doi.org/10.1029/2001JD000451, 2002.

Whaley, C. H., Mahmood, R., von Salzen, K., Winter, B., Eckhardt, S., Arnold, S., Beagley, S., Becagli, S., Chien, R.-Y., Christensen, J., Damani, S. M., Dong, X., Eleftheriadis, K., Evangeliou, N., Faluvegi, G., Flanner, M., Fu, J. S., Gauss, M., Giardi, F., Gong, W., Hjorth, J. L., Huang, L., Im, U., Kanaya, Y., Krishnan, S., Klimont, Z., Kühn, T., Langner, J., Law, K. S., Marelle, L., Massling, A., Olivié, D., Onishi, T., Oshima, N., Peng, Y., Plummer, D. A., Popovicheva, O., Pozzoli, L., Raut, J.-C., Sand, M., Saunders, L. N., Schmale, J., Sharma, S., Skeie, R. B., Skov, H., Taketani, F., Thomas, M. A., Traversi, R., Tsigaridis, K., Tsyro, S., Turnock, S., Vitale, V., Walker, K. A., Wang, M., Watson-Parris, D., and Weiss-Gibbons, T.: Model evaluation of short-lived climate forcers for the Arctic Monitoring and Assessment Programme: a multi-species, multi-model study, Atmos. Chem. Phys., 22, 5775–5828, https://doi.org/10.5194/acp-22-5775-2022, 2022.

Wu, M., Liu, X., Zhang, L., Wu, C., Lu, Z., Ma, P., Wang, H., Tilmes, S., Mahowald, N., Matsui, H., and Easter, R. C.: Impacts of Aerosol Dry Deposition on Black Carbon Spatial Distributions and Radiative Effects in the Community Atmosphere Model CAM5, J. Adv. Model. Earth Syst., 10, 1150–1171, https://doi.org/10.1029/2017MS001219, 2018.

Xin, J., Wang, Y., Pan, Y., Ji, D., Liu, Z., Wen, T., Wang, Y., Li, X., Sun, Y., Sun, J., Wang, P., Wang, G., Wang, X., Cong, Z., Song, T., Hu, B., Wang, L., Tang, G., Gao, W., Guo, Y., Miao, H., Tian, S., and Wang, L.: The Campaign on Atmospheric Aerosol Research Network of China: CARE-China, Bull. Am. Meteorol. Soc., 96, 1137–1155, https://doi.org/10.1175/BAMS-D-14-00039.1, 2015.

Yang, K., Koike, T., Ishikawa, H., Kim, J., Li, X., Liu, H., Liu, S., Ma, Y., and Wang, J.: Turbulent Flux Transfer over Bare-Soil Surfaces: Characteristics and Parameterization, J. Appl. Meteorol. Climatol., 47, 276–290, https://doi.org/10.1175/2007JAMC1547.1, 2008.

YishuangLiang and hxmhuang: DESS-of-Tsinghua-University/CIESM: CIESM of Tsinghua University (Version v1.1.0) [Computer software]. Zenodo, https://doi.org/10.5281/zenodo.3596317, 2020.

Yoshioka, M., Mahowald, N. M., Conley, A. J., Collins, W. D., Fillmore, D. W., Zender, C. S., and Coleman, D. B.: Impact of Desert Dust Radiative Forcing on Sahel Precipitation: Relative Importance of Dust Compared to Sea Surface Temperature Variations, Vegetation Changes, and Greenhouse Gas Warming, J. Clim., 20, 1445–1467, https://doi.org/10.1175/JCLI4056.1, 2007.

Young, K. C.: The Role of Contact Nucleation in Ice Phase Initiation in Clouds, J. Atmos. Sci., 31, 768–776, https://doi.org/10.1175/1520-0469(1974)031<0768:TROCNI>2.0.CO;2, 1974.

Yu, H., Kaufman, Y. J., Chin, M., Feingold, G., Remer, L. A., Anderson, T. L., Balkanski, Y., Bellouin, N., Boucher, O., Christopher, S., DeCola, P., Kahn, R., Koch, D., Loeb, N., Reddy, M. S., Schulz, M., Takemura, T., and Zhou, M.: A review of measurement-based assessments of the aerosol direct radiative effect and forcing, Atmos. Chem. Phys., 6, 613–666, https://doi.org/10.5194/acp-6-613-2006, 2006.

https://doi.org/10.5194/egusphere-2026-6615
Preprint. Discussion started: 10 November 2026
© Author(s) 2026. CC BY 4.0 License.



Zaveri, R. A., Easter, R. C., Singh, B., Wang, H., Lu, Z., Tilmes, S., Emmons, L. K., Vitt, F., Zhang, R., Liu, X., Ghan, S. J., and Rasch, P. J.: Development and Evaluation of Chemistry-Aerosol-Climate Model CAM5-Chem-MAM7-MOSAIC: Global Atmospheric Distribution and Radiative Effects of Nitrate Aerosol, J. Adv. Model. Earth Syst., 13, e2020MS002346, https://doi.org/10.1029/2020MS002346, 2021.

Zhang, F. and Li, J.: Doubling–Adding Method for Delta-Four-Stream Spherical Harmonic Expansion Approximation in Radiative Transfer Parameterization, J. Atmos. Sci., 70, 3084–3101, https://doi.org/10.1175/JAS-D-12-0334.1, 2013.

Zhang, G. J. and McFarlane, N. A.: Sensitivity of climate simulations to the parameterization of cumulus convection in the Canadian climate centre general circulation model, Atmosphere-Ocean, 33, 407–446, https://doi.org/10.1080/07055900.1995.9649539, 1995.

Zhang, L., Gong, S., Padro, J., and Barrie, L.: A size-segregated particle dry deposition scheme for an atmospheric aerosol module, Atmos. Environ., 35, 549–560, https://doi.org/10.1016/S1352-2310(00)00326-5, 2001.

Zhang, X. Y., Wang, Y. Q., Niu, T., Zhang, X. C., Gong, S. L., Zhang, Y. M., and Sun, J. Y.: Atmospheric aerosol compositions in China: spatial/temporal variability, chemical signature, regional haze distribution and comparisons with global aerosols, Atmos. Chem. Phys., 12, 779–799, https://doi.org/10.5194/acp-12-779-2012, 2012.

Zhao, X., Lin, Y., Peng, Y., Wang, B., Morrison, H., and Gettelman, A.: A single ice approach using varying ice particle properties in global climate model microphysics, J. Adv. Model. Earth Syst., 9, 2138–2157, https://doi.org/10.1002/2017MS000952, 2017.